Universidade de Aveiro

Universidade Federal
de Pernambuco

YEAR 2024

Rodolfo Rodrigues Nunes da Silva

Lanthanide-Based Primary Luminescent Thermometers for Nanoparticle 3D Localization Using Hyperspectral Microscopy

Termómetros Luminescentes Primários Baseados em Iões Lantanídeos para Localização 3D de Nanopartículas por Microscopia Hiperespectral

Universidade de Aveiro

Universidade Federal de Pernambuco

YEAR 2024

Rodolfo Rodrigues Nunes da Silva

Lanthanide-Based Primary Luminescent Thermometers for Nanoparticle 3D Localization Using Hyperspectral Microscopy

Termómetros Luminescentes Primários Baseados em Iões Lantanídeos para Localização 3D de Nanopartículas por Microscopia Hiperespectral

Tese apresentada à Universidade de Aveiro e à Universidade Federal de Pernambuco para cumprimento dos requisitos necessários à obtenção do grau de Doutor junto ao programa doutoral em Física MAP-fis da Universidade de Aveiro e ao Programa de Pós-Graduação em Química pela Universidade Federal de Pernambuco, de acordo com o Acordo de Doutoramento em Regime de Cotutela internacional. A tese foi realizada sob a orientação científica dos Doutores Luís António Ferreira Martins Dias Carlos e Maria Rute de Amorim e Sá Ferreira André, Professores Catedráticos do Departamento de Física da Universidade de Aveiro, e Ricardo Luiz Longo e Ivani Malvestiti, Professor Titular e Professora Associada, respectivamente, do Departamento de Química Fundamental da Universidade Federal de Pernambuco.

Trabalho desenvolvido no âmbito do projeto CICECO-Aveiro Institute of Materials, UIDB/50011/2020 & UIDP/50011/2020. Financiado por fundos nacionais FCT/MEC NanoHeatControl (POCI-01-0145-FEDER-031469), The Shape of Water (PTDC/NAN-PRO/3881/2020) e LogicALL PTDC/CTM-CTM/0340/2021 e pelo Horizon 2020 FET Open program nº 801305 (NanoTBTech) da União Europeia.

Catalogação na fonte
Bibliotecária: Luiza de Oliveira/CRB 1316

S586l Silva, Rodolfo Rodrigues Nunes da
Lanthanide based primary luminescent thermometers for nanoparticle 3D localization using hyperspectral microscopy / Rodolfo Rodrigues Nunes da Silva – 2024.
137 fls. il.

Orientador: Ricardo Luiz Longo.
Orientadora externa: Maria Rute de Amorim e Sá Ferreira André.
Tese (Doutorado) – Universidade Federal de Pernambuco. CCEN. Programa de Pós-Graduação em Química / Universidade de Aveiro. Programa Doutoral em Física MAP-fis. Recife, Aveiro, 2024.
Inclui referências.

1. Íons de lantanídeos trivalentes. 2. Termômetros luminescentes primários. 3. Regressão linear multiparamétrica. 4. Microscopia hiperespectrais. I. Longo, Ricardo Luiz . II. André, Maria Rute de Amorim e Sá Ferreira III. Título.

541.3 CDD (23. ed.) UFPE - CCEN 2024 – 95

to José Freitas, my beloved husband.

o júri

Presidente

Prof. Doutor Ricardo Luiz Longo
professor titular da Universidade Federal de Pernambuco

Vogais

Prof. Doutora Maria Rute de Amorim e Sá Ferreira André
professora catedrática da Universidade de Aveiro

Prof. Doutora Ana Maria Pires
professora assistente da Universidade Estadual Paulista – Presidente Prudente

Prof. Doutora Maria Cláudia França da Cunha Felinto
Professora titular do Instituto de Pesquisas Energéticas e Nucleares – IPEN/SP

Prof. Doutor Wagner Eduardo da Silva
professor adjunto da Universidade Federal Rural de Pernambuco

Prof. Doutor Hermi Felinto de Brito
professor titular da Universidade de São Paulo

Acknowledgement

As this chapter of my academic journey draws to a close, I cannot overlook the opportunity to express my gratitude to those who supported me along the way. I extend my deepest appreciation to my supervisors, Professors Luís Carlos, and Rute Ferreira, for their invaluable assistance, opportunities for learning, and guidance over the past four years. I also acknowledge the contributions of Professors Ricardo Longo and Ivani Malvestiti, who provided valuable advice from the outset of my academic trajectory.

A special thank you goes to Professor Juliana Angeiras for her assistance during the final sprint of completing the thermometric analysis and for patiently listening to all my concerns and Doctor Keyla Souza for her assistance with excitation thermometry. I seize this moment to express my thanks to Doctor Sandra Correia for her guidance in using fluorometers and other equipment, Doctor Carolina Santos for helping me comprehend hyperspectral data and its processing, and especially Doctor Alexandre Botas for his support in operating the microscope, closely guiding me, and teaching the tools that contributed to the development of my project.

I extend my appreciation to the entire staff of the Department of Physics at the University of Aveiro and the Department of Fundamental Chemistry at the Federal University of Pernambuco for their assistance with the bureaucratic aspects required in various situations.

To my colleagues, Joana Martins, Justyna Zeler, Fernando Maturi, Sofia Zanella, Talita Souza, Ana Luís Moreira, João Ramalho, and all the current and former members of phantom-g and the i3N friends, I express my gratitude for the moments when we not only discussed science but also delved into the fundamental questions of life.

To my family, who consistently believed in me, sometimes more than I believed in myself, I extend heartfelt thanks. A special acknowledgment goes to my mother, who did everything in her power to support my aspirations, and to my husband, who embarked on the adventurous journey of pursuing a PhD abroad and instilled confidence in me.

I wish to express my gratitude to the funding agencies on behalf of CICECO-Aveiro Institute of Materials UIDB/50011/2020 & UIDP/50011/2020, FCT/MEC NanoHeatControl (POCI-01-0145-FEDER-031469), The Shape of Water (PTDC/NAN-PRO/3881/2020), and LogicALL PTDC/CTM-CTM/0340/2021, as well as FET Open Horizon 2020 nº801305 (NanoTBTech) from the European Union.

palavras-chave

Iões de Lantanídeos Trivalentes, Termómetros Luminescentes Primários, Regressão Linear Multiparamétrica, Microscopia Hiperespectrais.

Resumo

Os avanços recentes tornaram a deteção remota através da termometria de luminescência raciométrica, especialmente baseada em iões lantanídeos trivalentes (Ln(III)), uma técnica promissora com uma infinidade de aplicações. No entanto, a maioria dos termómetros luminescentes baseados em Ln(III) existentes requer um processo de calibração com um termómetro externo de referência (termómetros secundários), o que exige calibrações recorrentes, especialmente quando usados em diferentes meios. Esse processo de calibração pode ser impraticável, levando a postular uma relação de calibração independente do meio potencialmente imprecisa. Assim, o uso de termómetros primários baseados em princípios físicos bem estabelecidos torna-se imperativo para superar esses desafios. Apesar de sua importância reconhecida na termometria de luminescência, os termómetros luminescentes primários são atualmente raros. Neste estudo, propusemos, implementámos e validámos termómetros primários que requerem calibração em uma temperatura conhecida (primários-T), que também são autorreferenciáveis, utilizando dados raciométricos dos espectros de excitação. Além disso, combinando com o espectro de emissão, concebemos termómetros que não requerem calibração (primários-S). Embora demonstremos a viabilidade desse método usando um complexo de Eu(III)-β-dicetonato, o $Eu(hfa)_3bpyO_2$, como prova de conceito, a abordagem é universal, e outros materiais baseados em Ln(III) podem ser explorados. Notavelmente, a utilização de vários parâmetros termométricos permite obter uma precisão sem precedentes neste tipo de dispositivos de 0,2% na faixa de temperatura fisiológica. Também explorámos a aplicação da microscopia hiperespectral, uma técnica que combina espectroscopia com microscopia ótica, para obter simultaneamente informações espectrais e espaciais. Avanços recentes na reconstrução ótica aumentaram a relevância da imagem hiperespectral em aplicações biomédicas, como monitorização de agentes de bioimagem, identificação de patogénicos e células cancerígenas, e avaliação da internalização de nanopartículas em células. Neste contexto, foram sintetizadas nanopartículas de Gd_2O_3 codopadas com Yb(III)/Er(III), e foi realizada a sua caracterização estrutural e luminescente, bem como a avaliação de viabilidade celular em linhagens celulares de melanoma humano (MNT-1 e A375). Usando a imagem hiperespectral 2D, abordámos a internalização das nanopartículas pelas células MNT-1 e a sua localização 3D em células fixas em diferentes planos e profundidades da cultura celular. Os resultados demonstram a distribuição das partículas em planos distintos dentro do volume celular, particularmente nas regiões citoplasmáticas e perinucleares. Além disso, usando a emissão das nanopartículas foi determinada a temperatura intracelular obtendo-se um valor compatível com a temperatura ambiente.

keywords

Trivalent Lanthanide Ions, Primary Luminescent Thermometers, Multiparametric Linear Regression, Hyperspectral Microscopy.

abstract

Recent advancements have made remote sensing through ratiometric luminescence thermometry, particularly based on trivalent lanthanide ions (Ln(III)), a promising technique with myriad applications. However, most existing Ln(III)-based luminescent thermometers requires a calibration process with a reference thermal probe (secondary thermometers), which needs recurrent calibrations, especially when used in diverse media. This calibration process can be impractical, leading to the postulation of a potentially inaccurate medium-independent calibration relation. Thus, the use of primary thermometers, based on well-established physical principles, becomes imperative to overcome these challenges. Despite their recognized importance in luminescence thermometry, primary luminescent thermometers are currently rare. In this study, we proposed, implemented, and validated primary thermometers requiring calibration at one known temperature (primary-T), which are also self-referencing, utilizing ratiometric data from the excitation spectra. Additionally, by combining with the emission spectra, we devised thermometers not requiring calibration (primary-S). While we demonstrated the feasibility of this approach using a Eu(III)-β-diketonate complex, the $Eu(hfa)_3bpyO_2$, as a proof-of-concept, the approach is universal, and other Ln(III)-based materials can be explored. Notably, the utilization of various thermometric parameters enabled unprecedented high accuracy of 0.2% in the physiological temperature range. We also explored the application of hyperspectral microscopy, an intriguing technique that combines spectroscopy with optical microscopy, to obtain simultaneous spectral and spatial information. Recent advances in optical reconstruction have enhanced the relevance of hyperspectral imaging in biomedical applications, such as monitoring bioimaging agents, identifying pathogens and cancerous cells, and assessing the cellular uptake of nanoparticles. In this context, we reported the synthesis of Yb(III)/Er(III)-codoped Gd_2O_3 nanoparticles, their structural and luminescence characterization, and their cell viability assessments in Human melanoma (MNT-1 and A375) cell lines. Using 2D hyperspectral imaging, we addressed the internalization of the particles by MNT-1 cells and their 3D localization in a fixed configuration across different planes and cell culture depths. The results demonstrated the distribution of particles in distinct planes deep within the cell volume, particularly in the cytoplasmic and perinuclear regions. Furthermore, using the emission of Yb(III)/Er(III)-codoped Gd_2O_3 nanoparticles the intracellular temperature was predicted with a value compatible with the room temperature.

Table of Contents

Table of Figures

List of Tables

List of abbreviations and symbols

A	Pre-exponential factor
ANOVA	Analysis of variance
$bpyO_2$	2,2′-bipyridine-1,1′-dioxide
CTAB	hexadecyltrimethylammonium bromide
DAPI	4′,6-diamidino-2-phenylindole
DLS	Dynamic light scattering
DMEM	Dulbecco′s modified Eagle′s medium
ECACC	European Collection of Authenticated Cell Cultures
Eu	Europium
FED	Forced electric dipole
h	Planck constant
hfa	hexafluoracetylacetate
LIR	Luminescent intensity ratio
Ln	Lanthanide
MD	Magnetic dipole
MLR	Multiparametric linear regression
MOFs	Metal-organic frameworks
MTT	3-(4,5-dimethylthiazol-2-yl)-2,5-diphenyltetrazolium bromide
NIR	Near-infrared
PMMA	Poly(methyl methacrylate)
PSF	Point spread function
QD	Quantum dots
R	Repeatability
T	Temperature

UCNP	Upconverting nanoparticles
UV-vis	Ultraviolet-visible
Δ	Thermometric parameter
ΔE	Energy difference between thermally coupled states
$\delta\Delta$	Uncertainty in the thermometric parameter
δT	Uncertainty in the temperature
Δ_0	Value of Δ in the limit of zero pump power
g_i	Degeneracy of level i
A_i	Spontaneous emission rate
P_D	Power density
S_r	Relative thermal sensitivity
T_0	Known temperature
W_{nr}	Nonradiative decay
k_B	Boltzmann constant
υ_i	Frequency of level i

1. STATE OF THE ART.

Temperature is a fundamental quantity in many chemical, physical and biological processes, and hence adequate thermometers are crucial for the study and control of these processes. The development of thermometric systems with such a level of spatial resolution is mandatory to understand the thermally dependent processes occurring at the nanoscale. Temperature can be regarded as a relative perception of hot or cold [1]. However, a more accurate definition is stated as: the temperature of a body is the rate of change of its internal energy U with respect to the entropy S at constant volume, namely $T = (\partial U/\partial S)_V$ [2]. Although there are a handful of thermometers adequate for macroscopic systems, the measurement of temperature at the nanoscale continues to be a challenge [3]. Measuring temperature on a micro/submicro scale is an important tool in studies involving nanomedicine (especially intracellular thermometry), microelectronics and micro/nanofluidics, where the size of the sensor and how invasive the method is, are important parameters [3a]. This is particularly relevant in biological microsystems, that demand extra-requirements such as non-contact, high thermal sensitivity in the physiological temperature range (e.g., 293-330 K), high stability, biocompatibility, cell compatibility and versatility to bind to specific intracellular targets [4]. These measurements are essential for understanding various phenomena and processes that occur at submicron scales that are associated with heat transfer or dissipation [3a, 5].

Measurement techniques such as Raman spectroscopy, infrared thermography, and thermal scanning microscopy can be considered to work remotely at the microscale [3a]. Remote temperature measurement and control, that can be made by hyperspectral microscopy, are in demand due to the numerous challenging requests arising from nanotechnology and biomedicine, such as monitoring the intracellular temperature in hyperthermia therapy, where

it is crucial to ensure that the temperature increase is confined to the tumor, preventing damage at the surrounding healthy tissue.

Thermometry has been intensely investigated in the last years because of its relevance to industry and metrology [3b, 6], and for its biomedical applications and engineering [7]. At the micro- and nanoscale, thermometry has been regarded as fundamental to develop underlying laws of heat transfer [3], to design and/or improve new circuits [8], to comprehend quantitatively heat exchange within cells and tissues [7d, 9], and to harmlessly apply hyperthermia therapy [3a, 10].

Luminescent nanothermometry is a method of measuring temperature that uses the relationship between temperature and the photophysical properties of the nanothermometer, e.g. emission intensity, lifetimes of excited states, among others [5]. Luminescent thermometry is a promising method due to their high relative thermal sensitivity (>1%/K) and spatial resolution (<10 μm), short acquisition times (<1 ms), and are non-invasive [3b]. In this context, ratiometric approaches for molecular (or nano) thermometry are widely employed because of their precision, easiness, and high relative sensitivity [11]. Usually, ratios of emission (integrated) intensities are used as thermometric parameters due to the high sensitivity of emission-based techniques allowing, for instance, single particle spectroscopy [11a, 12]. Indeed, photoluminescence of lanthanide trivalent ions, Ln(III), is especially suitable for these measurements [3b] because of the high emission intensities, narrow excitation and emission bands, long emission lifetimes, and spectral ranges from UV-vis to near-infrared [3a]. Another interesting feature of Ln(III) is the nearly independence of the energies of 4*f*-intraconfigurational transition with the surroundings (e. g., ligands, host crystal, solvent, etc.) of the lanthanide ion [13]. This allows for prompt assignments of excitation and emission spectra [12] and predictable energy differences. These features have contributed to an accelerated development of lanthanide-based thermometers in recent years [3a]. As a result, many systems

such as (molecular) complexes with a wide range of solubility, micro- and nanocrystals and nanoparticles, metal-organic frameworks (MOFs), organic-inorganic hybrids [3b, 14] as well as their bioconjugates based on lanthanide ions have been designed and developed [7d]. Despite these numerous developments, there are still a lack of primary thermometers (with known or predictable calibration) based on lanthanide ions, by the time this work started, only a few primary thermometers have been developed to date [15], all based on the temperature dependence of emission features such as the peak energy of semiconductor nanoparticles [16], or the intensity emissions of Ln(III) states in thermal equilibrium [11a, 17]. In fact, several lanthanide ions present states that are separated by hundreds of wavenumbers and are thus thermally coupled. Because the *4f*-4*f* transitions are narrow, the intensities of thermally coupled states can be measured and used as thermometric parameters. The ratio of these intensities can be expressed as $Ae^{-\Delta E/(k_B T)}$, where ΔE is the energy difference between the thermally coupled states, k_B is the Boltzmann constant, T is the temperature, and A is a constant that depends on the properties of these states and may depend on the experimental setup. Thus, if the energy difference ΔE and the pre-exponential factor A are known, the temperature can be determined without previous calibration and a primary thermometer is obtained. Usually, ΔE can be obtained from an emission spectrum or assuming it is not dependent upon the environment from a table with free ion energy levels. On the other hand, despite assuming the factor A being independent of temperature, it has not been determined from additional experimental data and it is quite difficult to calculate for macroscopic systems. As a result, this factor is determined from measurements at a known temperature and the thermometer is calibrated. These primary thermometers have a known thermometric equation that relates Δ quantitatively to the temperature, T, and involves known physical constants [17b, 17c]. In contrast, secondary thermometers require recurrent calibrations when used in different media or conditions [3b]. Recently, a ratiometric thermometer with predictable calibration based on the emissions in

nano and microcrystals of Y_2O_3:Eu(III) was developed [17b]. This thermometer is based on the ratio between the emission intensities of the $^5D_0 \rightarrow {}^7F_4$ Eu(III) transitions when the $^5D_0$ level is excited from the thermally coupled $^7F_0$ and $^7F_1$ or $^7F_2$ levels. The pre-exponential factor in the thermometric parameters can be determined from the ratios of the areas of the corresponding $^5D_0 \rightarrow {}^7F_0$, $^5D_0 \rightarrow {}^7F_1$, and $^5D_0 \rightarrow {}^7F_2$ bands in the emission spectrum.

Ratiometric luminescent primary thermometers can be classified as primary-T or primary-S, depending on whether the thermometric parameter Δ_0 is determined at a known temperature T_0 [11a, 17a, 17c-e] or involves a pre-exponential factor A determined from additional spectral measurements,[17b] respectively. Established primary-T thermometers employ the ratio of the integrated emission intensities of the $^2H_{11/2} \rightarrow {}^4I_{15/2}$ and $^4S_{3/2} \rightarrow {}^4I_{15/2}$ transitions in Er(III) as the Δ parameter,[11a, 15, 17a, 17c-e] while primary-S thermometers use the ratio of the emission intensities of the Eu(III) $^5D_0 \rightarrow {}^7F_4$ transitions when the $^5D_0$ level is populated from the thermally coupled $^7F_0$, $^7F_1$, and $^7F_2$ levels. This type of primary-S thermometer was implemented in $Y_2O_3:Eu^{3+}$ nanocrystals using the Lorentz local-field correction, which depends on the refraction index, for the integrated intensities (areas) [17b]. The pre-exponential factor A in Δ was determined from the ratios of the areas of the $^5D_0 \rightarrow {}^7F_1$ or $^5D_0 \rightarrow {}^7F_0$ transitions in the emission spectrum [17b]. This approach most likely motivated investigations on ratiometric thermometric parameters based on the excitation spectra of Ln(III) ions. Examples as the transitions from the ground and excited states of Eu(III) in $LiSr_{0.988}VO_4$ [18], YVO_4 [19], $LuVO_4$ [20], and $LiLaP_4O_{12}$ nanoparticles [21], of Nd(III) in $LaPO_4$ nanoparticles [22], of Tb(III) in $CaWO_4$ nanocrystals [23], of Pr(III) in the $SrMoO_4$ nanophosphor [24], and of Er(III) in YVO_4 [25]. Various ratiometric thermometric parameters have been proposed based on the excitation spectra of Ln(III) ions, but they have not yet been employed to predict temperature or proposed as primary thermometers [19c].

1.1. LUMINESCENT THERMOMETERS.

Luminescence is the radiative emission from a given material and occurs from transitions between electronic excited states. The external excitation of electronic states is made by different sources of energy [26]. The first observation of the luminescence phenomenon dates to the Middle Ages when materials glowed in the dark after sunlight exposure – then named phosphors. These materials were named after phosphorus, the ancient Greek name given to planet Venus (morning star that announces the sunrise) [26].

Among the luminescent materials, it is important to highlight quantum dots (QD) [27], polymers [28], organic dyes [29], and lanthanide-doped systems (including nanoparticles), the later ones work as thermometers being one of the focus of the current nanothermometry research, due to their unique properties. For instance, the trivalent lanthanide Ln(III)-doped materials have specific properties such as narrow emission bands covering the entire spectral range from ultraviolet (UV), e.g., Gd(III), to the visible, e.g., Eu(III) and Tb(III), and near-infrared, e.g., Er(III) and Nd(III) [30], long-lived lifetimes (ms) and no photoblinking (in contrast to QDs). Lanthanides are the chemical elements whose atomic numbers range from 57 to 71. Unlike most elements, whose valence electrons are placed at the outermost electron shell, lanthanides valence electrons occupy the 4*f* orbitals that are closer to the nucleus than the already filled orbitals 5*s*, 5*p*, and 6*s*. This unique electronic configuration provided valence 4*f* electrons a shielding effect, therefore, they can be accurately described by the approximation of the free ion [31].

The most relevant sensing parameters among lanthanide-based thermometers are based on intensity changes, lifetime change, and ratiometric properties (the ratiometric scheme taking into account the ratio between two thermally coupled states that is affected by temperature to calculate the thermometric parameters) [32]. The intensity of a single transition in luminescent

thermometers is affected by the intersystem crossings for complexes and nanoparticles, and specially by the experimental conditions under which the emission spectrum was recorded [2]. In addition, excitation intensity is critically affected by local changes of the phosphors concentrations, power density laser fluctuations, signal-to-noise detection, compromising the thermometer temperature accurate reading [2, 32].

Temperature sensing by the relative change between two emission intensities (ratio), instead of a single emission, overcomes the problems associated with excitation (e.g., fluctuations of the excitation source) and local concentration variation of the emitting centers. A second emission in this ratiometric scheme can be employed as a reference [2]. The excitation using near-infrared (NIR) radiation as a source of excitation of UCNPs are amongst the more popular Ln(III)-based single-center thermometers [33]. A photon upconversion is a process where the absorption of two (or more) lower energy photons leads to the emission of one higher energy photon. A photon upconversion process involving Ln(III)-based nanomaterials usually involves three steps: photon absorption, energy transfer, and the emission of photons [34]. Taking the example of Er(III)-Yb(III) pair, Figure 1, represents its simplified energy diagram and its upconversion process when excited with 980 nm wavelength light.

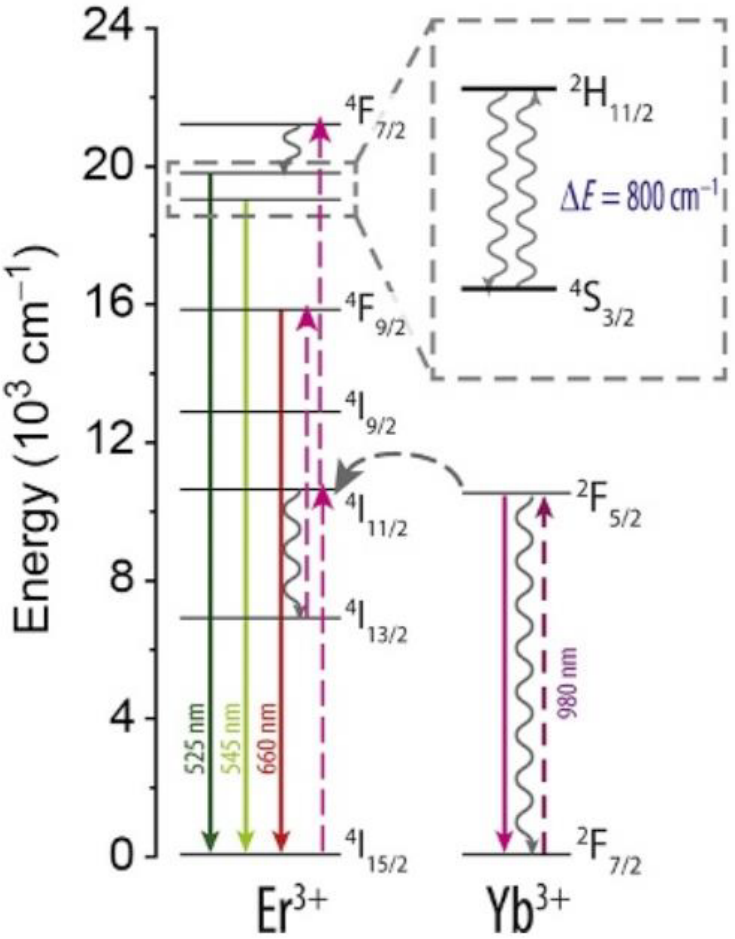

Figure 1. Partial energy-level diagram of Er(III)-Yb(III) ions highlighting the Yb(III) absorption at 980 nm. The diagram depicts Yb(III)-to-Er(III) energy transfer pathways and the $^2H_{11/2} \rightarrow {}^4I_{15/2}$, $^4S_{3/2} \rightarrow {}^4I_{15/2}$, and $^4F_{9/2} \rightarrow {}^4I_{15/2}$ Er(III) emissions. The expansion depicts the thermally coupled $^2H_{11/2}$ and $^4S_{3/2}$ levels of Er(III) adapted from [17c].

The Yb(III) is labeled as sensitizer and Er(III) as activator because Yb(III) ions are responsible to sensitize the emitting Er(III) levels upon NIR irradiation. Balabhadra *et al.* reported in 2017 [17c] a primary thermometer based on Er(III)/Yb(III):SrF_2 NPs which is characterized by a well-established thermometric equation that is used to determine the absolute temperature, without the need of prior external calibration process. In single-center ratiometric thermometers as this, Δ (or luminescent intensity ratio - LIR), the thermometric parameter is defined using the emission intensities from two separate levels. If the energy

separation (ΔE), where ΔE is the energy difference between the barycenter of the two levels, e.g., $^2H_{11/2}$ and $^4S_{3/2}$ of Er(III), is small (i.e., $200 < \Delta E < 2000$ cm^{-1} comparable to the thermal energy $k_B T$, where k_B is the Boltzmann constant, and T is the temperature), it is common to say they are "thermally coupled". In this case, both levels are populated according to the Boltzmann statistics and the Δ is written as:

$$\Delta = Ae^{-\Delta E/(k_B T)} \qquad \text{Equation 1}$$

where k_B is the Boltzmann constant and $A = g_1 A_1 h\upsilon_1/(g_2 A_2 h\upsilon_2)$ where h is the Planck constant, g_i is the degeneracy of level i, A_i the spontaneous emission rate, and υ_i the frequency of level i [3a]. Up to now, in most of the examples involving the temperature determination in single-center thermometers based on the thermally coupled levels, it is required an external thermal calibration of the thermometric parameter with a reference thermometer – secondary thermometers, because the constant A cannot be calculated with sufficient accuracy. Balabhadra *et al.* proved that ΔE and A can be measured independently of any experimental calibration and the temperature is directly calculated using Δ, demonstrating this system is a primary thermometer. In this regard, a mathematical manipulation of the equation leads to the equation (1) was used to determine the temperature:

$$\frac{1}{T} = \frac{1}{T_0} - \frac{k_B}{\Delta E}\ln\left(\frac{\Delta}{\Delta_0}\right) \qquad \text{Equation 2}$$

where Δ_0 corresponds to the value Δ in the limit of zero pump power at a known temperature T_0. Because this thermometer requires determining Δ_0 at a known temperature T_0, it is classified as primary-T.

The uncertainty in the thermometric parameter, δΔ, is calculated as:[35]

$$\delta\Delta = \Delta\sqrt{\left(\frac{\delta I_H}{I_H}\right)^2 + \left(\frac{\delta I_S}{I_S}\right)^2} \qquad \text{Equation 3}$$

where $\delta I_{H,S}/I_{H,S}$ is estimated using the signal-to-noise ratio values, typically calculated dividing the readout fluctuations of the baseline by the maximum intensity value of the $^2H_{11/2} \rightarrow {}^4I_{15/2}$ (I_H) and $^4S_{3/2} \rightarrow {}^4I_{15/2}$ (I_S) transitions.

Comparison between different thermal probes is an important aspect, particularly, to access the performance of the thermometer for a specific application. Thus, the thermometer's performance can be evaluated based on its relative thermal sensitivity (S_r), temperature uncertainty (δT), repeatability, reproducibility, and spatio-temporal resolution.[4]

The absolute thermal sensitivity is the rate of change of the thermometric parameter Δ by temperature unit. However, it is meaningless to compare absolute thermal sensitivity among thermometers operating by different physical principles or materials. Thus, in order to compare the performance of distinct thermometers, it is used the relative thermal sensitivity (S_r) [33]:

$$S_r = \frac{1}{\Delta}\left|\frac{\partial \Delta}{\partial T}\right| 100\% \qquad \text{Equation 4}$$

usually expressed in units of % change per degree of temperature change (% K^{-1}).

The temperature uncertainty (or temperature resolution) describes the smallest temperature resolvable by the thermometer. The uncertainty in the temperature arises from several factors, such as the experimental detection setup, the acquisition conditions, and the signal-to-noise ratio and, of course, it depends on the material employed. δT can be estimated by the time-dependent output fluctuations of the thermometer calculated temperature or by the estimation [33]:

$$\delta T = \frac{1}{S_r}\frac{\delta \Delta}{\Delta} \qquad \text{Equation 5}$$

where $\delta\Delta/\Delta$ is the relative uncertainty in the determination of the thermometric parameter (depending on the acquisition setup and estimated from the errors in Δ).

The spatial (δx) and temporal (δt) resolutions of a measurement are defined as the minimum distance or time interval between measurements, respectively, presenting a

temperature change larger than δT [3b, 33]. The thermometer's reproducibility refers to the change of the same measurement carried out under different conditions (e.g., different equipment or observer). The repeatability, R, characterizes the thermometer capacity to provide repeatedly the same result, under the same circumstances, and is calculated as [33]:

$$R = 1 - \frac{\max|\Delta_c - \Delta_i|}{\Delta_c} \qquad \text{Equation 6}$$

where Δ_c and Δ_i represent, respectively, the mean value and the measured values at each temperature of thermometric parameter.

Over the past decade, luminescent thermometers have seen remarkable and continuous advancement, following a few pioneering works published in the last quarter of the 20th century. Various types of phosphors have been explored, including polymers, DNA or protein conjugates, organic dyes, quantum dots (QDs), as well as transition metal and Ln(III)-doped materials. These materials offer remote thermal detection through their light emission properties, contrary to the common misconception of being contactless. While many examples are based on individual thermal probes, more intricate structures such as core@shell nanoarchitectures, heater-thermometer nanoplatforms, and mixtures of thermographic phosphors encapsulated into polymers and organic–inorganic hybrids have also been demonstrated.

The diverse range of reported examples, particularly those operating at the nanoscale, underscores the growing interest in luminescence thermometry across various fields including microelectronics, microoptics, photonics, micro and nanofluidics, nanomedicine, theranostics, and numerous other potential applications such as thermally-induced drug release, phonon-, plasmonic-, and magnetic-induced hyperthermia, and in scenarios where exothermal chemical or enzymatic reactions occur at submicron scales.

While many luminescent thermometers currently available require calibration with a reference thermal probe (termed secondary thermometers) and necessitate recurrent calibrations, especially when used in different environments, this process can be impractical. In some cases, a medium-independent calibration relation is proposed, which may introduce inaccuracies. To address this limitation, primary thermometers, which determine temperature based on well-established physical principles, are essential. However, despite being recognized as a significant advancement in luminescence thermometry, primary luminescent thermometers remain scarce.

The first review regarding luminescent primary thermometers and their applications was published by Martins *et al.* [36]. The text will delve into their thermometric attributes, assess their performance in comparison to non-luminescent primary examples, and outline several challenges that need to be addressed to foster the further development of primary thermometers.

1.2.HYPERSPECTRAL MICROSCOPY.

Hyperspectral microscopy is a technique that can be used to obtain both spatial and spectral information simultaneously [37]. Hyperspectral images are images in which a spectrum is measured for each pixel. A pixel is the spatial subdivision of images. They are small sets of information that are spatially correlated [38]. A hyperspectral image can be visualized as a hypercube of data (Figure 2) and it has three dimensions: two spatial (X and Y) and one spectral (λ, wavelength).

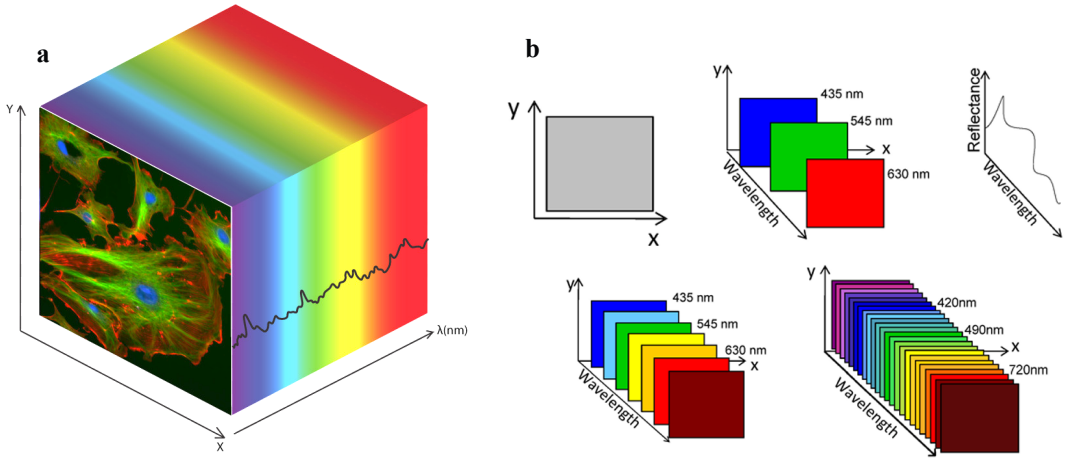

Figure 2. (a) hyperspectral image of a thyroid and salivary gland tumour detection. Courtesy of CleanPNG. (b) Schematic representation of a hypercube which is a 3D-dataset of spatial and spectral information. Source: Author.

Hyperspectral images have applications in remote sensing of the Earth [39], food quality control [40], material phase identification in micro- and nanoscale [37b], and safety. In this last example the variations of blood oxygenation of hands and face are detected, which are used to ascertain signs of emotional stress in potential criminals [41].

The relevance of hyperspectral imaging in sub-micrometer scale mapping has been described in studies focused on biomedical applications, such as the monitoring of the cellular uptake of nanoparticles [42], and the identification of pathogens and cancer cells [43]. In these examples, the spectral profile results from light scattering measures. The combination of hyperspectral microscopy and emission properties is even less explored and only three examples have been reported so far. The first refers to down-shifting energy conversion of silicon nanoparticles, where emission in the red spectral region combined with hyperspectral analysis was used to discuss the homogeneity of the film obtained in resolution at the submicrometric scale [16b]. The second example explores hyperspectral microscopy of the MG-63 cell line, where emission comes from nanoparticles, which allowed monitoring of cell assimilation of lanthanide nanoparticles [44]. The third one explores the of Er(III)/Yb(III)-co-

doped GeO_2−Ta_2O_5 composite dispersed in PMMA with a concentration of 9.0 wt % for real-time temperature sensing and photothermal conversion [45].

Recently, hyperspectral microscopy was also successfully used to study the anisotropy of lanthanide-based crystals [46]. Rodrigues *et al.* described a protocol for a novel application of hyperspectral images to study the properties of Eu-Tb single crystals. According to the authors this protocol can be extended to other types of materials such as organic-inorganic hybrids inorganic microparticles [47], micron-sized molecular crystals [48], and nanoparticles in biological tissues [49].

1.3. INTRACELLULAR THERMOMETRY.

In cellular studies, such as the cellular division and death, temperature plays a key role [50]. Thermosensing in living cell requires precise thermometers working at the micro/nanoscale with high spatial resolution. Brites *et al.* have offered a general overview on many kinds of nanothermometers [5]. Most of the systems used for intracellular thermometry are noncontact and use optical properties for detection, such as intensity changes, lifetime change, and band-shape [51].

There are several types of materials that can be used for intracellular thermometry such as organic molecular dyes, polymers, inorganic nanoparticles, organic-inorganic hybrids, amongst others [51]. For instance, Piñol *et al.*[7a] have described a real-time intracellular temperature measurement using luminescent Ln(III)-bearing polymeric micellar probes (Ln(III) = Sm(III) and Eu(III)) incubated in breast cancer MDA-MB468 cells. The 2D temperature mapping recorded an increasing in the temperature of the cells in the physiologic range showing inhomogeneous intracellular temperature progressions up to ∼20 degrees and subcellular gradients of ∼5 degrees between the nucleolus and the remaining of the cell,

illustrating how temperature can be different in each organelle highlighting the potential of this tool to study intracellular processes.

High-resolution thermal sensing is not only interesting at the cellular level, but also in animal models, which are more useful in diagnosis and controlled hyperthermia treatment. As mentioned above, temperature plays an important role in intracellular mechanisms and its measurement and control is the next step on intracellular thermometry.

Debasu *et al.*[52] prepared a nanoplatform where nanoheaters and nanothermometers could be used to measure and control the temperature, using thermometric $(Gd_{0.97}Yb_{0.02}Er_{0.01})_2O_3$ nanorods as the central core and gold nanoheaters as surface decoration. However, the system was over-sized, and it was not possible to test this nanoplatform as a nanoheater.

Herein will be shown how the hyperspectral microscopy can be used to monitoring the intracellular temperature using primary thermometers based on lanthanide upconverting nanoparticles.

1.3.1. Hyperspectral microscope and intracellular temperature sensing.

As mentioned above, the temperature can be measured using the emission spectra of luminescent materials. Having the properties of hyperspectral microscope, it is possible to record the emission spectra of lanthanide upconversion nanoparticles. The hyperspectral image is mainly defined as a collection of spectra, i.e., each pixel has an associated spectrum. Each pixel field-of-view on the Cytoviva hyperspectral images system, available at Phantom-g, Aveiro, corresponds to 129×129 nm^2 on the sample's plane, using an objective of 100× magnification. The hyperspectral scanning is vertical and each image results from 696 lines, using an exposure time, which will choose depending on the sample, per line.

Debasu *et al.* discussed the incorporation of gadolinium oxide nanoparticles co-doped with Er(III) and Yb(III), which works as a primary thermometer, into breast cancer cells MG-63 [44]. Using the hyperspectral microscope, it is possible to locate and obtain the emission spectra from the upconverting nanoparticles.

It was possible to observe cells with the nanoplatform-treated showing dark and bright spots (Figure 3.B) larger than approximately 2 mm, not visible in the images of control cells (Figure 3.A), and this is associated with the nanoparticle clusters located outside the cancer cells.

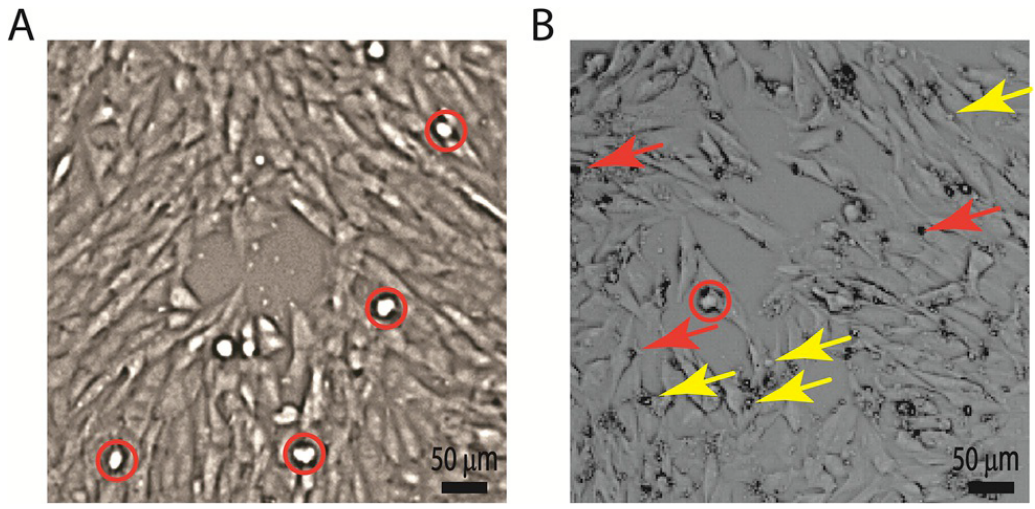

Figure 3. Bright-field optical images of (A) control MG-63 cells and (B) MG-63 cells treated with NRs-AuNRs. The red and yellow arrows in (B) depict black and white points, respectively, not visible in (A), ascribed to nanoplatform clusters. Adapted from[44].

Debasu *et al.* obtained the hyperspectral images from cancer cells with an imaging microscope. The image obtained with laser excitation has the advantage of locating the nanoplatforms via the Er(III) emission spectrum (Figure 4D). A reference spectral library was created from the white-light scattering of the region from where the Er(III) emission is collected (Figure 4C). This spectral library was subsequently used for mapping the nanoplatforms within MG-63 cells.

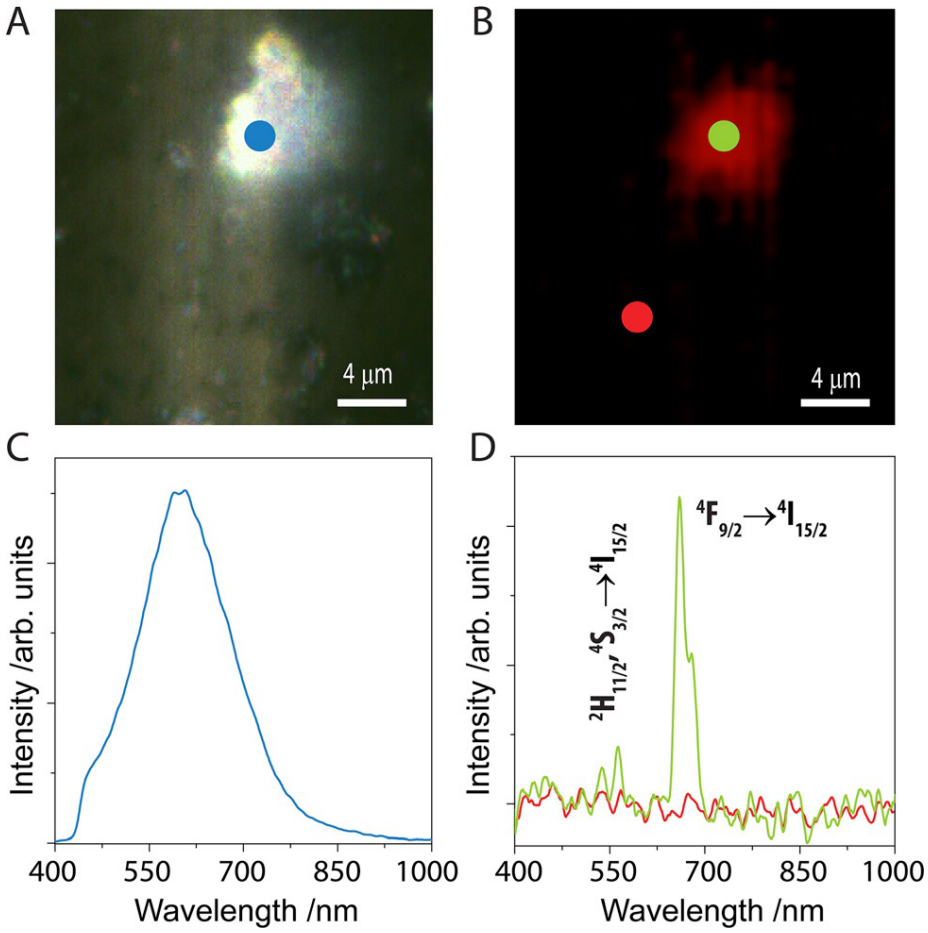

Figure 4. Hyperspectral images of NRs-AuNRs under (A) white-light and (B) 980 nm excitation. The spectral profile from the regions marked by blue, green, and red are shown in (C) and (D), respectively. Adapted from [44].

Using the spectral collection from the hyperspectral image acquired, and having a well-designed calibration curve, it is possible to estimate the temperature. Hyperspectral imaging mapped the nanoplatforms within cells, based on a reference spectral library generated from a white-light scattering spectral profile, opened a new avenue to monitor the cellular uptake of Ln(III)-bearing nanoplatforms.

2. GOALS.

2.1.GENERAL GOALS AND PROCEDURES.

The main goal of this thesis is to develop new approaches and methods to measure temperature at the submicron-scale, or even at the nanoscale, based on luminescent thermometers. A novel approach to luminescent thermometry based on the excitation spectra was developed and tested for its generality, that included the extension of the previous proposal, where it was applied to the Eu(III)-diketonate-coordination compound and to nanoparticles of yttrium oxide doped with trivalent europium [53]. In addition, it was developed a temperature mapping protocol at submicron-scale using the well-stablished upconversion luminescence protocol and hyperspectral microscopy.

Following the proposal of Dr. Keyla de Souza [54], primary thermometers based on the excitation and emission spectra of Eu(III) ions in nanoparticles of yttrium oxide doped with trivalent europium were investigated and validated. The choice of this type of system is justified by the fact that they do not have chromophores, transitions at lower wavelengths, minimizing uncertainties, and the possibility of presenting emission from $^5D_1$ and $^5D_2$ levels, because non-radiative processes are minimized. For this part of the PhD research, the following specific goals can be identified:

1- synthesis of Eu(III)-doped NPs, namely BiF:Eu1 and $Y_2O_3:Eu^{3+}$, systems that present emissions from $^5D_0$ and $^5D_1$ levels, and possibly $^5D_2$;
2- characterization of these NPs, specially their luminescent and thermal properties;
3- determination of the excitation and emission spectra at temperatures ranging from 12 to 340 K; and

4- analysis and validation of the excitation spectra of these systems to develop new primary nanothermometers.

More specifically, the temperature mapping by hyperspectral microscopy employs UCNPs because of the NIR radiation excitation lies in the biological window and measurement within the visible region. This excitation source has a greater depth of penetration on biological tissues, being an advantage for this kind of applications. Among UCNPs, the ones doped with Er(III), such as $(Gd_{0.97}Yb_{0.02}Er_{0.01})_2O_3$, (with emission in the first biological window with the wavelength range from 700 nm to 950 nm (NIR-I)) co-doped with Yb(III) (with excellent absorption at 980 nm) [55] can function as primary nanothermometer [17c, 56].

Thus, three specific goals may be identified for this part of the research:

1- the synthesis of UCNPs that will work as primary nanothermometers;
2- incorporate these primary nanothermometers into the cells; and
3- developing a temperature mapping protocol.

3. EXPERIMENTAL.

3.1.MATERIALS AND METHODS.

The Figure 5 shows the schematic setup of the hyperspectral microscope. Using this setup, both optical and hyperspectral images were acquired as described below.

.

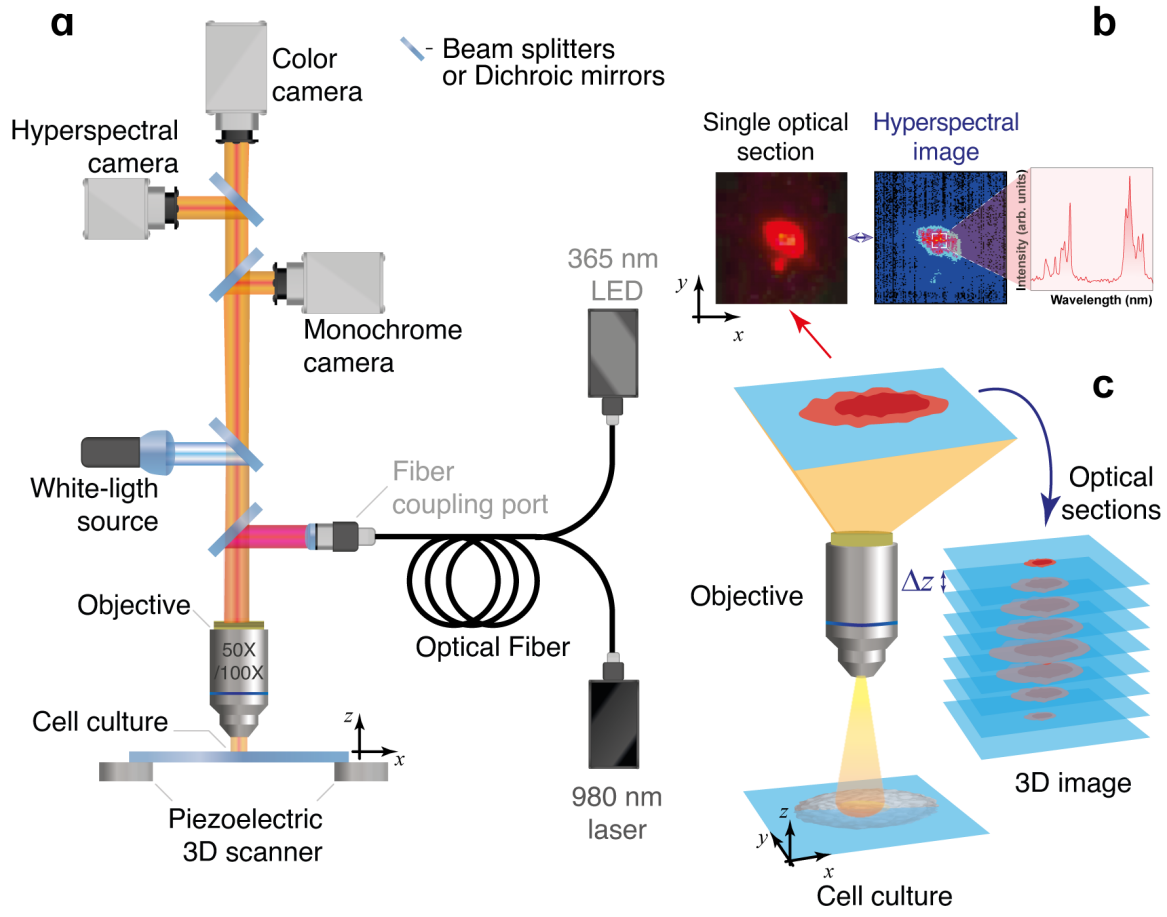

Figure 5. (a) Schematics of the hyperspectral microscope. (b) Optical section of the cell culture, the corresponding hyperspectral image, and the spectral profile. (c) Construction of the 3D image by the composition of the optical sections in distinct z planes, separated by Δz. Source: Author.

Optical Images: The optical microscopy images were recorded using an Olympus BX51 microscope (10×, 50×, and 100× objectives), equipped with a color digital CCD camera (Retiga

4000R, QImaging) and a monochrome digital CCD camera (01-QI825-M-16-C, QImaging). The samples were irradiated using white light of an illuminator (Lumen 200, Prior) that was filtered using a Dual Mode Fluorescence Module from CytoViva, resulting in an emission band between 552 and 592 nm with peak at ca. 580 nm, or using a CW NIR laser diode (PSU-H-LED, CNI Lasers) at 980 nm.

Hyperspectral images: The hyperspectral microscope images were obtained with a digital camera (IPX-2M30, Imperx) coupled to a spectrograph (V10E 2/3″, Specim, 30 μm slit, nominal spectral range of 400–1000 nm, and nominal spectral resolution of 2.73 nm). The variation of the plans in which the hyperspectral images were obtained was performed by moving in the *z*-axis the piezo-driven platform to the position that corresponds to the selected plan. The hyperspectral images were recorded in bright field reflection mode, under irradiation from a 980 nm CW NIR laser excitation.

The hyperspectral images were acquired using CW NIR laser diode (PSU-H-LED, CNI Lasers) at 980 nm. To calculate the laser power density, the optical power and the beam profile were measured by placing a powermeter (FieldMaxII-TOP OP-2 Vis, Coherent) and a CCD camera (BC106N-VIS/M, Thorlabs), respectively, in the position where the sample will be positioned to take hyperspectral microscope images.

3.2.SYNTHESIS OF THE NANOPARTICLES**.**

3.2.1. Synthesis of the $(Gd_{0.97}Yb_{0.02}Er_{0.01})_2O_3$ UCNPs

$(Gd_{0.97}Yb_{0.02}Er_{0.01})_2O_3$ *nanoparticles:* Spherical $(Gd_{0.97}Yb_{0.02}Er_{0.01})_2O_3$ nanoparticles were synthesized following a procedure [44] modified from a previously established methodology [57]. In a typical procedure, aqueous solutions of $Gd(NO_3)_3$ (2.94 mL, 0.4 mol/L), $Yb(NO_3)_3$ (0.030 mL, 0.4 mol/L), and $Er(NO_3)_3$ (0.120 mL, 0.1 mol/L) were mixed in distilled water (200 mL). Urea (2.7 g) and hexadecyltrimethylammonium bromide (CTAB) (0.6 g) were dissolved in this

solution under ultrasonication and magnetic stirring. The mixture was heated up at 358 K and the reaction was refluxed for 3 h. The final product was washed with distilled water and ethanol several times, collected *via* centrifugation (600 rpm, 25 minutes), and dried at 348 K for 24 h. To obtain crystalline $(Gd_{0.97}Yb_{0.02}Er_{0.01})_2O_3$ nanoparticles (where the concentrations are the nominal molar concentrations) the dried powder was calcined at 1073 K for 3 h.

3.3. Synthesis of the BiF_3:Eu nanoparticles

The Eu(III)-doped bismuth oxyfluoride nanoparticles (e.g., BiF_3:Eu1 as 1% Eu(III) doping BiF_3:Eu5 as 5% Eu(III) doping) were prepared by Zanella et al. [53] from the Department of Molecular Sciences and Nanosystems from Ca' Foscari University of Venice.

3.4. Synthesis of the Y_2O_3:Eu^{3+} nanoparticles

The Y_2O_3:Eu^{3+} nanoparticles were synthesized following the procedure described by Debasu [58] and it was fully characterized according to the work developed by Debasu and collaborators.

3.5. SYNTHESIS AND CHARACTERIZATION OF $Eu(hfa)_3bpyO_2$.

Equimolar quantities of (2,2´-bipyridine-1,1´-dioxide) $bpyO_2$ and complex $Eu(hfa)_3(H_2O)_2$, using hexafluoroacetylacetate (hfa) (synthesized according to the method described in ref. [59]) were stirred under reflux in methanol for 12 hours (Scheme 1). A white precipitate of the $Eu(hfa)_3bpyO_2$ complex (**1**) was isolated by solvent evaporation. It was then washed with water (3 – 10 mL) and dried at 50 °C under vacuum for 12 hours (yield 92 %). Elemental analysis: Calcd. for $C_{25}H_{11}F_{18}N_2O_8Eu$ (961.30): C, 31.24; H, 1.15; N, 2.91. Found: C, 31.18, H 1.19, N 2.85. Fourier transform infrared spectroscopy – attenuated total reflectance (FTIR–ATR): 3131 w, 2901 w, 1655 s, 1555 m, 1530 s, 1500 s, 1481 s, 1430 m, 1256 s, 1210 s, 1145 s, 1098 m,

1035 w, 950 w, 854 w, 838 m, 798 m, 771 m, 741 w, 721 m, 660 s, 585 s cm^{-1}. m/z = 943 $[Eu(hfa)_3(bpyO_2)\text{-}F]^+$.

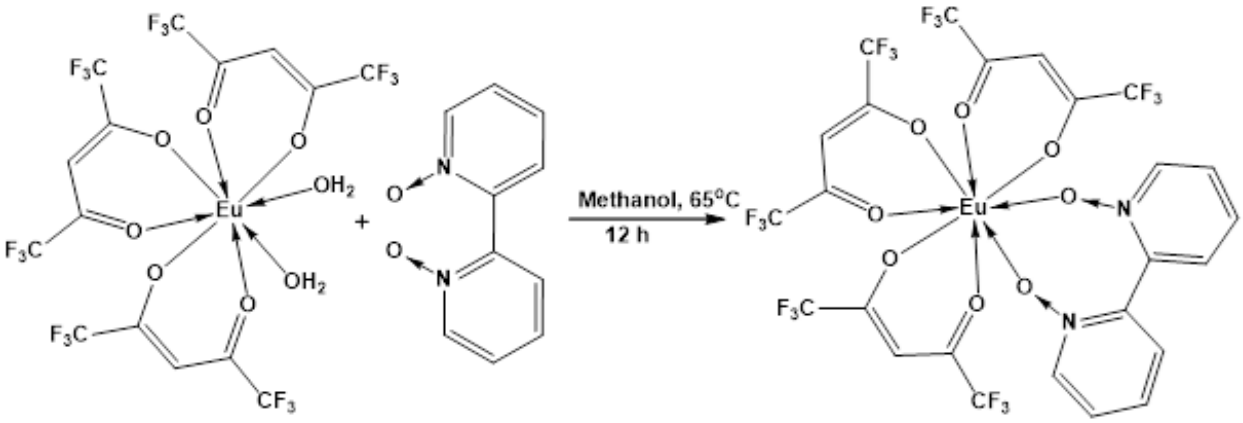

Scheme 1. Synthesis of the $Eu(hfa)_3bpyO_2$ complex (1).

3.6. CHARACTERIZATION.

Powder X-ray diffraction: Diffraction patterns were collected on a powder X-ray diffractometer (PANalytical Empyrean), using Cu-$K_{\alpha 1}$ radiation (0.1540 nm, 45 kV, 40 mA) in the reflection spinning scan mode in the range 15.00 – 50.00º (2θ) with a 0.04 degrees step and 1.8 s acquisition time per step.

Electronic microscopy: The morphology of the samples was analyzed on a Hitachi H9000 transmission electron microscope (TEM) operated at 200 kV.

Photoluminescence: The upconversion emission spectra were recorded at room temperature on a Fluorolog®-3 Horiba Scientific (Model FL3-2T) spectroscopy, with a TRIAX 320 single-emission monochromator (fitted with a 1200 grooves mm^{-1} grating blazed at 500 nm, reciprocal linear density of 2.6 nm mm^{-1}), coupled to an R928 Hamamatsu photomultiplier, using the front-face acquisition mode. The excitation source was a continuous wave laser diode

at 980 nm (Thorlabs LDM21 mount, LDC220 laser diode controller, and TED200 temperature controller) focused using a C230TM-B aspheric lens (Thorlabs). The emission spectra were corrected for the detection and optical spectral response of the spectrofluorometer using a photodiode reference. The laser power on the sample was measured using a FieldMaxII-TOP Laser Power and Energy Meter (Coherent Inc.) coupled with a neutral density filter (NE10B-B, Thorlabs) to avoid saturation of the power meter at high laser power. The average diameter of the spot area on the sample is 406 μm.

DLS and Zeta potential: The measurements were recorded at 298 K using a Malvern Zetasizer Nano series instrument, Nano-ZS (Red badge operating with a 632.8 nm laser, Model ZEN3600, UK). A folded capillary cell (Malvern instruments, DTS1070) was used for both measurements. The average of three measurements with ten scans was reported.

The log-normal fitting function of OriginLab® is:

$$y = \frac{A}{\sqrt{2\pi}\omega x}\exp[-(\ln(x/x_c))^2/(2w^2)] \qquad \textbf{Equation 7}$$

where A is the area under the curve, w is the log standard deviation and x_c the position of the center of the distribution. The log-normal function was used to fit the histogram of DLS diameter values.

The Gaussian fitting function of OriginLab® is:

$$y = \frac{A_0}{w\sqrt{\pi/(4\ln 2)}}\exp(-4\ln 2\,(x - x_c)^2/w^2), \qquad \textbf{Equation 8}$$

where A_0 is the area under the curve, w is the standard deviation and x_c the position of the center of the distribution. The Gaussian function was used to fit the histogram of zeta potential values.

Optical Microscopy. The optical microscopy images were recorded using an Olympus BX51 microscope (50× and 100× objectives), equipped with a color (Retiga 4000R, QImaging) and a monochrome (01-QI825-M-16-C, QImaging) digital CCD cameras. The bright-field images (in transmission and reflection modes) were acquired under white light (DC regulated illuminator, DC-950, Fiber-Lite), UV (LED light, LLS-365, Ocean Optics, emission at 365 ± 25 nm), or NIR (CW laser diode at 980 nm, PSU-H-LED, CNI Lasers) irradiations. A scheme of the setup is presented in Figure 5a.

The laser beam homogeneity was measured using a procedure described elsewhere [60] Figure 6. The power density of each pixel (P_D) was obtained by the ratio between the measured power, using a power meter (FieldMaxII-TOP OP-2 Vis, Coherent), and the area of a single-pixel (6.45×6.45 μm^2) of the CCD camera (BC106NVIS/M, Thorlabs). In the region of the inset of Figure 6, the mean value ± standard deviation of P_D, considering only values higher than 36.8% of the maximum intensity (*i.e.,* 1/e), is 0.25±0.02 W cm^{-2}.

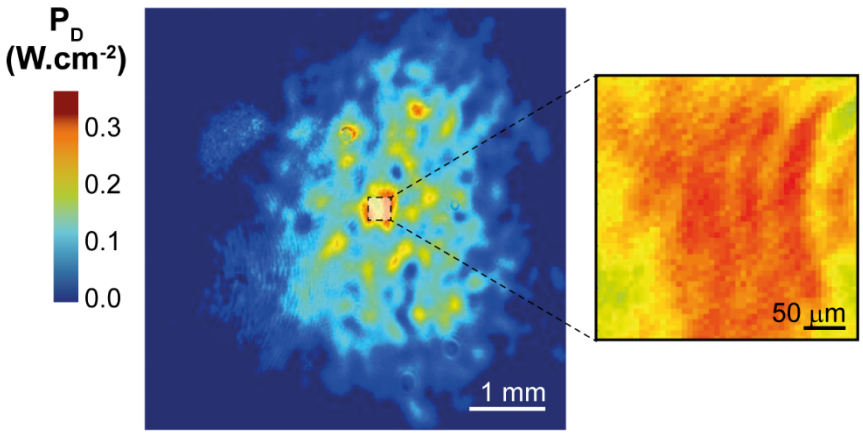

Figure 6. Power density profile of the 980 nm laser beam. The inset presents the beam region used to irradiate the samples in the hyperspectral images. Adapted from reference.[60]

Hyperspectral Microscopy: The hyperspectral microscope images were performed with a digital camera (IPX-2M30, Imperx) coupled to a spectrograph (V10E 2/3″, Specim, 30 μm slit, nominal spectral range of 400–1000 nm, and nominal spectral resolution of 2.73 nm). Each

pixel field-of-view of the hyperspectral images recording with the 100× objective corresponds to 129×129 nm^2, on the plane of the samples. The hyperspectral scanning is performed line-by-line, with a total of 696 lines using an exposure time of 3.0 s per line. All the hyperspectral data were acquired and analyzed using the ®ENVI 4.8 software.

3D imaging system. The 3D images were created using the custom CytoViva Acquisition Software by acquiring 320 optical microscopy images (2D optical sections), with the monochrome digital CCD camera, at different surface depths using an automatic piezo-driven *z*-axis platform (Nano-Z Series, Mad City Labs) and a distance between optical sections (Δz) of 200 nm (Figure 5b,c). For the nuclei of the cells, the 2D optical sections were recorded in bright field reflection mode under UV irradiation. The images were obtained by deconvolution assuming that the optical path through the instrument is optically perfect and convoluted with a point spread function (PSF), *i.e.*, a mathematical function describing the distortion of the optical path by a point source of light through the instrument. The used PSF is based on the numerical aperture and index of refraction of the objective, the refraction index of the medium, and the 4,6′-diamidino-2-phenylindole (DAPI) emission wavelength. For the nanoparticles, the 2D optical sections were recorded in dark-field transmission mode using the CytoViva enhanced dark-field illumination system (CytoViva, Auburn, AL, USA), under red light illumination. The irradiation band (552-592 nm, peak at ca. 580 nm) was achieved by filtering the white light from the illuminator (Lumen 200, Prior) by a dual-mode fluorescence module. The location of the nanoparticles uses their scattering intensity since the regions where the nanoparticles are located are those presenting higher scattering intensity (Figure 26). The positions of the particles are detected searching along each column of pixels - that result from the stacking of the images acquired along the *z*-axis - the localization of the object with the highest scattering intensity. The pixel with the highest intensity is considered as the location of

the center of the nanoparticle and is represented in the 3D image by a sphere. Only the pixels with intensity above a certain threshold were considered to eliminate the contribution of the background signal.

The biological assessments for the cell lines were conducted in collaboration with Dr. Helena Oliveira's group, in the Deparment of Biology at University of Aveiro, as follows:

Cell lines and culture conditions. Human melanoma MNT-1 cells were kindly provided by Manuela Gaspar (iMed.ULisboa, Portugal). A375 cell line was purchased from the European Collection of Authenticated Cell Cultures (ECACC) and supplied by Sigma-Aldrich (Spain). MNT-1 and A375 cells were aseptically grown in Dulbecco's modified Eagle's medium (DMEM), supplemented with 10% FBS, 2 mM l-glutamine, 100 U/mL penicillin–100 μg mL^{-1} streptomycin, and 2.5 μg mL^{-1} fungizone in a humidified incubator at 310 K and 5% CO_2.

Viability assessment. The effect of the nanoparticles on cell viability was determined by the colorimetric 3-(4,5-dimethylthiazol-2-yl)-2,5-diphenyltetrazolium bromide (MTT) assay, which measures the formation of purple formazan in viable cells [61] following the norm ISO 10993-5:20099(en) [62]. MNT-1 and A375 cells were seeded in 96 wells plates. MNT-1 were seeded at 3500 and 2000 cells per well for 24 and 48 h exposure, respectively, while A375 were seeded at 3500 and 2500 cells per well for 24 and 48 h exposure, respectively. After adhesion, cells were incubated for 24 and 48 h with $(Gd_{0.97}Yb_{0.02}Er_{0.01})_2O_3$ nanoparticles at 0, 12.5, 25, 50, 100, and 200 μg mL^{-1}. Control cells were incubated with a culture medium. At the end of the incubation time, the wells were emptied, washed with the phosphate-buffered saline (PBS) solution to remove the remaining particles, and a fresh medium (100 μL) was placed in each well. After that, 50 μL of MTT (1 mg. mL^{-1} in PBS) was added to each well and incubated for 4 h at 310 K in a 5% CO_2 humidified atmosphere. Thereafter, the culture

medium with MTT was removed and replaced by 150 µL of DMSO to dissolve the formazan crystals. The absorbance was measured with a plate reader (Synergy HT Multi-Mode, BioTeK, Winooski, VT) at 570 nm with blank corrections. The cell viability (*V*) was calculated, with respect to the control cells, using:

$$V\ (\%) = \frac{A_{\mathrm{s}} - A_{\mathrm{DMSO}}}{A_{\mathrm{c}} - A_{\mathrm{DMSO}}} \times 100\% \qquad \text{Equation 9}$$

where A_{s}, A_{DMSO}, and A_{c} are the values of the absorbance of the sample, DMSO, and control, respectively.

Statistical analysis of cellular viability. The statistical significance of disparities between control and exposed cells was evaluated by one-way ANOVA, followed by Dunnett's test using the Sigma Plot 12.5 software (Systat Software Inc.). A value of $p < 0.05$ was considered statistically significant.

Microscopy sample preparation. MNT-1 cells were grown on glass coverslips and cultured in the presence of the $(Gd_{0.97}Yb_{0.02}Er_{0.01})_2O_3$ nanoparticles at 25 and 100 µg·mL^{-1} dispersed in culture medium, for 24 h. After that, cells were fixed with 4% paraformaldehyde in PBS for 10 min. Following washes with PBS and deionized water, coverslips were mounted onto glass slides with 4',6-diamidino-2-phenylindole (DAPI)-containing Vectashield mounting medium (Vector Labs).

3.7. THERMOMETRY BASED ON EXCITATION SPECTRA.

3.8. THERMOMETRIC PARAMETERS BASED ON EXCITATION SPECTRA OF LANTHANIDE IONS: THEORY.

Consider a system with a manifold of low-lying states a, b, c, ..., (in increasing order of energy) denoted collectively as α, and a set of high-lying excited states e, f, g, ... (in increasing order of energy), named β. Some of these low-lying states e.g., a, b, c, are thermally coupled. Thus, an excitation spectrum monitored at a given emission wavelength related to the emission from state e will have bands corresponding to transitions from the thermally coupled states (e.g., $a, b,$ and c) to some of the high-lying excited states (e.g., $i,$ and j). In addition, the energy separations between adjacent levels in α and β are larger than 10000 $\mathrm{cm^{-1}}$. With these energy separations, the transitions within the manifold α and within the set β are dominated by nonradiative decay rates, W_{nr}, which can be expressed as [63]:

$$W_{\mathrm{nr}}(T) = \frac{C e^{-\alpha \Delta E}}{[1 - e^{-\tilde{\nu}_{\mathrm{max}}/(k_{\mathrm{B}}T)}]^{\Delta E/\tilde{\nu}_{\mathrm{max}}}} \qquad \text{Equation 10}$$

where C and α are positive-definite constants characteristic of a given material at low temperatures, ΔE (in $\mathrm{cm^{-1}}$) is the energy separation between the states, $\tilde{\nu}_{\mathrm{max}}$ (in $\mathrm{cm^{-1}}$) is the maximum phonon wavenumber, and k_{B} ($= 0.695035\ \mathrm{cm^{-1}\ K^{-1}}$) is Boltzmann constant. Adjusted values of $\tilde{\nu}_{\mathrm{max}}$, C, and α for some matrices (crystals) are available [64], for instance, they are, respectively, 175 $\mathrm{cm^{-1}}$, $1.2 \times 10^{10}\ \mathrm{s^{-1}}$ and 1.9×10^{-2} cm for $LaBr_3$ and 400 $\mathrm{cm^{-1}}$, $3.5 \times 10^{7}\ \mathrm{s^{-1}}$ and 3.8×10^{-3} cm for $LiYF_4$. As a result, transitions between states within α and β will be dominated by nonradiative rates between adjacent levels, whereas transitions from β to α will be dominated by radiative rates and will be much smaller than those within α and β. An energy level diagram with the most relevant transitions is depicted in Figure 7.

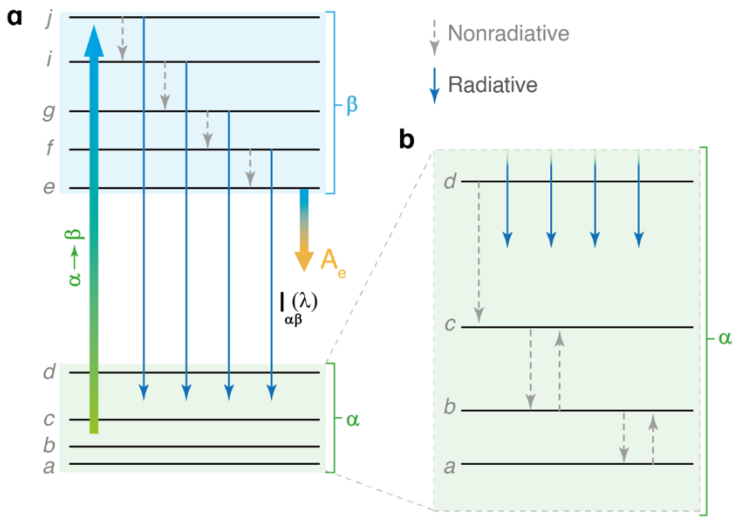

Figure 7. Simplified energy level scheme used to describe the excitation spectrum from a manifold of low-lying, denoted collectively as α, where $\alpha = a, b, c, \ldots$ (in increasing order of energy), to a set of high-lying excited states, denoted collectively as β, where $\beta = e, f, g, \ldots$ (in increasing order of energy). The low-lying levels a, b, and c are thermally coupled. Dashed arrows represent nonradiative transitions and solid arrows correspond to radiative transitions. Source: Author.

The low-lying states *a*, *b*, and *c* are thermally coupled because the energy separations between them are small (usually < 1500 cm^{-1}), thus, the decaying rates are very large and thermal excitations (backward transitions) are also necessary and should have large rates to ensure thermal equilibrium. Thus, only these states should contribute to the excitation spectrum because their sizable thermal populations ensure that enough ions can be excited, whereas their thermal couplings ensure they are repopulated fast enough so that steady-state emission can be reached.

In addition, the bands in the excitation and emission spectra should be narrow so that, despite the energy separation between the states being small, they do not overlap. All these requirements are fulfilled by some lanthanide ions, for instance, Eu(III). Indeed, spectral bands of Eu(III) based compounds and materials are narrow and almost no-overlaps are observed. This ion presents a manifold of low-lying levels with the following energies: $^7F_0$ 0.0, $^7F_1$ 372,

$^7F_2$ 1026, $^7F_3$ 1666, $^7F_4$ 2823, $^7F_5$ 3849, and $^7F_6$ 4907 cm^{-1} as well as a set of high-lying excited levels: $^5D_0$ 17293, $^5D_1$ 19027, $^5D_2$ 21483, $^5D_3$ 24355, $^5L_6$ 25325 cm^{-1}, ... obtained for the free ion in LaF_3 crystal [65]. Due to the special features of the lanthanide ions, these energy levels remain practically with same energies in different environments, including complexes with organic ligands, crystals, nanoparticles, coordination polymers, etc. in fact, these values differ less than 2% (except for $^7F_3$) compared to those of the free ion [66] for the manifold ^7F_J and less than 0.5% for the manifold ^5D_J and other high-lying excited states. It can be observed that the energy separations between the adjacent levels vary from ca. 370 to 2900 cm^{-1} and that that $^7F_0$, $^7F_1$, and $^7F_2$ levels are thermally coupled at temperatures up to 400 K, and above this temperature, the $^7F_3$ level may be considered thermally coupled. Thus, it is usual to observe excitations from $^7F_0$ and $^7F_1$ levels, as well as from $^7F_2$ level in favorable cases. These excitations can be monitored at ca. 615 nm corresponding to the $^5D_0 \longrightarrow {}^7F_2$ transition, because it is most intense. However, for reasons of spectral window or specific applications, it can be monitored at ca. 700 nm corresponding to the $^5D_0 \longrightarrow {}^7F_4$ transition. For some matrices with small nonradiative decays within the set of excited states, emissions from $^5D_1$ and possibly $^5D_2$ can also be observed, which will be relevant for a calibration free thermometer.

The intensity, $I_{\alpha\beta}$, of an emission from an excited state e within set β to a given state within manifold α, is proportional to the product of the radiative emission rate from e level, A_e, and the number of the emitters in e state, $N_e(\alpha \rightarrow \beta)$, when the excitation occurs from a state in manifold α to a state in set β, i.e., $I_{\alpha\beta} \propto A_e N_e(\alpha \rightarrow \beta)$.[66-67] The intensities of the transitions in the excitation spectrum are proportional to the areas of the respective bands in the spectrum, where the proportionality constant depends on the experimental setup (e. g., slits, geometry, detector, excitation source, etc.). If all experimental parameters are maintained fixed

while the excitation spectrum is recorded, then the ratio of the excitation intensities becomes the ratio of the respective areas. So, taking the thermometric parameter $\Delta^{\alpha\beta}_{\alpha'\beta'}$ as the ratio of $I_{\alpha\beta}$ and $I_{\alpha'\beta'}$ integrated intensities in the excitation spectrum yields,

$$\Delta^{\alpha\beta}_{\alpha'\beta'} \equiv \frac{I_{\alpha\beta}}{I_{\alpha'\beta'}} = \frac{S^{\mathrm{ex}}_{\alpha\to\beta}}{S^{\mathrm{ex}}_{\alpha'\to\beta'}} = \frac{N_e(\alpha\to\beta)}{N_e(\alpha'\to\beta')} \qquad \text{Equation 11}$$

where $S^{\mathrm{ex}}_{\alpha\to\beta}$ and $S^{\mathrm{ex}}_{\alpha'\to\beta'}$ are the areas under the bands associated with $\alpha\to\beta$ and $\alpha'\to\beta'$ transitions, respectively, in the excitation spectrum. Because the $I_{\alpha\beta}$ and $I_{\alpha'\beta'}$ intensities are monitored at the same wavelength with the same experimental parameters, the proportionality constant and the radiative emission rate A_e cancel in the ratio and justifies the last equality in Equation 11. It is noteworthy that the thermometric parameter $\Delta^{\alpha\beta}_{\alpha'\beta'}$ in Equation 11 is independent of the mode of acquisition (rate of energy or of photons) of spectra. Under continuous excitation, $N_e(\alpha\to\beta)$ and $N_e(\alpha'\to\beta')$, appearing in the Equation 11, become the number of the emitters in the emitting e level at steady-state when the excitation leads to the $\alpha\to\beta$ and $\alpha'\to\beta'$ transitions, respectively.

The number of ions at each state is governed by a set of rate equations, which relates the rate of change of the number of ions with the net pathways that populate and depopulate that level. These rate equations can be setup for the energy levels and transitions depicted in figure 2, which yield (see Annexes 9.1. page 106)

$$\frac{\mathrm{d}N_\alpha(t)}{\mathrm{d}t} = -\frac{\mathrm{d}N_\beta(t)}{\mathrm{d}t} = \sum_{\beta''}^{e,f,g,\dots}\sum_{\alpha''}^{a,b,c,\dots} k_{\beta''\alpha''}N_{\beta''}(t) - k_{\alpha'\beta'}N_{\alpha'}(t) \qquad \text{Equation 12}$$

where $N_\alpha(t)$ and $N_\beta(t)$ are the sum of the number of ions in the α manifold of low-lying states and in the β set of high-lying excited states, respectively, i.e.

$$N_\alpha(t) = \sum_{\alpha''}^{a,b,c,\ldots} N_{\alpha''}(t)\,, \qquad N_\beta(t) = \sum_{\beta''}^{e,f,g,\ldots} N_{\beta''}(t) \qquad \text{Equation 13}$$

Notice that the rates of change of the total number of ions in α and β depend only on the decaying rates from the β set to the α manifold, $k_{\beta''\alpha''}$, and on the excitation rate $k_{\alpha'\beta'}$. This is valid, despite the complexity of the energy level diagram and transitions in Figure 7, including the forward and backward transitions amongst the thermally coupled levels.

At the steady-state regime, the rates of change become null, that is, $\mathrm{d}N_\alpha/\mathrm{d}t = \mathrm{d}N_\beta/\mathrm{d}t = 0$, and the following expression can be obtained for the number of ions in the emitting level, N_e,

$$k_{e\alpha}N_e(\alpha' \to \beta') = k_{\alpha'\beta'}N_{\alpha'} - \sum_{\beta''}^{f,g,\ldots}\sum_{\alpha''}^{a,b,c,\ldots} k_{\beta''\alpha''}N_{\beta''} \cong k^{\mathrm{abs}}_{\alpha'\to\beta'}N_{\alpha'}, \qquad \text{Equation 14}$$

$$k_{e\alpha} = \sum_{\alpha''}^{a,b,c,\ldots} k_{e\alpha''}$$

where the number of ions in each state are constant or no longer dependent on time.

Considering that the excitation source is not too powerful, the number of ions in the high-lying excited states $f, g, \ldots$ are then vanishing small, because the transition rates from high-lying excited states $k_{\beta\alpha}$ are much smaller than the decay rates within the set of excited states $k_{\beta\beta'}$, which justifies the approximation in Eq. 11, where the rate associated with the $\alpha' \to \beta'$ excitation, $k^{\mathrm{abs}}_{\alpha'\to\beta'}$, has been made explicit. Under these assumptions, the thermometric parameter defined in Eq. 8 becomes,

$$\Delta^{\alpha\beta}_{\alpha'\beta'} = \frac{S^{\mathrm{ex}}_{\alpha\to\beta}}{S^{\mathrm{ex}}_{\alpha'\to\beta'}} = \frac{N_e(\alpha \to \beta)}{N_e(\alpha' \to \beta')} = \frac{k^{\mathrm{abs}}_{\alpha\to\beta}N_\alpha}{k^{\mathrm{abs}}_{\alpha'\to\beta'}N_{\alpha'}} \qquad \text{Equation 15}$$

where N_α and $N_{\alpha'}$ are the number of ions at steady-state regime upon continuous excitation from α and α' states, respectively. It is important to realize that α and α' states are thermally

coupled and considering that the continuous excitation at each wavelength is turned-on long enough to stablish thermal equilibrium at temperature *T* and the steady-state regime, then the fraction of ions (or population) in the thermally coupled states follows the Boltzmann distribution,

$$\frac{N_\alpha}{N_{\text{t.c.}}} = g_\alpha e^{-E_\alpha/(k_B T)}, \qquad N_{\text{t.c.}} = \sum_{\alpha''=a,b,c}^{\text{t.c.}} N_{\alpha''} \qquad \text{Equation 16}$$

where $N_{\text{t.c.}}$ is the total number of ions in the sample that are in thermally coupled (t.c.) states, g_α and E_α is the degeneracy $(2J+1)$ and energy of a specific state of α set, labeled as α, k_B is the Boltzmann constant. Notice that because the populations of the thermally coupled states depend only on the temperature, then $N_{\text{t.c.}}$ is the same for any excitation.

In addition, this derivation of the thermometric parameter considered the ions (or optical centers) to be independent and isolated. However, for real samples, the ions are placed in a material medium matrix with a refractive index, n, which alters the speed of light and affects the transition rates and measured quantities by a dielectric correction $\chi_{\alpha\to\beta}(n)$. This correction depends on the process or quantity such as absorption, spontaneous emission, cross section, or oscillator strength as well as dipole character, namely, electric dipole (ED) and magnetic dipole (MD) [68]. This is the reason to introduce an explicit dependence on the process (e.g., abs) and on the transition mechanism in the dielectric factor, for instance, $\chi_{\text{ED}}^{\text{abs}}(n)$ or $\chi_{\text{MD}}^{\text{abs}}(n)$, as well as on the transition rates, e.g., $k_{\alpha\to\beta}^{\text{abs}}$ in Eq. 11. The $k_{\alpha\to\beta}^{\text{abs}}$ transition rate should be replaced by $k_{\alpha\to\beta}^{\text{abs}}/\chi_{\alpha\to\beta}^{\text{abs}}(n)$, namely,

$$k_{\alpha\to\beta}^{\text{abs}} \to \frac{k_{\alpha\to\beta}^{\text{abs}}}{\chi_{\alpha\to\beta}^{\text{abs}}(n)}, \qquad \text{Equation 17}$$

where the dielectric correction $\chi_{\alpha\to\beta}^{\text{abs}}(n)$ corresponds $\chi_{\text{ED}}^{\text{abs}}(n)$ or $\chi_{\text{MD}}^{\text{abs}}(n)$ when the $\alpha\to\beta$ transition has an electric dipole (ED) or magnetic dipole (MD) character, respectively. This

dielectric correction takes into consideration the changes of the speed of light in the medium as well as the effects of the local field on the electric dipole. For absorption, these dielectric factors are [68]

$$\chi_{\mathrm{ED}}^{\mathrm{abs}}(n) = n^3\chi_{\mathrm{L}}(n) \cong n^3\left(\frac{n^2+2}{3}\right)^2 \text{ and } \chi_{\mathrm{MD}}^{\mathrm{abs}}(n) = n^5 \qquad \text{Equation 18}$$

where χ_{L} is the local field effects on the electric dipole and the approximation is related to the Lorentz model [68]. Expression of these dielectric factors for emission, cross section, and oscillator strength [68] can be found in the Annexes.

Thus, the thermometric parameter in Eq. 12 becomes,

$$\Delta_{\alpha'\beta'}^{\alpha\beta} = \frac{S_{\alpha\to\beta}^{\mathrm{ex}}}{S_{\alpha'\to\beta'}^{\mathrm{ex}}} = A_{\alpha'\beta'}^{\alpha\beta} e^{-\Delta E_{\alpha\alpha'}/(k_{\mathrm{B}}T)}, \qquad \text{Equation 19}$$

where $\Delta E_{\alpha\alpha'} = E_\alpha - E_{\alpha'}$ is the energy difference between the low-lying α and α' states, and the pre-exponential factor, $A_{\alpha'\beta'}^{\alpha\beta}$, is

$$A_{\alpha'\beta'}^{\alpha\beta} = f(n)\frac{k_{\alpha\to\beta}^{\mathrm{abs}} g_\alpha}{k_{\alpha'\to\beta'}^{\mathrm{abs}} g_{\alpha'}}, \qquad f(n) = \frac{\chi_{\alpha'\to\beta'}^{\mathrm{abs}}(n)}{\chi_{\alpha\to\beta}^{\mathrm{abs}}(n)}, \qquad \text{Equation 20}$$

where $f(n)$ is the dielectric factor, which is 1 when both $\alpha \to \beta$ and $\alpha' \to \beta'$ transitions have the same character, whereas transitions with distinct electromagnetic character it becomes dependent on the refractive index varies with temperature, in principle, $f(n)$ would be temperature dependent. It is noteworthy that $f(n)$ has a weak dependence on n, for instance, a variation of ca. 6.5% in the refractive index around a typical value of 1.55 causes a variation of only 1.2% in the dielectric factor. In addition, the variation of the refractive index with temperature is very small, which can be estimated by the thermo-optic coefficient [69] of the material. At constant pressure, the thermo-optic coefficient is the derivative of the refractive index with respect to the temperature, $\frac{\mathrm{d}n}{\mathrm{d}T}$, which varies from ca. 10^{-4} to 10^{-6} K^{-1} [70]. For

typical oxides, the thermo-optic coefficient is ca. 10^{-5} K^{-1} that yields a variation of ca. 0.2% in a refractive index of 2.0 when the temperature increases from 0 to 400 K. As a result, the expected change of the refractive index with the temperature varying from cryogenic values to 400 K is less than 1%, which causes a negligible variation of the dielectric factor. Thus, $f(n)$ in the pre-exponential factor of the thermometric parameter can be considered independent of the temperature.

It can then be predicted from the thermometric parameter in Figure 15 that, for $\alpha \neq \alpha'$, a plot of the logarithm of $\Delta^{\alpha\beta}_{\alpha'\beta'}$ versus the inverse of temperature, $1/T$, should be linear with slope proportional to $\Delta E_{\alpha\alpha'}$, as long as the energy difference $\Delta E_{\alpha\alpha'}$, remains constant in the temperature range. The proposed thermometric parameter becomes predictable or primary if the absorption transitions rates, $k^{\mathrm{abs}}_{\alpha\to\beta}$, in the pre-exponential factor can be determined. This can be obtained by relating $k^{\mathrm{abs}}_{\alpha\to\beta}$ with the corresponding stimulated, $k^{\mathrm{stim}}_{\beta\to\alpha}$, and spontaneous, $A_{\beta\to\alpha}$, emission rates, which could then be determined from the emission spectrum. So, the thermometric parameter becomes,

$$\Delta^{\alpha\beta}_{\alpha'\beta} = \frac{S^{\mathrm{ex}}_{\alpha\to\beta}}{S^{\mathrm{ex}}_{\alpha'\to\beta}} = A^{\alpha\beta}_{\alpha'\beta} e^{-\Delta E_{\alpha\alpha'}/(k_{\mathrm{B}}T)} \qquad \text{Equation 21}$$

where

$$A^{\alpha\beta}_{\alpha'\beta} = f(n)\frac{S^{\mathrm{em}}_{\beta\to\alpha}(\text{power})}{S^{\mathrm{em}}_{\beta\to\alpha'}(\text{power})} = f(n)\frac{\nu_{\alpha\beta}}{\nu_{\alpha'\beta}}\frac{S^{\mathrm{em}}_{\beta\to\alpha}(\text{photon counting})}{S^{\mathrm{em}}_{\beta\to\alpha'}(\text{photon counting})},$$

$$f(n) = \frac{\chi^{\mathrm{abs}}_{\alpha'\to\beta}(n)}{\chi^{\mathrm{abs}}_{\alpha\to\beta}(n)} \qquad \text{Equation 22}$$

which has calibration completely predictable from the emission spectrum that provides the ratio $\frac{S^{\mathrm{em}}_{\beta\to\alpha}}{S^{\mathrm{em}}_{\beta\to\alpha'}}$, from tabulated values and from the excitation spectrum that gives $\frac{\nu_{\alpha'\beta}}{\nu_{\alpha\beta}}$ in the case of

photon counting measurements, and from the refractive index n in the expression of the dielectric factor $f(n)$. Detailed derivation can be accessed from Annexes.

Thus, the accuracy of the predicted temperature can also be estimated from the pre-exponential factor A and energy difference ΔE, namely

$$T = \frac{\Delta E}{k_{\mathrm{B}} \ln(A/\Delta)} \qquad \text{Equation 23}$$

This shows that the uncertainty in the predicted temperature depends linearly on the energy difference ΔE and has a logarithmic dependence on the pre-exponential factor A and the measured thermometric parameter Δ. As a result, the accuracy of the temperature is also fully predictable, and less prompted to errors from the measured quantities A and Δ.

To evaluate the performance of a thermometer based on a thermometric parameter Δ, the following quantities or parameters must be used: relative thermal sensitivity, spatial and temporal resolution, repeatability, and reproducibility [3a]. One of the most used parameters is the relative thermal sensitivity (S_{r}) of the thermometer, that for the proposed thermometer is also predictable. The relative thermal sensitivity, S_{r}, is given by [3a],

$$S_{\mathrm{r}} = \frac{1}{\Delta}\left|\frac{\mathrm{d}\Delta}{\mathrm{d}T}\right| \qquad \text{Equation 24}$$

Assuming that A is independent of the temperature, leads to

$$S_{\mathrm{r}}^{\alpha,\alpha'} = \frac{1}{\Delta_{\alpha'\beta'}^{\alpha\beta}}\left|\mathrm{d}\Delta_{\alpha'\beta'}^{\alpha\beta}/\mathrm{d}T\right| = \frac{\Delta E_{\alpha\alpha'}}{k_{\mathrm{B}}T^2} \qquad \text{Equation 25}$$

which is fully predictable by knowing $\Delta E_{\alpha\alpha'}$ and it is independent of the pre-exponential factor of the thermometric parameter. This prediction can be tested by measuring the excitation spectra of Eu(III) based compound or material at different temperatures. Taking the (numerical)

derivative of the thermometric parameter at each temperature, the experimental relative thermal sensitivity can be obtained and compared to that predicted by the thermometric equation.

For the proposed thermometer, the self-referencing can be considered, for the general case, as for $\alpha = \alpha'$, which implies $E_{\alpha\alpha'} = 0$, and it can be predicted that the thermometric parameter $\Delta_{\alpha\beta'}^{\alpha\beta}$ becomes

$$\Delta_{\alpha\beta'}^{\alpha\beta} \equiv \frac{S_{\alpha\to\beta}^{\mathrm{ex}}}{S_{\alpha\to\beta'}^{\mathrm{ex}}} = A_{\alpha\beta'}^{\alpha\beta} \ , \qquad \text{Equation 26}$$

which should be constant or independent of temperature and thus could be employed for self-referencing. This prediction can also be tested by measuring the excitation spectra of Eu(III) based compound or material at different temperatures.

Another feature of these thermometric parameters based on the excitation spectrum is the cross-validation. For instance, choosing an appropriate Eu(III) based compound or material, where the emission from the $^5\mathrm{D}_0$ and $^5\mathrm{D}_1$ excited states (e.g. $^5\mathrm{D}_0 \longrightarrow {}^7\mathrm{F}_{0,1,2}$ and $^5\mathrm{D}_1 \longrightarrow {}^7\mathrm{F}_{0,1,2}$) are observed and quantifiable as well as the excitation transitions $^7\mathrm{F}_{0,1} \longrightarrow {}^5\mathrm{D}_0$ and $^7\mathrm{F}_{0,1} \longrightarrow {}^5\mathrm{D}_1$, then the thermometric parameters Δ_{00}^{10} and Δ_{01}^{11} can be promptly obtained, which would predict the same temperature and thus providing cross-validation. In fact, the $^7\mathrm{F}_{0,1} \longrightarrow {}^5\mathrm{D}_0$ and $^7\mathrm{F}_{0,1} \longrightarrow {}^5\mathrm{D}_1$ transitions are commonly observed in the excitation spectra of several Eu(III) compounds and materials and the emissions $^5\mathrm{D}_0 \longrightarrow {}^7\mathrm{F}_{0,1}$ and $^5\mathrm{D}_1 \longrightarrow {}^7\mathrm{F}_{0,1}$ can be observed in compounds with low phonon frequencies, which decreased the nonradiative decay $^5\mathrm{D}_1 \longrightarrow {}^5\mathrm{D}_0$.

As a result, the excitation spectrum of Eu(III)-compounds and materials is robust, simple, and versatile approach to thermometry at nanoscale with complete predictable calibration, relative sensitivity, and accuracy.

Despite significant advancements, only a limited number of primary thermometers have been developed thus far[15], relying on the temperature-dependent characteristics of emission features, such as the peak energy of semiconductor nanoparticles[16] or the intensity emissions of Ln(III) states in thermal equilibrium[11a, 17]. These primary thermometers are equipped with a known thermometric equation that establishes a quantitative relationship between Δ and temperature (T), incorporating well-defined physical constants[17b, 17c]. This capability addresses the primary limitation of secondary thermometers, namely the need for recurrent calibrations when used in different media[3b], exemplified by the ideal gas thermometer's equation linking temperature to measurable quantities such as pressure, volume, and amount of substance, alongside the molar gas constant[71].

These ratiometric luminescent primary thermometers can be categorized into primary-T and primary-S types (Figure 8). Primary-T thermometers rely on a thermometric parameter Δ_0 determined at a known temperature T_0[11a, 17a, 17c-e], often utilizing the ratio of integrated emission intensities of specific transitions of Ln(III) ions. In contrast, primary-S thermometers involve a pre-exponential factor (A) calculated from additional spectral measurements[17b]. Notably, established primary-T thermometers employ the ratio of integrated emission intensities of specific transitions of Er(III) as the Δ parameter, determined by observing decreasing laser power density at a known temperature T_0 until heating effects become negligible. On the other hand, primary-S thermometers, exemplified by the first likely example employing the ratio of emission intensities of Eu(III) transitions, determine A from spectral ratios in the emission spectrum[17c].

Regarding primary-S thermometers, the initial probable instance utilized the ratio of the emission intensities of the Eu(III) $^5D_0 \rightarrow {}^7F_4$ transitions when the $^5D_0$ level is populated from the thermally coupled $^7F_0$, $^7F_1$, and $^7F_2$ levels. It was applied in Y_2O_3:Eu(III) nanocrystals using the Lorentz local-field correction, which relies on the refractive index, for the areas[17b]. The

pre-exponential factor A in Δ was derived from the ratios of the areas of the $^5D_0 \rightarrow {}^7F_1$ or $^5D_0 \rightarrow {}^7F_0$ transitions in the emission spectrum[17b]. This approach most likely prompted investigations into ratiometric thermometric parameters based on the excitation spectra of Ln(III) ions.

Following the approach, it was proposed two new primary thermometers. The so called primary-T which requires a known temperature to be calibrated. The other one primary-S is calibrated using the combination of emission/excitation spectra and, therefore, does not require a known temperature for its calibration. The thermometric equations are shown in the Figure 8 which also illustrate the proposed concept of these primary ratiometric luminescence thermometry.

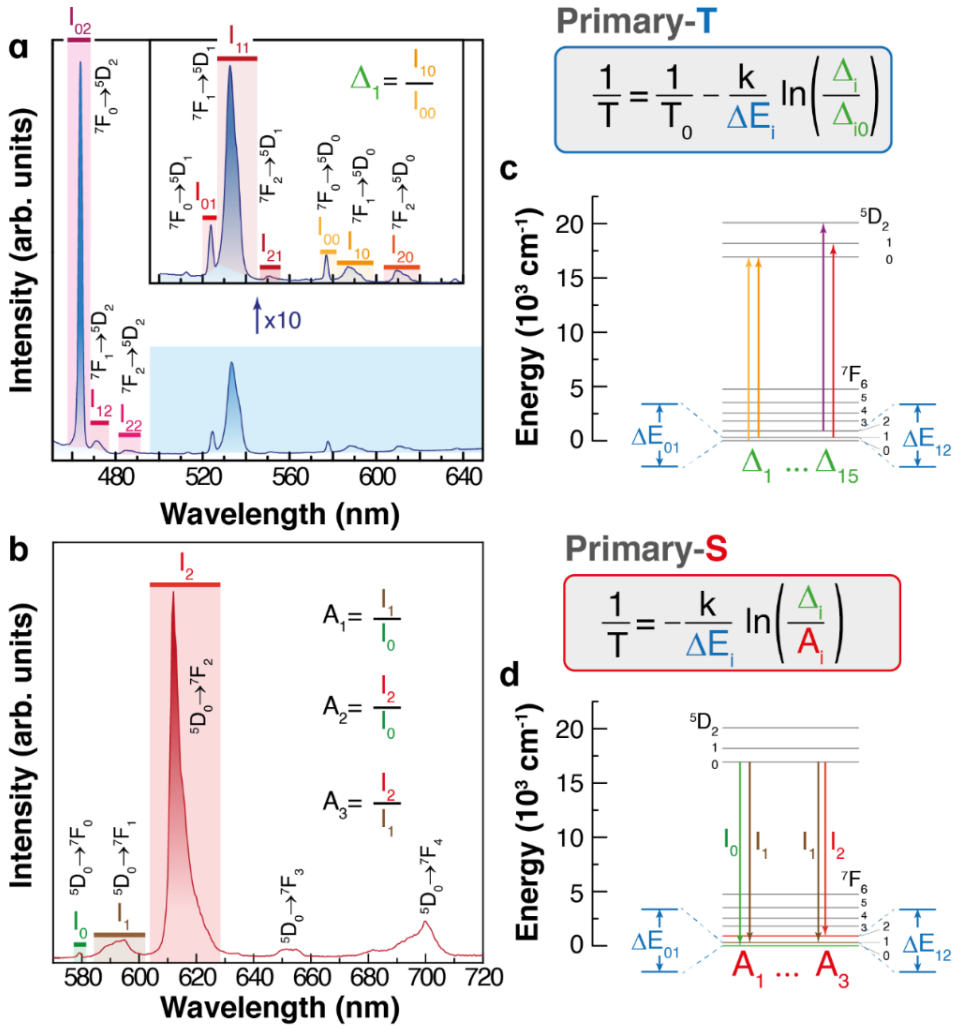

Figure 8. The proposed concept of primary ratiometric luminescence thermometry. Room-temperature (300 K) (a) excitation and (b) emission spectra of the $Eu(hfa)_3bpyO_2$ complex 1 monitored at 700 nm and excited at 338 nm, respectively. The thermometric parameters Δ_i are obtained as ratios of the integrated areas in the excitation spectrum, corresponding to upwards transitions presented in the simplified energy scheme (exemplified for Δ_1). (c) Proper choices of these ratios yield constant (temperature-independent) Δ_i that are employed as self-reference. For primary-T thermometers, Δ_{i0} are the thermometric parameters at a known temperature T_0. For primary-S thermometers, the pre-exponential factors A_i are obtained from the emission spectrum, represented by the downwards arrows in the energy diagram presented in (d). For all thermometers, ΔE_i is the energy difference between the initial levels. Source: Author.

3.9. THERMOMETRY BASED ON EXCITATION SPECTRA: EU(III) COMPLEXES AND NANOPARTICLES.

Before testing these predictions and the proposed primary thermometers, it is important to analyze some properties of complexes and inorganic nanoparticles suitable as thermometers. The most relevant feature of the Eu(III) based compounds is the presence of bands in the excitation spectrum associated with $^7F_{0,1,2} \longrightarrow {}^5D_{0,1,2}$ transitions, which span the spectral range of ca. 450 to 630 nm. For instance, the $^7F_0 \longrightarrow {}^5D_2$ (460-470 nm), $^7F_1 \longrightarrow {}^5D_1$ (530-540 nm), and $^7F_2 \longrightarrow {}^5D_0$ (610-625 nm) transitions have forced electric dipole character and are hypersensitive, whereas $^7F_1 \longrightarrow {}^5D_0$ (585-600 nm) and $^7F_0 \longrightarrow {}^5D_1$ (520-530 nm) are pure magnetic dipole transitions and have intensities that are practically independent of the environment [72]. For the free ion, the energy differences are $\Delta E_{01} = 379\ \text{cm}^{-1}$, $\Delta E_{02} = 1043\ \text{cm}^{-1}$, and $\Delta E_{12} = 664\ \text{cm}^{-1}$ between $^7F_0$, $^7F_1$, and $^7F_2$ levels.[66] Thus, it is expected that excitations from $^7F_2$ of Eu(III) would be observed only at near or higher than room temperature. For complexes, the ligands usually have intense and broad excitation bands that could overlap or even completely mask several 4*f*-4*f* bands. For instance, the excitation spectra of $Eu(hfa)_3bpyO_2$ complex at temperatures ranging from 12 to 340 K are illustrated in Figure 9.

In this work it was analyzed three systems. The first one was $Eu(hfa)_3bpyO_2$ a β-diketone complex with the synthesis described in the experimental session. This complex was fully characterized. The other one was a oxyfluoride bismuth nanoparticle doped with Eu(III), the synthesis and structural and optical characterization was described in details by Zanella and collaborators [53]. The **Table 1** below summarize these two systems as well as the type of spectrum (excitation or emission), spectral range used to obtain the thermometers, and the temperature range used to acquire the spectra (excitation or emission). A third system that will

be presented and discussed in detail in the following section is yttrium oxide, Y_2O_3, nanoparticle doped with Eu(III).

Table 1. List of systems, spectrum type, spectral range, and temperature range from the samples analyzed based on Eu(III).

System	Spectrum type	Spectral range (nm)	Temperature range (K)
Eu(hfa)$_3$bpyO$_2$ complex	Excitation/emission	450-600	12-350
BiF$_3$ nanoparticles	Excitation/emission	450-570	12-340

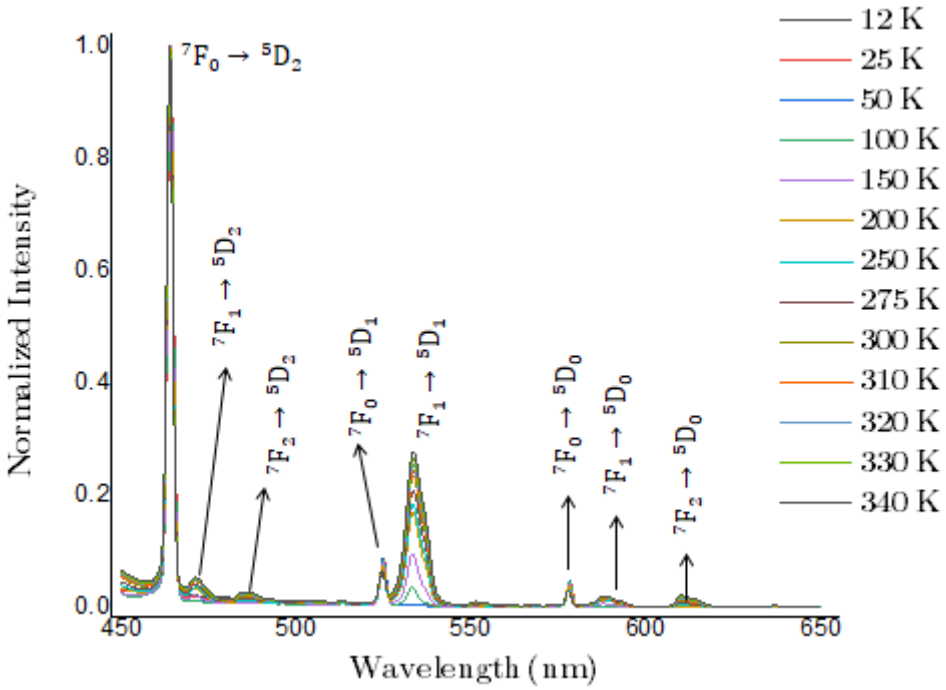

Figure 9. Excitation spectra of the Eu(hfa)$_3$bpyO$_2$ complex 1 monitored at 700 nm at several temperatures from 12 to 340 K, from 450 to 650 nm spectral region. Source: Author.

For the Eu(hfa)$_3$bpyO$_2$ complex, the excitation bands of the ligands (obtained from excitation spectra monitored at 700 nm) do not interfere into the bands associated with 4*f*-4*f* transitions (Figure 9) with wavelengths longer than 450 nm. Therefore, by monitoring the excitation spectra at ca. 700 nm ($^5D_0 \longrightarrow {}^7F_4$), the transitions to the $^5D_0$ level can be observed as shown in Figure 9 for the Eu(hfa)$_3$bpyO$_2$ complex.

Despite being the least intense bands, the $^7F_{0,1,2} \longrightarrow {}^5D_0$ transitions are observed when monitoring the excitation spectra at ca. 700 nm, which could be used to predict the temperature because the corresponding transitions $^5D_0 \longrightarrow {}^7F_{0,1,2}$ in the emission spectrum are observed (primary-S thermometers). Indeed, these three thermometric parameters: $\Delta_{00}^{10} = S^{ex}_{^7F_1 \rightarrow {}^5D_0} / S^{ex}_{^7F_0 \rightarrow {}^5D_0}$, $\Delta_{00}^{20} = S^{ex}_{^7F_2 \rightarrow {}^5D_0} / S^{ex}_{^7F_0 \rightarrow {}^5D_0}$, and $\Delta_{20}^{10} = S^{ex}_{^7F_1 \rightarrow {}^5D_0} / S^{ex}_{^7F_2 \rightarrow {}^5D_0}$ should predict the same temperature, denoted as T_0, which can be determined from the areas of the corresponding emission bands (see Annexes). As a result, it could be used to determine the pre-exponential factor of other more accurate or sensitive thermometric parameters such as $\Delta_{12}^{02} = S^{ex}_{^7F_0 \rightarrow {}^5D_2} / S^{ex}_{^7F_1 \rightarrow {}^5D_2}$ or $\Delta_{01}^{11} = S^{ex}_{^7F_1 \rightarrow {}^5D_1} / S^{ex}_{^7F_0 \rightarrow {}^5D_1}$ or even the hypersensitive transitions $\Delta_{11}^{02} = S^{ex}_{^7F_0 \rightarrow {}^5D_2} / S^{ex}_{^7F_1 \rightarrow {}^5D_1}$. For instance, the pre-exponential factor of the latter thermometer is

$$A_{11}^{02} = \Delta_{11}^{02}(T_0) e^{\Delta E_{01}/(k_B T_0)} \qquad \text{Equation 27}$$

where T_0 is the predicted temperature by primary-S thermometric parameters, e.g., Δ_{00}^{10}, Δ_{00}^{20} or Δ_{20}^{10}, and Δ_{11}^{02} is the thermometric parameter (ratio of the areas $S^{ex}_{^7F_0 \rightarrow {}^5D_2} / S^{ex}_{^7F_1 \rightarrow {}^5D_1}$) determined at T_0. This is valid for transitions from the $^5D_0$ level in the emission spectra to $^7F_{0,1,2}$ levels.

On the other hand, if the emissions from the $^5D_1$ and $^5D_2$ Eu(III) excited states can be observed, then the thermometric parameters Δ_{01}^{11} or Δ_{12}^{02} mentioned above could be employed to predict the temperature (primary-S). Indeed, inorganic matrices are quite suitable for this application because the presence of high energy phonons could be avoided, thus allowing emission from $^5D_1$ and $^5D_2$ levels to be observed. For instance, bismuth oxyfluoride nanoparticles, α-BiO_yF_{3-2y}, doped with [73] Eu(III) ions present typical excitation band 4*f*-4*f* bands in addition to an intense broad band centered at 275 nm assigned to a ligand-to-metal charge-transfer band associated with O^{2-} and Eu(III) ions, monitored at 591 nm ($^5D_0 \longrightarrow {}^7F_1$

transition). The emission spectrum, upon excitation at 393 nm ($^7F_0 \longrightarrow {}^5L_6$ transition), in the 570-700 nm region, presents bands assigned to typical $^5D_0 \longrightarrow {}^7F_J$ with $J = 0$ to 4 transitions as well as bands associated with $^5D_1 \longrightarrow {}^7F_{0,1,2}$ and $^5D_2 \longrightarrow {}^7F_3$ transitions [73]. Eu(III)-doped bismuth oxyfluoride nanoparticles (e.g., BiF_3:Eu1 as 1% Eu(III) doping BiF_3:Eu5 as 5% Eu(III) doping) were prepared by Zanella *et al.* [53] from the Department of Molecular Sciences and Nanosystems from Ca' Foscari University of Venice and were chosen to test and validate this new excitation thermometer because in addition to their photophysical properties, they are simple, fast, and reproducible to synthesize with quantitative doping with Eu(III) and average crystallite values of 80 and 81 nm, which agree with the average sizes of 81 ± 5 and 87 ± 8 nm determined from SEM micrographs. Excitation spectra of BiF_3:Eu1 (1% Eu(III) doped) nanoparticles monitored at 612 nm at several temperatures ranging from 50 to 340 K are illustrated in Figure 10. Notice that emissions from the $^5D_1$ Eu(III) level are observed [53].

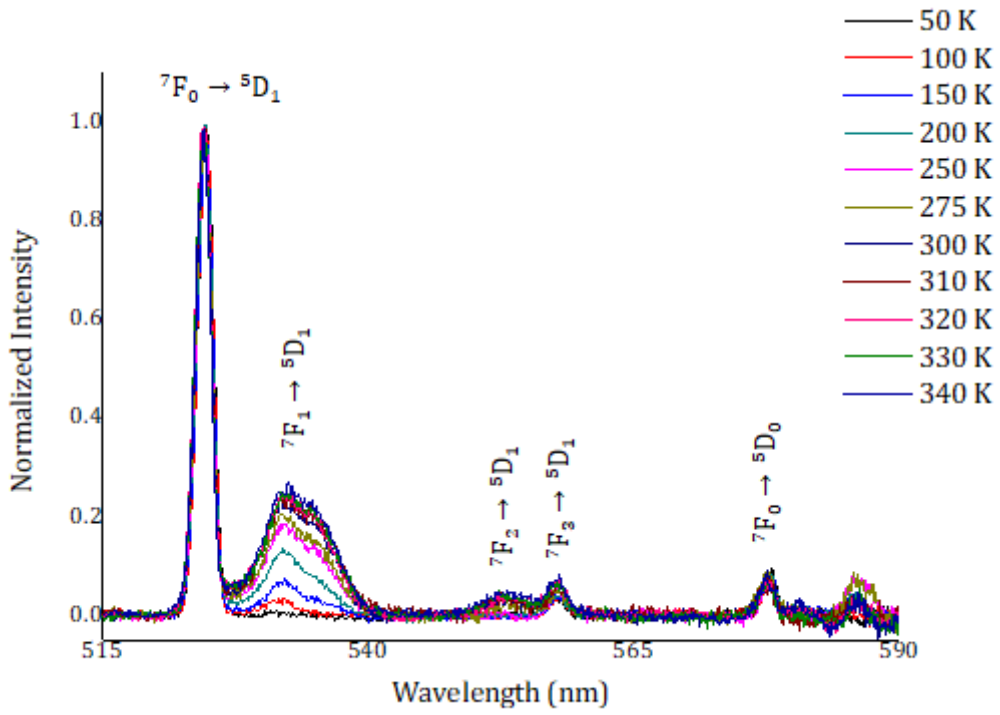

Figure 10. Excitation spectra of BiF_3:Eu1 nanoparticles monitored at 612 nm at several temperatures from 50 to 340 K. Source: Author.

3.10. THERMOMETRY BASED ON RATIOMETRIC INTENSITY IN EXCITATION SPECTRA OF LANTHANIDE IONS: VALIDATION.

The predicted linearity of the logarithm of the thermometric parameter and the inverse of temperature according to Equation 15 has been observed for several transitions from excitation spectrum in different complexes and nanoparticles (Figure 11).

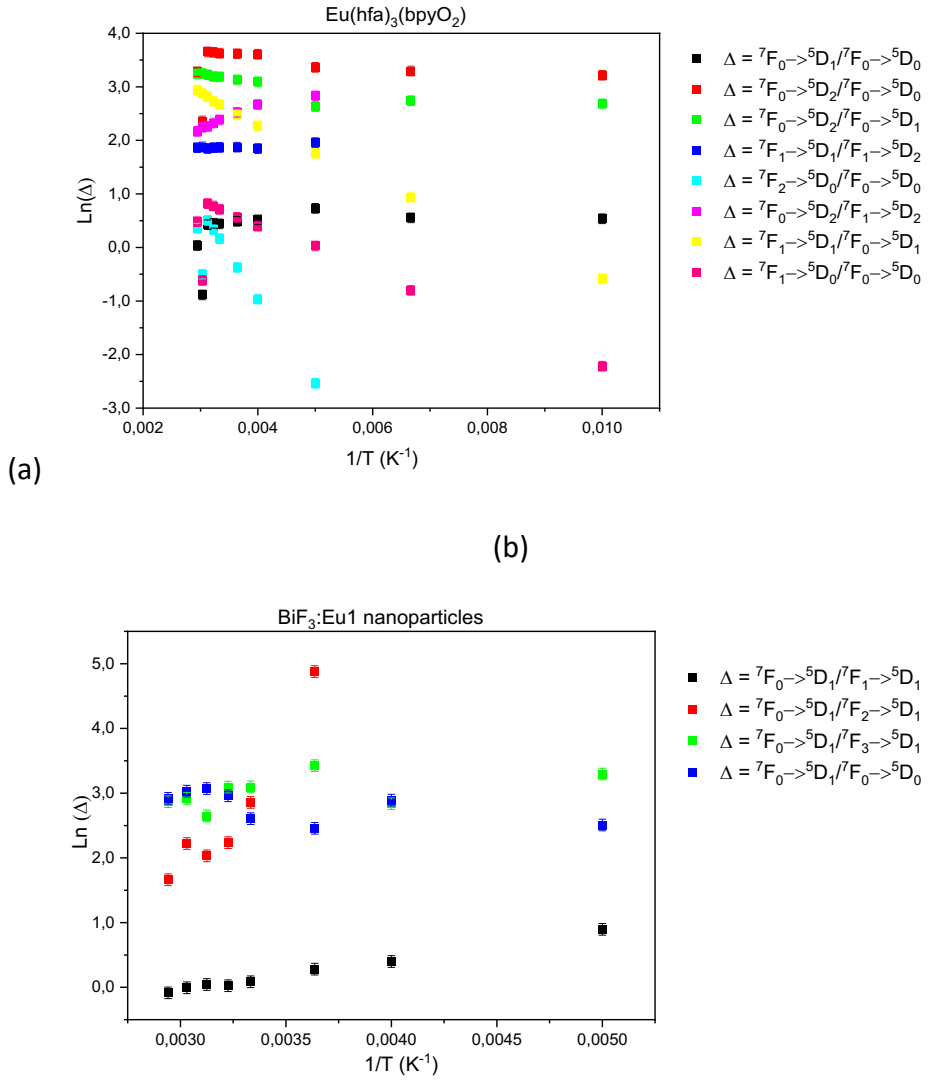

Figure 11. Arrhenius plot of the thermometric parameter Δ for the $Eu(hfa)_3bpyO_2$ complex between 100 and 330 K (excitation spectrum monitored at 700 nm) (a) and BiF_3:Eu1 nanoparticles between 50 to 340 K (b). Source: Author.

For the $Eu(hfa)_3bpyO_2$ complex the excitation spectrum (see Figure 9) monitored at 700 nm at several temperatures from 12 to 340 K show well defined bands at 525 and 534 nm assigned to the $^7F_0 \rightarrow {}^5D_1$ and $^7F_1 \rightarrow {}^5D_1$ transitions [66], respectively. These bands do not overlap with the ligands and their integration (522 and 527.5 nm, and from 527.5 to 544 nm) can be performed directly to provide the thermometric parameter Δ_{01}^{11}. A plot of $\ln \Delta_{01}^{11}$ vs. $1/T$ for the temperature range from 200 to 320 K yields a straight line with slope $-\Delta E_{01}/k_B = -553 \pm 37.3$ K and correlation coefficient $R^2 = 0.965$. The estimated value of $\Delta E_{01} = (553\ \text{K}) \times (0.695\ \text{cm}^{-1}\ \text{K}^{-1}) = 384\ \text{cm}^{-1}$ coincides almost perfectly with the energy difference of 379 cm^{-1} of the free-ion levels $^7F_1$ and $^7F_0$ for Eu(III).[66] The intercept is $\ln \Delta_{01}^{11} = 4.48 \pm 0.14$, then $\Delta_{01}^{11} = 88.2$. Also, the predicted relative sensitivity is obtained from Equation 24 as, $S_r = (\Delta E_{01}/k_B)/T^2 = (55200/T^2)\%\ \text{K}^{-1}$, that yields $S_r = (5.1 - 0.8)\%\ \text{K}^{-1}$ for $T =$ 100 to 330 K. However, because the emissions from the $^5D_1$ level could not be observed, this pre-exponential factor could not be determined (Figure 12a).

As mentioned, this linear behavior of $\ln \Delta$ versus T^{-1} is predicted as long as ΔE is constant (independent of the temperature). However, the thermal expansion/contraction can affect the energy difference and cause deviation from linearity [74]. Indeed, if the behavior of $\ln \Delta$ versus T^{-1} is analyzed in a greater temperature interval (12 to 330 K), the correlation coefficient $R^2 = 0.99252$ and the slope yields estimated value of $\Delta E_{01} = 340.4\ \text{cm}^{-1}$, in poor agreement with the free ion value (Figure 12b). Other parameters, experimental setup and/or selected systems can provide better results.

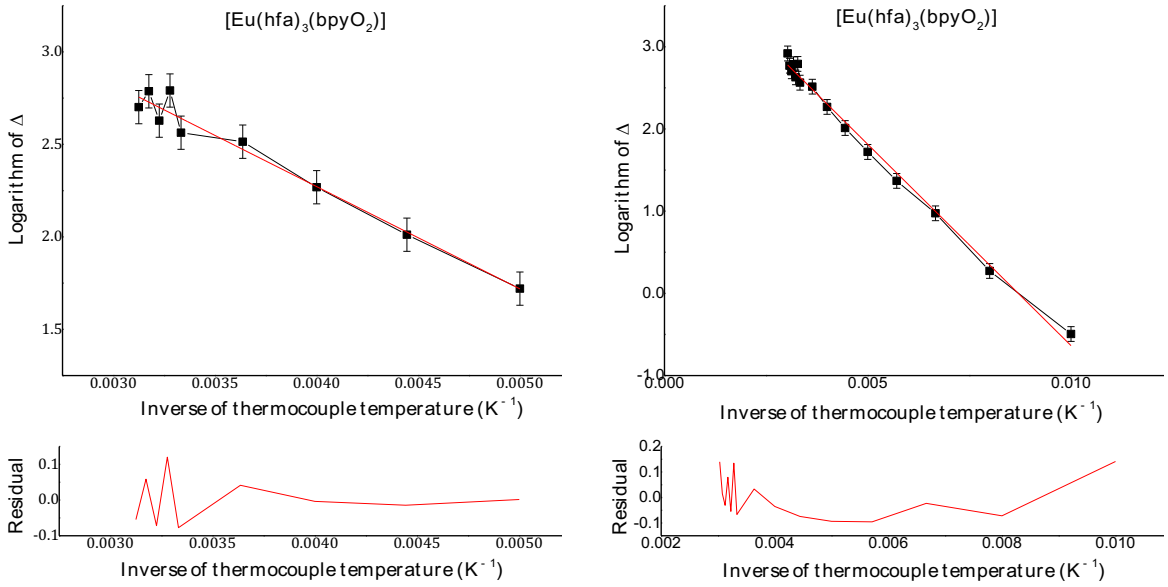

(a) (b)

Figure 12. Linear fit of the logarithm of the thermometric parameter Δ_{01}^{11} obtained from excitation intensities of the $^7F_1 \rightarrow {}^5D_1$ (S_1^{ex}) and $^7F_0 \rightarrow {}^5D_1$ (S_2^{ex}) transitions monitored at 700 nm in the $Eu(hfa)_3bpyO_2$ complex as a function of the inverse of temperature at several temperatures from (a) 200 to 320 K (estimated value of $\Delta E_{01} = 384.5\ cm^{-1}$ and correlation coefficient $R^2 = 0.965$) and (b) 12 to 330 K (estimated value of $\Delta E_{01} = 340.4\ cm^{-1}$ and correlation coefficient $R^2 = 0.9925$). Source: Author.

Assuming that A is independent of the temperature (Eq. 16), S_r is fully predictable by knowing $\Delta E_{\alpha\alpha'}$ (Eq. 22) and it is independent of the pre-exponential factor of the thermometric parameter. As a result, for example, the thermometric parameters Δ_{01}^{11} and Δ_{12}^{02} must have the same relative sensitivity (e.g. $\Delta E_{01}/k_B \cong 545.3$ K [66], whereas Δ_{21}^{01} and Δ_{22}^{01} must be almost three times more sensitive, $\Delta E_{02}/k_B \cong 1500.6$ K) [66]. This prediction was tested by measuring the excitation spectra of Eu(III) based compound or material at different temperatures. Taking the (numerical) derivative of the thermometric parameter at each temperature, the experimental relative thermal sensitivity can be obtained and compared to that predicted by the thermometric equation, as shown, for example, for thermometric parameter Δ_{01}^{11} obtained from $^7F_1 \rightarrow {}^5D_1$ and $^7F_0 \rightarrow {}^5D_1$ transitions monitored at 700 nm for the $Eu(hfa)_3bpyO_2$ complex as a function of the inverse of square temperature at several temperatures (Figure 13 and Figure 14).

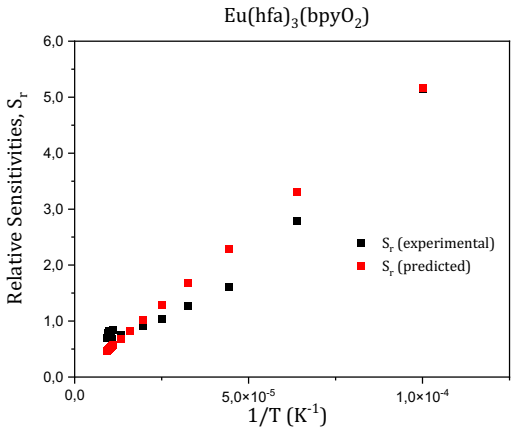

Figure 13. Relative thermal sensitivity (S_r) obtained for the thermometric parameter Δ_{01}^{11} ($^7F_1 \rightarrow {}^5D_1$ and $^7F_0 \rightarrow {}^5D_1$ transitions monitored at 700 nm) for the temperature interval from 100 to 330 K, considering the adjusted value of $\Delta E = 358.5\ cm^{-1}$ for the $Eu(hfa)_3bpyO_2$ complex as a function of the inverse of square temperature. Source: Author.

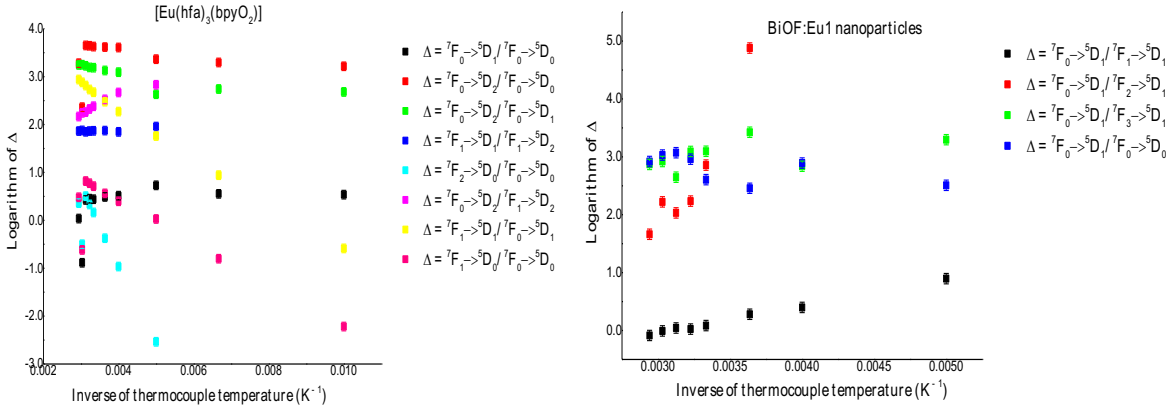

Figure 14. Relative thermal sensitivity (S_r) obtained for the thermometric parameter (a) Δ_{00}^{10} ($^7F_1 \rightarrow {}^5D_0$ and $^7F_0 \rightarrow {}^5D_0$ transitions monitored at 700 nm) for the temperature interval from 200 to 340 K, and considering $\Delta E = 232.5\ cm^{-1}$; and (b) Δ_{01}^{11} ($^7F_1 \rightarrow {}^5D_1$ and $^7F_0 \rightarrow {}^5D_1$ transitions monitored at 700 nm, excluding the temperature of 50 K) for the temperature interval from 100 to 330 K, and considering the adjusted value of $\Delta E = 325\ cm^{-1}$, for the $Eu(hfa)_3bpyO_2$ complex as a function of the inverse of square temperature. Source: Author.

It is noteworthy that the pre-exponential factor $\Delta_{\alpha'\beta}^{\alpha\beta}$ can be obtained independently from the emission spectrum at the same temperature, whereas the exponent $\Delta E_{\alpha\alpha'}/k_{\mathrm{B}}$ can be obtained directly from the excitation spectrum or from known values for the free ion (e.g., $\Delta E_{01}/k_{\mathrm{B}} = 545.3$ K, [66] for Δ_{11}^{10}). Note that the dielectric correction is practically independent on the temperature because the thermo-optic coefficients ($\partial n/\partial T$) are very small for these solid samples. Thus, for example, the thermometric parameter Δ_{11}^{10} has a fully predictable calibration, as long as the $^5\mathrm{D}_1 \longrightarrow {}^7\mathrm{F}_0$ and $^5\mathrm{D}_1 \longrightarrow {}^7\mathrm{F}_1$ transitions are quantified in the emission spectrum. In addition, this thermometric parameter has predictable relative thermal sensitivity and calculable accuracy.

In fact, other excitation transitions such as $^7\mathrm{F}_0 \longrightarrow {}^5\mathrm{D}_0$ ($S^{\mathrm{ex}}_{^7\mathrm{F}_0\rightarrow{}^5\mathrm{D}_0}$) (FED, 570-585 nm) and $^7\mathrm{F}_1 \longrightarrow {}^5\mathrm{D}_0$ ($S^{\mathrm{ex}}_{^7\mathrm{F}_1\rightarrow{}^5\mathrm{D}_0}$) (MD, 585-600 nm) or $^7\mathrm{F}_0 \longrightarrow {}^5\mathrm{D}_0$ ($S^{\mathrm{ex}}_{^7\mathrm{F}_0\rightarrow{}^5\mathrm{D}_0}$) and $^7\mathrm{F}_2 \longrightarrow {}^5\mathrm{D}_0$ ($S^{\mathrm{ex}}_{^7\mathrm{F}_2\rightarrow{}^5\mathrm{D}_0}$) (FED, 605-625 nm) can provide thermometric parameters $\Delta_{00}^{10} = S^{\mathrm{ex}}_{^7\mathrm{F}_1\rightarrow{}^5\mathrm{D}_0}/S^{\mathrm{ex}}_{^7\mathrm{F}_0\rightarrow{}^5\mathrm{D}_0}$ or $\Delta_{00}^{20} = S^{\mathrm{ex}}_{^7\mathrm{F}_2\rightarrow{}^5\mathrm{D}_0}/S^{\mathrm{ex}}_{^7\mathrm{F}_0\rightarrow{}^5\mathrm{D}_0}$, respectively, that have predictable calibrations, relative sensitivities, and accuracies, if the reverse transitions are observed in the emission spectrum. Therefore, the excitation spectrum can provide several thermometric parameters with known and general expressions $\Delta = Ae^{-\Delta E/(k_{\mathrm{B}}T)}$.

Thus, the temperature predictions were obtained from Equation 23 for all selected systems from different thermometric parameter. For example, for the Δ_{00}^{10} obtained from excitation spectrum monitored at 700 nm for the $Eu(hfa)_3bpyO_2$ complex at 300 K (Figure 9),

$$\Delta_{00}^{10} = \frac{S^{\mathrm{ex}}_{^7\mathrm{F}_1\rightarrow{}^5\mathrm{D}_0}}{S^{\mathrm{ex}}_{^7\mathrm{F}_0\rightarrow{}^5\mathrm{D}_0}} = \frac{0.11680}{0.05723} = 2.041.$$

The areas were obtained by integrating the bands between 576 and 580.5 nm (maximum at 578 nm) for the $^7F_0 \longrightarrow {}^5D_0$ transition and between 589.5–597.5 nm (maximum at 589 nm) for the $^7F_1 \longrightarrow {}^5D_0$ transition.

The wavenumber of these transitions, obtained from gaussian fit, are: $\tilde{\nu}_{^5D_0-{}^7F_0} = 17247\ \text{cm}^{-1}$ and $\tilde{\nu}_{^5D_0-{}^7F_1} = 16880\ \text{cm}^{-1}$, yielding

$$\frac{\nu_{^5D_0-{}^7F_1}}{\nu_{^5D_0-{}^7F_0}} = \frac{16880}{17247} = 0.97872.$$

The following ratio was determined from the emission spectra (at 300 K):

$$\frac{S^{\text{em}}_{^5D_0\rightarrow{}^7F_1}}{S^{\text{em}}_{^5D_0\rightarrow{}^7F_0}} = 9.3414;$$

for excitation at 338 nm. Because the thermometric parameters involve f-f transitions, the emission spectrum should have been obtained by exciting at some intra-4*f* transition, e.g., $^7F_{0,1} \longrightarrow {}^5L_6$ (390–405, 400–410 nm). Thus, it is better to choose the closest excitation wavelength to the intra-4*f* transition, namely, 338 nm.

Considering a refractive index of $n = 1.60$, the dielectric correction factor becomes

$$\frac{(n^2+2)^2}{9n^2} = 0.9025.$$

Thus, the pre-exponential factor is

$$A_{00}^{10} = \frac{(n^2+2)^2}{9n^2}\frac{S^{\text{em}}_{^5D_0\rightarrow{}^7F_1}(\text{power})}{S^{\text{em}}_{^5D_0\rightarrow{}^7F_0}(\text{power})} = 0.9025 \times 9.3414 = 8.4306$$

or

$$A_{00}^{10} = \frac{\nu_{^5\mathrm{D}_0-{}^7\mathrm{F}_1}}{\nu_{^5\mathrm{D}_0-{}^7\mathrm{F}_0}} \frac{(n^2+2)^2}{9n^2} \frac{S^{\mathrm{em}}_{^5\mathrm{D}_0\rightarrow{}^7\mathrm{F}_1}(\text{photon counting})}{S^{\mathrm{em}}_{^5\mathrm{D}_0\rightarrow{}^7\mathrm{F}_0}(\text{photon counting})} = 0.97872 \times 0.9025 \times 9.3414$$

$$= 8.2512$$

where $S^{\mathrm{em}}_{\beta\rightarrow\alpha}(\text{power})$ and $S^{\mathrm{em}}_{\beta\rightarrow\alpha}(\text{photon counting})$ is the area of the band in the emission acquired as energy per unit of time (power) and as number of photons per unit of time (photon counting), respectively.

Using the adjusted free-ion value $\Delta E_{10} = 294.1\ \mathrm{cm}^{-1}$ gives $\Delta E_{10}/k_{\mathrm{B}} = 423.1$ K, and the predicted temperature is

$$T = \frac{\Delta E_{10}}{k_{\mathrm{B}}} \frac{1}{\ln(a_{00}^{10}/\Delta_{00}^{10})} = \frac{423.1\ \mathrm{K}}{1.4185} = 298.3\ \mathrm{K}$$

or

$$T = \frac{\Delta E_{10}}{k_{\mathrm{B}}} \frac{1}{\ln(a_{00}^{10}/\Delta_{00}^{10})} = \frac{423.1\ \mathrm{K}}{1.3978} = 302.1\ \mathrm{K}$$

where both values agree very well with the expected temperature 300 K, and for this particular case, the measurements of the emission intensity (photon counting versus power) do not greatly affect the predicted temperature. This same procedure was used to obtain others predicted temperatures for this system, from different thermometric parameter for a refractive index $n = 1.55$ and different selected system.

As mentioned, a self-referencing thermometer is characterized by a thermometric parameter that does not vary with the temperature. In fact, employing the ratio of excitation intensities corresponding to transitions from the same initial state (e.g. $^7\mathrm{F}_0$ or $^7\mathrm{F}_1$) to distinct excited states (e.g. $^5\mathrm{D}_0$ and $^5\mathrm{D}_1$ or $^5\mathrm{D}_1$ and $^5\mathrm{D}_2$) provides a thermometric parameter that remains constant with changes in the temperature. For instance, the Eu(III) transitions from the

ground state such as $^7F_0 \longrightarrow {}^5D_1$ (MD, 520−530 nm) and $^7F_0 \longrightarrow {}^5D_2$ (FED, 460−470 nm) are fairly intense and commonly observed in the excitation spectrum. Thus,

$$\Delta_{01}^{02} = \frac{S^{ex}_{^7F_0 \rightarrow {}^5D_2}}{S^{ex}_{^7F_0 \rightarrow {}^5D_1}} = \frac{15n^2}{(n^2+2)^2} \frac{S^{em}_{^5D_2 \rightarrow {}^7F_0}}{S^{em}_{^5D_1 \rightarrow {}^7F_0}}$$

provides a thermometric parameter that is constant with the temperature and larger than 1, because the transition $^7F_0 \longrightarrow {}^5D_2$ is hypersensitive. However, it is very difficult to predict because emissions from the $^5D_2$ level is rarely observed. On the other hand, the $^7F_0 \longrightarrow {}^5D_1$ and $^7F_0 \longrightarrow {}^5D_0$ (FED, 570−585 nm) transitions can also be observed in the excitation spectrum and

$$\Delta_{00}^{01} = \frac{S^{ex}_{^7F_0 \rightarrow {}^5D_1}}{S^{ex}_{^7F_0 \rightarrow {}^5D_0}} = \frac{(n^2+2)^2}{3n^2} \frac{S^{em}_{^5D_1 \rightarrow {}^7F_0}}{S^{em}_{^5D_0 \rightarrow {}^7F_0}},$$

is also a constant thermometric parameter that can be predicted for compounds with observable emissions from $^5D_1$ and $^5D_0$ levels. Note, however, that the $^7F_0 \longrightarrow {}^5D_0$ (FED, 570−585 nm) transition is at the limit of the spectral corrections of the most common excitation sources (*ca*. 580 nm).

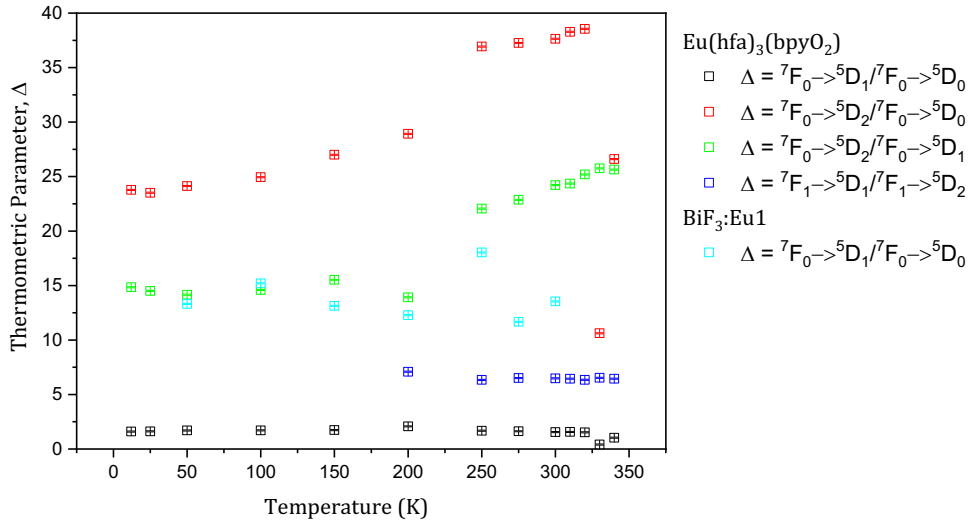

Figure 15. Dependence of different thermometric parameters in Eq. 23 obtained from the ratio of excitation intensities corresponding to transitions from the same initial state to distinct excited states for $Eu(hfa)_3bpyO_2$ complex monitored at 700 nm and for BiF_3:Eu1 nanoparticles monitored at 612 nm. Source: Author.

In addition, two or more selected transitions provide ratios that must give the same temperature, thus quantifying the accuracy of a measured temperature. For the $Eu(hfa)_3bpyO_2$ complex, this feature of the predicted temperatures was validated for the Δ_{00}^{10} and Δ_{00}^{20} thermometers obtained from the excitation spectra monitored at 700 nm for a temperature range of 200 to 300 K. The best values of the predicted temperature (compared to the observed temperature) were, for Δ_{00}^{10} parameter, 97 K (100 K), 143 K (150 K), 201 K (200 K), 246 K (250 K), 274 K (275 K), and 304 K (300 K), with standard deviation of 2.1, 4.9, 0.7, 2.8, 0.7, 2.8, 6.4 and 6.4, respectively; and for Δ_{00}^{20} parameter, the best predicted values were 196 and 201 K (200 K), 251 and 254 (250 K), 283 and 287 K (275 K), with standard deviation of 2.6, 2.1 and 5.3, respectively.

3.11. TEMPERATURE PREDICTION USING SINGLE THERMOMETERS APPROACH: Y_2O_3:Eu^{3+} NANOPARTICLES.

Building on the aforementioned methodology, a distinct system was employed to validate the temperature and relative thermal sensitivity predictions. The excitation spectra of Y_2O_3:Eu^{3+} nanoparticles, was obtained in a narrow range of excitation, but the limited number of excitation bands, as illustrated in Figure 16, can be used to derive six thermometers, denoted as Δ_{21}^{01}, Δ_{11}^{01}, Δ_{01}^{11}, Δ_{21}^{11}, Δ_{11}^{21}, and Δ_{01}^{21}.

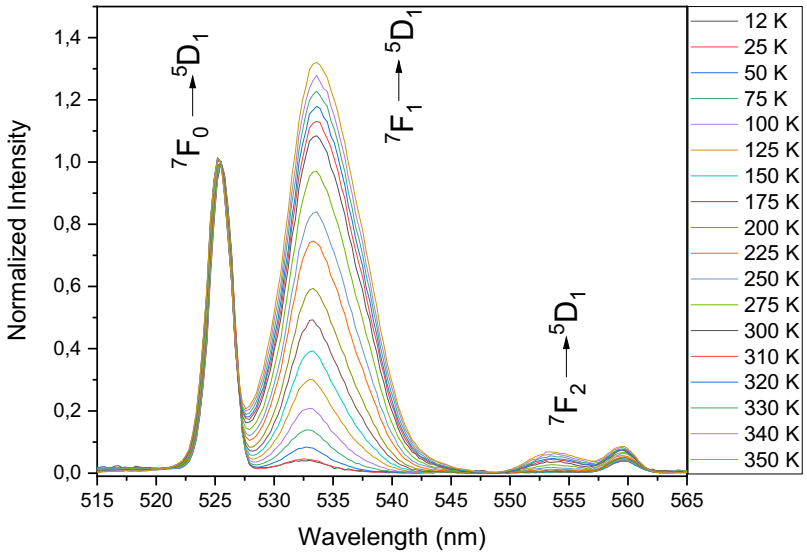

Figure 16. Excitation spectra of Y_2O_3:Eu^{3+} (5% Eu^{3+}) excited at 396 nm and monitored at 614 nm recorded from 12 to 350 K. Source: Author.

After the selection of thermometers, the following step involves predicting the temperature and determining the relative thermal sensitivity using a single thermometer, employing the primary thermometer equation proposed above. Figure 17 illustrates the

temperature prediction and the estimation of relative thermal sensitivity utilizing the designated single thermometer, denoted as Δ_{01}^{11}.

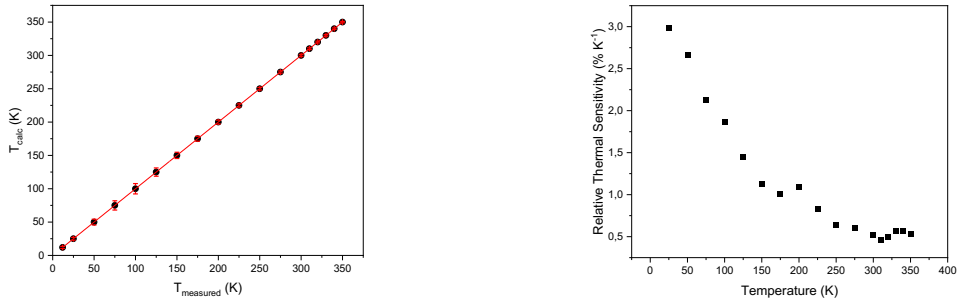

Figure 17. (a) Temperature prediction and (b) relative thermal sensitivity using the thermometer Δ_{01}^{11} in the temperature range from 200 to 350 K. Source: Author.

Figure 17a shows a remarkable agreement between the predicted and the measured temperatures. In addition, a substantial relative thermal sensitivity of 2.98% was observed for temperatures ranging from 12 to 350 K. To refine both the temperature prediction and enhance the thermal sensitivity, a multiparametric linear regression was employed. Building on recent advancements [75] that explore alternatives for improving such estimations, this approach was adopted to optimize the accuracy of temperature predictions and enhance the precision of relative thermal sensitivity estimates with respect to those using a single thermometer.

3.12. ON THE MULTIPARAMETRIC LINEAR REGRESSION (MLR) TO PREDICT THE TEMPERATURE AND IMPROVE THE RELATIVE THERMAL SENSITIVITY.

Recent advances in the field of luminescence nanothermometry have approached the limits of precision achievable by nanothermometers [76]. Consequently, there is a pressing need to explore novel methodologies for obtaining luminescent thermal probes with reduced uncertainty, especially for applications in both *in vitro* and *in vivo* thermal sensing [77]. Two potential approaches are being considered to minimize δT. The first approach involves enhancing the sensitivity of light detectors and the use of brighter materials to increase the signal-to-noise ratio, thereby leading to a reduction in $\delta\Delta/\Delta$. The second approach focuses on enhancing S_r, which can be achieved through either the development of new materials or developing new strategies to define the thermometric parameter. From now on, it is shown how the use of multiparametric linear regression was used to predict the temperature and to calculate the relative thermal sensitivity.

Multiparametric linear regression, also known as multiple linear regression, is a statistical method used for analyzing the relationship between a dependent variable (or response variable) and two or more independent variables (or predictor variables). It extends the principles of simple linear regression, where only one predictor variable is considered, to situations where multiple variables may influence the outcome. This technique is widely employed in various fields, including economics, social sciences, epidemiology, and natural sciences, to model complex relationships and make predictions based on multiple factors.

In a multiparametric linear regression model, the goal is to find the best-fitting linear equation that describes how changes in the predictor variables relate to changes in the dependent variable. The equation takes the form:

$$Y = \beta_0 + \beta_1 X_1 + \beta_2 X_2 + \cdots + \beta_n X_n + \varepsilon \qquad \text{Equation 28}$$

where Y represents the dependent variable to be predicted, X_1, X_2, ..., X_n are the independent variables or predictors, β_0 is the intercept, which represents the value of Y when all predictor variables are zero, β_1, β_2, ..., β_n are the regression coefficients, indicating the change in Y associated with a one-unit change in the corresponding predictor variable, while holding all other predictors constant, and ε represents the error term, which accounts for the variability in Y that cannot be explained by the predictor variables.

The coefficients β_0, β_1, β_2, ..., β_n are estimated from the available data using various statistical techniques, with the primary aim of minimizing the sum of squared errors (the differences between the predicted and actual values of Y). This process is typically performed using software tools like statistical packages or programming languages.

Multiparametric linear regression provides valuable insights into how multiple factors jointly affect the dependent variable. Researchers can assess the significance of each predictor, quantify their individual contributions, and assess the overall goodness of fit of the model. Additionally, it allows for making predictions and understanding the strength and direction of relationships between variables. However, it assumes that the relationships are linear and that the error terms are normally distributed and independent.

In summary, multiparametric linear regression is a powerful statistical tool employed to model and comprehend intricate relationships among multiple independent variables and a dependent variable. This technique plays a pivotal role in data analysis and predictive modelling across diverse fields.

Broadly speaking, the method for predicting temperature and the relative thermal sensitivity hinges on the statistical manipulations discussed in **Section 9.1.4.** regarding thermometry based on excitation spectra. The same equations and assumptions, as detailed earlier, were applied. These spectra were recorded utilizing the same setup, and the spectral areas were derived post-deconvolution using Gaussian fits.

Emphasizing the benefits of obtaining excitation spectra for temperature prediction is crucial, particularly when dealing with shorter spectral ranges that expedite the acquisition process. While it is true that employing more sophisticated equipment and longer acquisition times can be perceived as potential drawbacks in excitation spectrum-based thermometers, there are strategies available to mitigate these challenges. One effective approach is to limit the number of excitation bands recorded within a narrower spectral range or, alternatively, to utilize excitation intensities at specific wavelengths instead of scanning the entire spectral range. These wavelengths should be carefully selected from the peaks of bands with similar widths, thereby optimizing the efficiency of the temperature prediction process.

The equation for temperature prediction and the calculation of the relative thermal sensitivity as well as their uncertainty for the multiparametric linear regression was described in the literature [75] and they were applied here to estimate the temperature and the relative thermal sensitivity. Equation 23 becomes the temperature prediction using the multiparametric linear regression with up to six thermometers yields,

$$T = \beta_0 + \sum_{i=1}^{n} \beta_i \Delta_i + \varepsilon \qquad \text{Equation 29}$$

where T represents the temperature, Δ_i are the thermometric parameters obtained from the excitation spectra ($\Delta_{\alpha'\beta}^{\alpha\beta}$), β_0 is the intercept, β_i are the regression coefficients used to predict

the temperature ($i \neq 0$), ε represents the error term from the multiparametric regression, and n was varied from 2 to 6.

The temperature uncertainty is obtained considering the uncertainty associated with each thermometer, as follows, [75]

$$\frac{\delta\Delta_i}{\Delta_i} = \sqrt{\left(\frac{\delta I_1}{I_1}\right)^2 + \left(\frac{\delta I_2}{I_2}\right)^2}, \qquad \Delta_i = \frac{I_1}{I_2} \qquad \text{Equation 30}$$

and

$$\delta T = \frac{1}{S_\mathrm{r}} \sqrt{\sum_{i=1}^{n} \left(\frac{\delta\Delta_i}{\Delta_i}\right)^2} \qquad \text{Equation 31}$$

where I_1 and I_2 are the intensities (determined by the areas of the transitions in the spectrum) used to define thermometer Δ_i, and S_r is the relative thermal sensitivity. For the multiparametric linear regression the following expression has been postulated for the relative thermal sensitivity [75]

$$S_\mathrm{r} = \sqrt{\sum_{i=1}^{n} \left(\frac{1}{\Delta_i} \left|\frac{\partial\Delta_i}{\partial T}\right|\right)^2} = \sqrt{\sum_{i=1}^{n} \left(\Delta_i \left|\frac{\partial T}{\partial\Delta_i}\right|\right)^{-2}} \qquad \text{Equation 32}$$

Considering the model is a linear multiparametric one, the partial derivatives $\partial T/\partial\Delta_i$ can be promptly obtained and S_r becomes

$$S_r = \sqrt{\sum_{i=1}^{n} (\Delta_i \beta_i)^{-2}} \qquad \text{Equation 33}$$

The chosen system for applying multiparametric linear regression to enhance temperature and relative thermal sensitivity predictions was the Y_2O_3:Eu^{3+} nanoparticles, as depicted in Figure 16 above.

Upon examining the excitation spectra of Y_2O_3:Eu^{3+} nanoparticles, certain Eu(III) transitions became evident, namely $^7F_0 \longrightarrow {}^5D_1$, $^7F_1 \longrightarrow {}^5D_1$, and $^7F_2 \longrightarrow {}^5D_1$. With these transitions identified, it was possible to compute different thermometric parameters $\Delta_{\alpha'\beta'}^{\alpha\beta}$ by combining these Eu(III) transitions. A combination of up to six thermometers was utilized, including Δ_{21}^{01}, Δ_{11}^{01}, Δ_{01}^{11}, Δ_{21}^{11}, Δ_{11}^{21}, and Δ_{01}^{21}, to predict temperature and relative thermal sensitivity. The selection and combination of these thermometers were made randomly, and a method for choosing and performing multiparametric linear regression is currently in development. It is worth noting that these thermometric parameters, now referred to as thermometers, exhibit temperature dependence consistent with the europium complex described earlier. Emphasizing the significance of uniform conditions, it is relevant to note that these thermometric parameters can be readily compared. This is attributed to their acquisition under identical energy conditions. Notably, these parameters lack specific units, as they are derived as ratios of areas (proportional to the intensities).

Once the thermometers were chosen, multiparametric linear regression could be applied to predict temperature and relative thermal sensitivity as shown in Table 2. Figure 18 illustrates the temperature and relative thermal sensitivity within a temperature range of 12 to 350 K using 2, 4, and 6 thermometers. It is evident that increasing the number of thermometers leads to improved predictions of temperature and relative thermal sensitivity. Notably, the relative thermal sensitivity demonstrates a substantial performance improvement, ranging from 10 to 1000-fold when compared to single thermometer predictions for both temperature and relative thermal sensitivity (Figure 17).

Table 2. Temperature prediction (K) and the relative thermal sensitivity (K^{-1} and % K^{-1}) using the combination of 2, 4, and 6 thermometers ranging from 12 to 350 K.

	2 thermometers			4 thermometers			6 thermometers		
***T* (K)**	T_{calc}	S_r	$\%S_r$	T_{calc}	S_r	$\%S_r$	T_{calc}	S_r	$\%S_r$
12	1,22	0,01	0,81	9,05	0,82	82,42	12,63	1,48	147,70
25	18,62	0,01	0,98	24,60	0,62	62,01	21,71	1,24	124,37
50	72,05	0,02	1,93	58,22	0,30	29,70	53,71	1,30	129,99
75	105,76	0,03	3,45	79,66	0,18	18,33	79,52	2,09	208,53
100	123,02	0,06	5,57	99,21	0,16	15,89	100,41	3,27	326,89
125	139,51	0,09	8,62	122,39	0,20	19,67	125,41	4,86	485,95
150	140,02	0,12	11,80	145,57	0,26	25,66	144,35	6,73	672,84
175	163,71	0,15	15,26	167,48	0,33	32,78	170,92	7,94	794,15
200	166,72	0,19	19,48	195,82	0,42	41,63	194,54	10,07	1006,92
225	187,69	0,26	25,94	235,45	0,55	55,32	231,09	12,25	1224,86
250	249,24	0,30	30,29	250,85	0,65	64,60	255,74	10,10	1010,34
275	270,23	0,36	35,56	277,80	0,76	75,83	276,92	10,21	1020,82
300	306,82	0,41	40,98	299,45	0,87	87,38	299,13	8,40	839,61
310	318,66	0,43	43,11	307,93	0,92	91,91	308,60	7,69	768,78
320	325,26	0,45	45,00	316,42	0,96	95,94	316,23	7,36	736,40
330	333,11	0,48	47,54	327,87	1,01	101,35	326,77	6,95	695,02
340	341,95	0,50	50,43	340,55	1,07	107,50	340,45	6,38	638,17
350	348,38	0,53	53,30	353,67	1,14	113,61	353,86	5,99	598,84

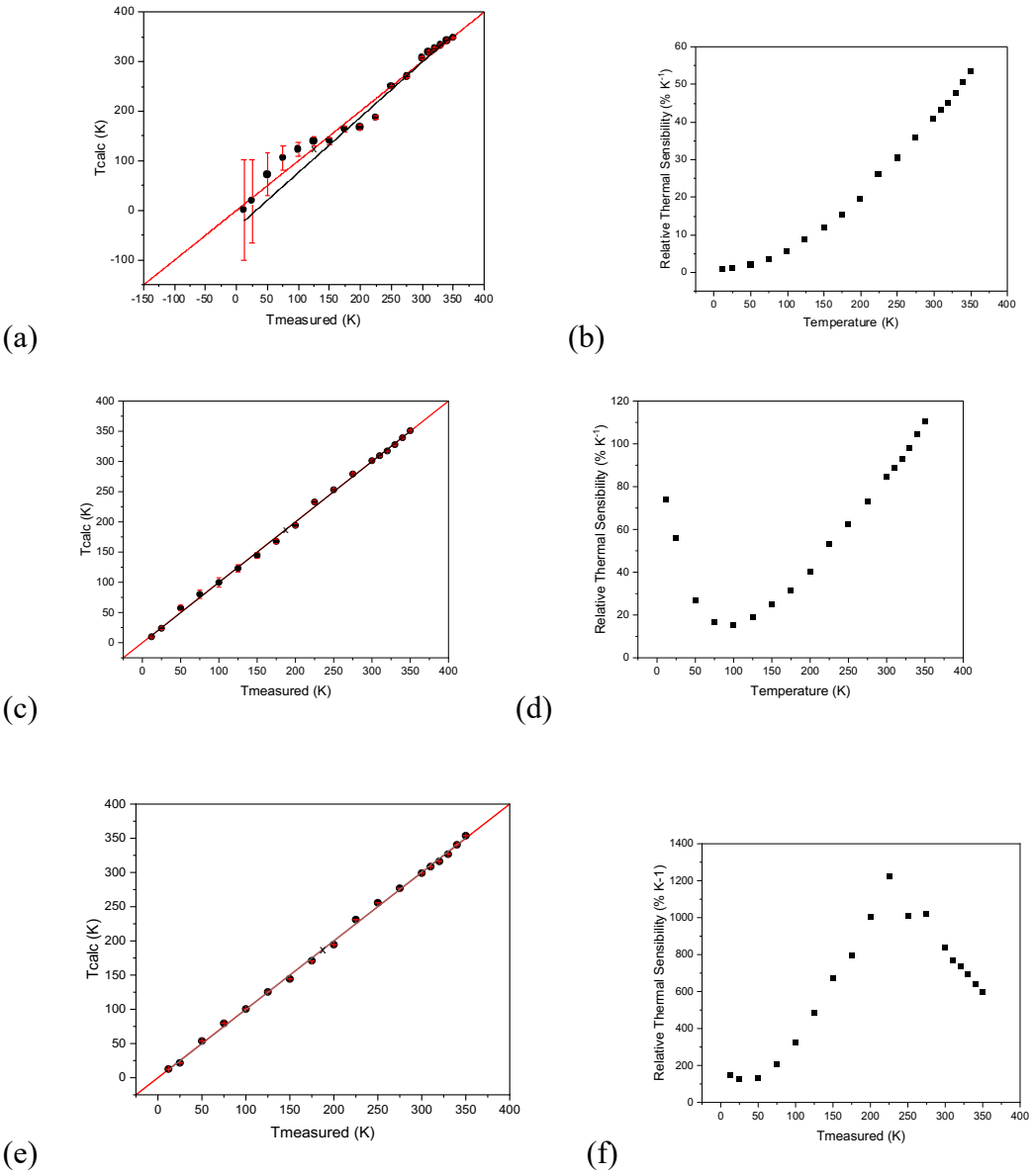

Figure 18. Correlation between the temperature measured with the temperature calculated using the multilinear regression with (a) 2-, (c) 4-, and (e) 6-thermometers; the corresponding relative thermal sensibility of (b) 2-, (d) 4-, and (f) 6-thermometers in the temperature range from 12 to 350 K. Source: Author.

The temperature predictions derived from this combination of thermometers were averaged and compared to temperature measurements obtained using a silicon diode, as illustrated in Figure 18.

The Table 3 provides information about the percentage contribution of each thermometer to temperature predictions using multiparametric linear regression models with 2, 4, and 6 thermometers. The percentages in the table represent the importance of each thermometer in predicting temperature at different temperature levels (12, 25, 50, 75, 100, 125, 150, 175, 200, 225, 250, 275, 300, 310, 320, 330, 340, and 350 K) for the different model configurations (2-, 4-, and 6-thermometer).

Table 3. Percentage contribution of each thermometer in the temperature prediction using 2-, 4-, and 6-thermometers in the multiparametric linear regression.

	2		4				6					
T	Δ_{21}^{01}	Δ_{11}^{01}	Δ_{21}^{01}	Δ_{11}^{01}	Δ_{01}^{11}	Δ_{21}^{11}	Δ_{21}^{01}	Δ_{11}^{01}	Δ_{01}^{11}	Δ_{21}^{11}	Δ_{11}^{21}	Δ_{01}^{21}
12	22.73%	77.27%	0.12%	0.04%	19.87%	79.97%	0.00%	0.01%	88.05%	3.72%	8.07%	0.14%
25	14.13%	85.87%	0.19%	0.11%	21.42%	78.28%	0.00%	0.02%	76.46%	2.93%	20.36%	0.22%
50	3.56%	96.44%	0.79%	2.09%	21.30%	75.82%	0.00%	0.08%	16.15%	0.60%	82.95%	0.21%
75	1.20%	98.80%	2.17%	17.46%	16.61%	63.76%	0.00%	0.11%	1.92%	0.08%	97.82%	0.08%
100	0.48%	99.52%	2.84%	57.30%	7.94%	31.92%	0.00%	0.11%	0.30%	0.01%	99.55%	0.03%
125	0.22%	99.78%	1.95%	86.87%	2.09%	9.10%	0.00%	0.12%	0.06%	0.00%	99.80%	0.01%
150	0.11%	99.89%	1.12%	95.46%	0.65%	2.78%	0.00%	0.12%	0.02%	0.00%	99.86%	0.01%
175	0.08%	99.92%	0.82%	97.72%	0.24%	1.22%	0.00%	0.15%	0.01%	0.00%	99.84%	0.00%
200	0.05%	99.95%	0.52%	98.92%	0.09%	0.47%	0.00%	0.15%	0.00%	0.00%	99.85%	0.00%
225	0.03%	99.97%	0.35%	99.44%	0.03%	0.18%	0.00%	0.18%	0.00%	0.00%	99.82%	0.00%
250	0.05%	99.95%	0.52%	99.27%	0.02%	0.19%	0.00%	0.36%	0.00%	0.00%	99.64%	0.00%
275	0.05%	99.95%	0.51%	99.35%	0.01%	0.14%	0.00%	0.48%	0.00%	0.00%	99.52%	0.00%
300	0.07%	99.93%	0.75%	99.09%	0.00%	0.15%	0.00%	0.94%	0.00%	0.00%	99.05%	0.00%
310	0.09%	99.91%	0.90%	98.93%	0.00%	0.17%	0.00%	1.24%	0.00%	0.00%	98.75%	0.00%
320	0.10%	99.90%	0.98%	98.85%	0.00%	0.17%	0.00%	1.48%	0.00%	0.00%	98.52%	0.00%
330	0.11%	99.89%	1.10%	98.73%	0.00%	0.17%	0.00%	1.85%	0.00%	0.00%	98.14%	0.00%
340	0.13%	99.87%	1.31%	98.51%	0.00%	0.18%	0.00%	2.47%	0.00%	0.00%	97.52%	0.00%
350	0.15%	99.85%	1.49%	98.32%	0.00%	0.18%	0.01%	3.13%	0.00%	0.00%	96.86%	0.00%

By analyzing Table 3 it is possible to address some correlations and implications:

1. **Thermometer Count:** it was evaluated three different models with 2-, 4-, and 6-thermometers. As the number of thermometers increases, the contribution of each thermometer to the prediction changes.

2. **Temperature:** several temperatures, ranging from 12 to 350 K, were considered. It is essential to note that the contribution of each thermometer varies with temperature.

3. **Percentage Contribution:** the percentage values in Table 3 quantify the contribution of each thermometer to the temperature prediction. These values are calculated based on the coefficients, β_i, associated with each thermometer in the multiparametric linear regression models.

Let us now present and discuss some key observations:

- **Higher Thermometer Counts:** moving from the 2-thermometer model to the 6-thermometer model, it can be observed a shift in the distribution of percentage contributions. In the 2-thermometer model, one thermometer tends to dominate the prediction (77.27%), but in the 6-thermometer model, the distribution is more evenly spread.

- **Varying Contributions with Temperature:** the contribution of each thermometer to the prediction varies significantly with the temperature. For example, at 12 K, the first thermometer has a contribution of 22.73% in the 2-thermometer model, while in the 4-thermometer model, it contributes only 0.12%. This demonstrates that the importance of thermometers can change based on the temperature being predicted.

- **Redundancy:** in some cases, thermometers have negligible contributions (close to 0%) to the prediction. This suggests that certain thermometers may not be providing

meaningful information for temperature prediction at specific temperature levels in a given model.

- **Cumulative Contributions:** the cumulative contribution of the thermometers can also be calculated. For instance, in the 2-thermometer model, the cumulative contribution of the first thermometer reaches 100% at 12 K. This means that, for this specific temperature, the first thermometer is the sole predictor in the 2-thermometer model.

- **Diminishing Contributions:** as the number of thermometers increases, the individual contributions decrease. In the 6-thermometer model, the contributions are more evenly spread among the thermometers.

In summary, this table provides valuable insights into how different thermometers contribute to temperature predictions in multiparametric linear regression models. It highlights the dynamic nature of these contributions, which depend on both the number of thermometers used and the temperature ranges being predicted. This information can be used to optimize the selection and configuration of the thermometers for accurate temperature predictions in various scenarios. It was selected three different model configurations to illustrate the scenario depict on Table 3. **Figure 19** provides a visual representation of the thermometer contributions to temperature prediction using different configurations of thermometers. Specifically, it shows the influence of 2 thermometers in (a), 4 thermometers in (b), and 6 thermometers in (c) on the accuracy of temperature predictions. This figure is instrumental in visually conveying the varying degrees of importance associated with each thermometer, shedding light on the dynamic nature of their contributions in different modeling scenarios.

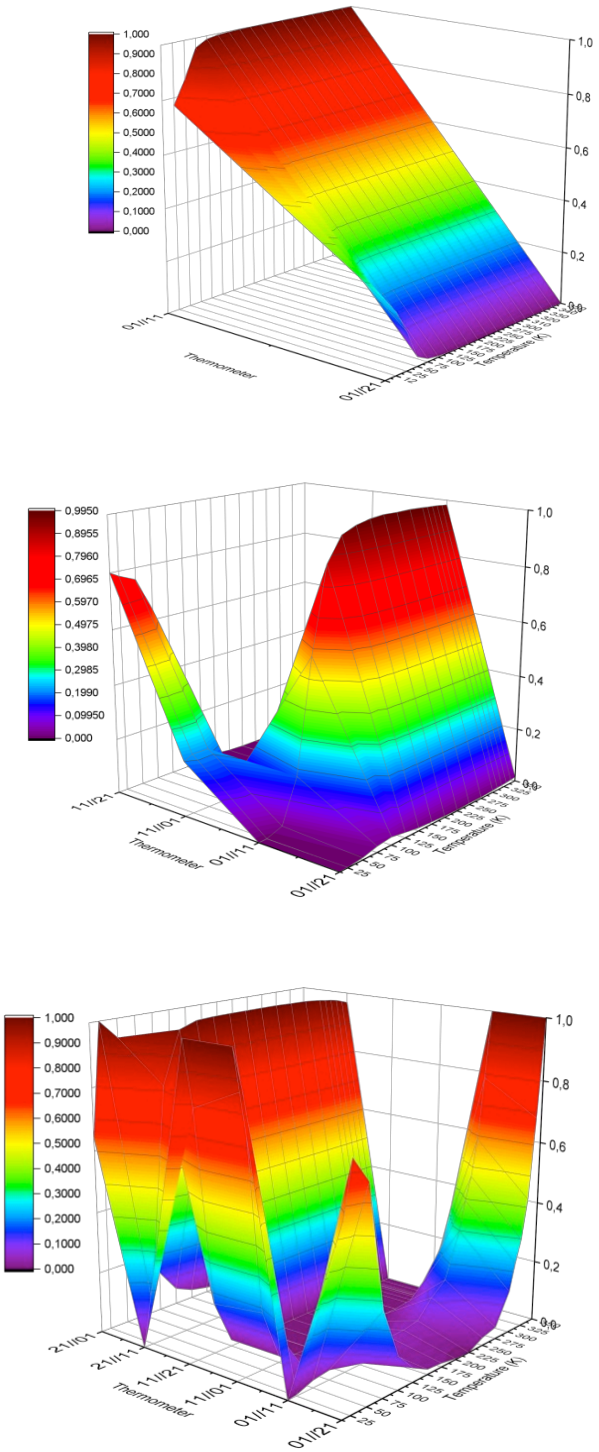

Figure 19. Contributions of each thermometer for the temperature prediction using (a) 2-thermometer, (b) 4-thermometer, and (c) 6-thermometer in multiparametric linear models. Source: Author.

This comparison revealed a significant gain in accuracy and precision, a twofold improvement compared to the regression obtained using the combination of six thermometers

employed in the europium nanoparticles mentioned earlier. Table 4 presents the mean signed deviation (MSD) and the mean unsigned deviation (MUD) with respect to the temperature obtained from multiparametric thermometers.

Table 4. Mean signed deviation (MSD) and mean unsigned deviation (MUD) from temperature prediction using 2 to 6 thermometers model for temperatures from 12 to 350 K.

Thermometers	6	5	4	3	2
MSD	-0.0008	-0.0016	0.0048	0.0154	0.0201
MSD (%)	-0.0847	-0.1592	0.4811	1.5414	2.0106
MUD	0.0284	0.0430	0.0368	0.0806	0.1623
MUD (%)	2.8484	4.3000	3.6812	8.0550	16.2302

The table presents statistical measures, Mean Signed Deviation (MSD) and Mean Unsigned Deviation (MUD), along with their percentage counterparts, with respect to the average multiparametric thermometers, for temperatures ranging from 12 to 350 K. These measures provide insights into the accuracy and precision of the temperature predictions obtained using different numbers of thermometers.

1. **MSD (Mean Signed Deviation):**

    - MSD represents the average difference between the predicted temperature and the actual temperature, considering the sign (positive or negative).
    - For 6 thermometers, the MSD is -0.0008, which indicates a very slight negative bias (underestimation) in the predictions.
    - As the number of thermometers decreases, the MSD increases, suggesting a gradual overestimation of the temperature as fewer thermometers are used.

2. **MSD (%):**

    - MSD as a percentage reflects the relative deviation as a proportion of the actual temperature.
    - The percentage values for MSD are small and negative for 6 and 5 thermometers, indicating a slight underestimation.
    - However, as the number of thermometers decreases, the MSD percentage increases, implying a larger relative underestimation.

3. **MUD (Mean Unsigned Deviation):**

    - MUD represents the average absolute difference between the predicted temperature and the actual temperature. It measures the magnitude of the prediction errors without considering their direction (overestimation or underestimation).
    - MUD values are generally higher than MSD values because they do not account for the direction of the errors.
    - MUD increases as the number of thermometers decreases, indicating that the prediction errors become larger in magnitude when fewer thermometers are used.

4. **MUD (%):**

    - MUD as a percentage reflects the relative magnitude of the absolute deviation as a proportion of the actual temperature.

- Similar to MUD, the MUD percentage increases as the number of thermometers decreases, showing that the relative magnitude of the prediction errors becomes more substantial with fewer thermometers.

Overall, the statistical analysis of this table suggests that using more thermometers leads to more accurate and precise temperature predictions. With 6 thermometers, the errors are small, and the predictions closely match the actual temperatures. As the number of thermometers decreases, the errors, both in terms of magnitude and direction, tend to increase. This demonstrates the importance of using a greater number of thermometers in the multiparametric linear regression to achieve more reliable temperature predictions.

4. CONCLUSIONS OF EXCITATION THERMOMETRY.

Nanothermometry has become relevant in academia and industries, which has attracted intense research. Due to their photophysical properties, materials containing lanthanide ions are widely studied and employed for the development of nanothermometers, particularly those with a well-stablished thermometric equation (known calibration, or primary thermometers) that relates the temperature to a thermometric parameter, self-calibration, high relative sensitivity, high spatial and temporal resolutions. For the first time, it was proposed, tested, and validated the application of excitation spectra to obtain thermometric parameters with those properties. In fact, it was shown that ratios between intensities of bands in the excitation spectra provide thermometric parameters, Δ_i, as $A_i e^{-\Delta E_i/(k_B T)}$, where ΔE_i is the energy difference between thermally coupled states, e.g., $^7F_{0,1,2}$ of Eu(III), k_B is the Boltzmann constant, T is the temperature, and A_i is a constant (independent of the temperature) involving the properties of the states. Thus, its relative sensitivity S_r becomes $S_{r,i} = \Delta E_i/(k_B T^2)$. It is noteworthy that some transitions have ratios that are independent of the temperature, thus yielding self-calibrated thermometers. In addition, two or more selected transitions provide ratios that must give the same temperature, which can quantify and improve the accuracy of a measured temperature. When the selected transitions in the excitation spectra can be associated to the emission ones, then the pre-exponential factor A_i can be determined from the emission spectrum and, therefore, the thermometers have known calibrations (primary-S thermometers).

These features were demonstrated for molecular complexes and doped nanoparticles for a wide range of temperature. The predicted temperatures were in good agreement with the observed (or reference) temperature. However, especially for $^7F_0 \rightarrow {}^5D_0$ and $^7F_1 \rightarrow {}^5D_0$ transitions, the prediction of temperature requires a better treatment, due to the lack of spectral

correction for these transitions when monitored at ca. 615 nm. Other lanthanide ions, other than Eu(III), such as Tb(III) and Sm(III), may also be interesting for this new methodology, expanding the scope of applications for these thermometers. Our findings are also relevant because the thermometers are self-calibrated (e.g., primary-S from spectral data or primary-T from a known temperature), self-referenced (temperature independent), and the temperature can be determined from excitation spectroscopy, which does not employ powerful sources and do not interfere with the measurement. Thus, intra-4*f* transitions in lanthanide ions, especially Eu(III), are ideal for these determinations because ΔE_i, as well as the pre-exponential factor, are highly insensitive to the ion environment so its calibrations should be remaining valid for any situation if the compound or material containing the lanthanide ions does not degrade. It is noteworthy that this is a quite simple approach and experimental setup for the measurements, which makes it very general. The peculiar photophysical properties of the lanthanide ions makes these thermometers quite robust, accurate and fully predictable in the sense that practically any materials (nanocrystals, nanoparticles, complexes, MOFs etc.) can be employed as long as the excitation bands due to the ligands do not overlap with those related to the infra-4*f* transitions. In addition, the sensitivity and accuracy can be tuned by choosing the excitations or a lanthanide ion with an appropriate energy of the first excited state with respect to the ground state.

Regarding the multiparametric linear regression (MLR), this study highlights the efficacy of MLR as a powerful statistical tool for modelling complex relationships between multiple independent variables and a predicted variable. It has broad applications in data analysis and predictive modelling across diverse fields.

The research centered on predicting temperature and relative thermal sensitivity based on statistical analyses using the Y_2O_3:Eu^{3+} nanoparticles as the selected thermometric system. This involved analysing excitation spectra and identifying specific Eu(III) transitions,

ultimately leading to the derivation of thermometric parameters. The combination of up to six thermometers was employed in MLR to make predictions, with the selection process remaining random, while a method for optimizing this choice is being developed.

One significant finding was that these thermometric parameters demonstrated temperature-independent behavior, mirroring the characteristics of the europium complex described earlier. The results showed that as the number of thermometers increased, the accuracy and precision of temperature predictions improved significantly. This improvement was most notable in the case of relative thermal sensitivity, where the performance gain ranged from 10 to 1000-fold compared to single thermometer predictions for both temperature and relative thermal sensitivity.

The statistical analysis emphasized the importance of using multiple thermometers. As the number of thermometers decreased, both the mean signed deviation (MSD) and the mean unsigned deviation (MUD) increased, signifying larger prediction errors, both in magnitude and direction. These findings underscored the critical role of employing a greater number of thermometers in the multiparametric linear regression, leading to more reliable and precise temperature predictions, even across a wide temperature range.

In summary, this study showcases the potential of multiparametric linear regression in advancing our understanding and predictive capabilities within the field of thermometry, offering a valuable tool for enhancing temperature predictions and relative thermal sensitivity assessments. The findings emphasize the importance of employing a sufficient number of thermometers to achieve the most accurate and reliable results, which can have significant implications in various scientific and practical applications.

4.1. INTRACELLULAR TEMPERATURE MEASUREMENTS USING PRIMARY-T THERMOMETERS.

The Gd_2O_3 UCNPs doped with 2% molar of Yb(III) ions and 1% molar of Er(III) was synthesized by the co-precipitation method. Spherical Gd_2O_3:Yb(III)/Er(III) nanoparticles were characterized using transmission electron microscopy, X-ray diffraction, zeta potential and dynamic light scattering. Figure 20a,b shows TEM micrographs of the $(Gd_{0.97}Yb_{0.02}Er_{0.01})_2O_3$ nanoparticles after calcination, which display an uniform spherical morphology with a particle size of 60 ± 4 nm and a typical rougher surface. The nanoparticles presented a diffraction pattern compatible with that of the undoped Gd_2O_3 cubic phase reference (Figure 20c). Moreover, in Figure 20b the distance between adjacent lattice fringes, 0.312 ± 0.002 nm, matches the respective d_{222} value (0.31 nm) of the cubic Gd_2O_3 structure (JCPDS No. 04-003-4699). The uncertainty of the lattice fringes was obtained using the standard deviation from the lattice fringes distance distribution.

The $(Gd_{0.97}Yb_{0.02}Er_{0.01})_2O_3$ nanoparticles are moderately dispersible in water presenting a zeta-potential of 10 ± 4 mV and a hydrodynamic size distribution centered at 156 ± 52 nm (Figure 22). When nanoparticles are incorporated into cell culture media, their colloidal and chemical properties are altered due to the presence of proteins and the high ionic content. For instance, serum proteins at a typical concentration of 10% can improve the colloidal stability due to extra electrostatic repulsion provided by proteins adsorbed on the particle surface [78]. Therefore, we expect that serum proteins present in the culture medium may have increased the stability of $(Gd_{0.97}Yb_{0.02}Er_{0.01})_2O_3$ nanoparticles relatively to the water suspension, resulting in the formation of smaller aggregates.

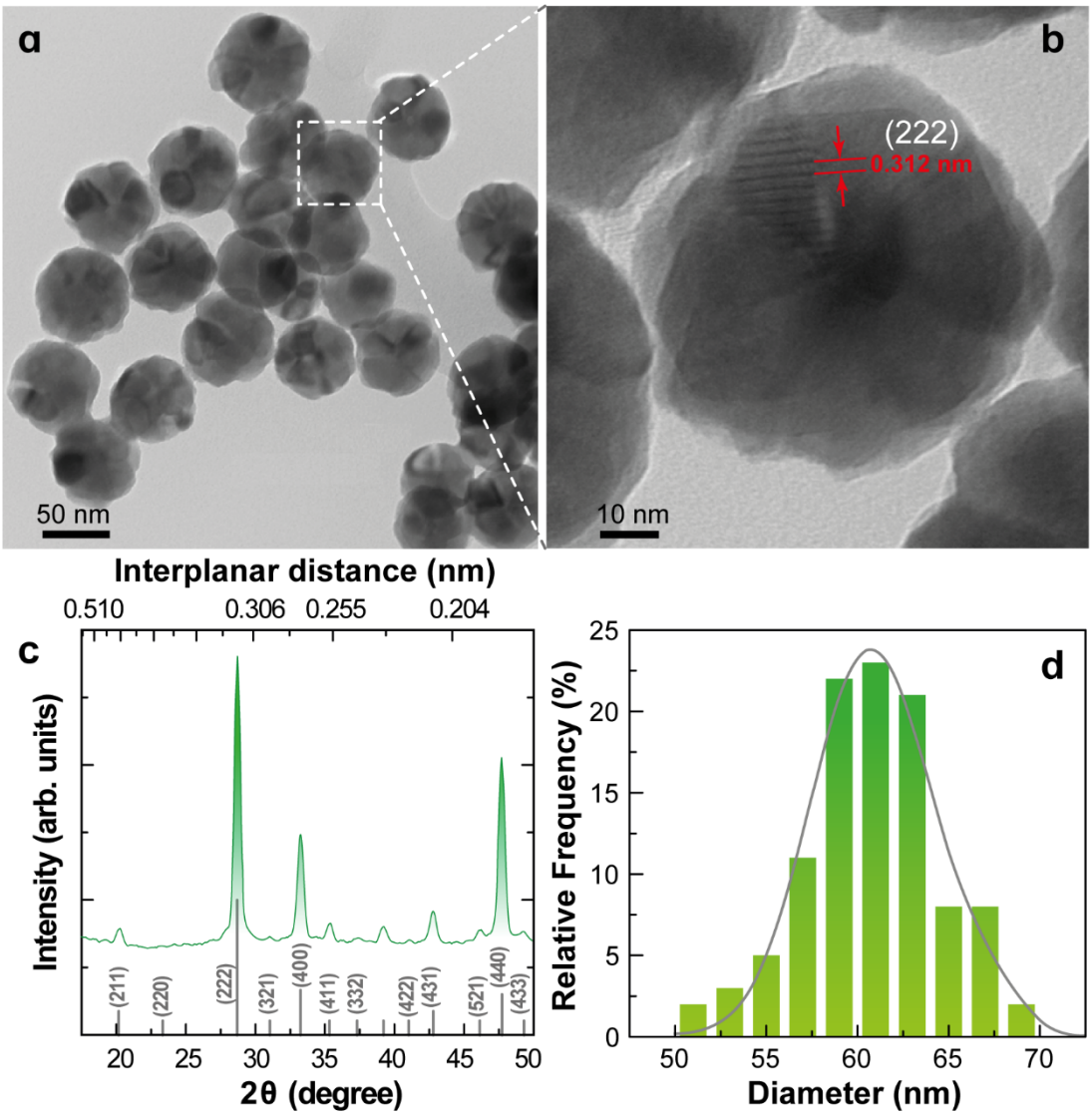

Figure 20. Representative TEM images of $(Gd_{0.97}Yb_{0.02}Er_{0.01})_2O_3$ at (a) low and (b) high magnification. In (b) the interplanar spacing between adjacent (222) planes of cubic Gd_2O_3 is depicted. (c) Powder XRD patterns of the nanoparticles showing reflections of the reference cubic Gd_2O_3 (PDF-4+ code: 04-003-4699). (d) Size distribution calculated from the TEM images using 100 representative nanoparticles. The solid line is the best fit to the experimental data using a log-normal distribution ($r^2 > 0.95$). Adapted from[79].

The emission spectra of the $(Gd_{0.97}Yb_{0.02}Er_{0.01})_2O_3$ nanoparticles display the usual $^2H_{11/2}\rightarrow{}^4I_{15/2}$ and $^4S_{3/2}\rightarrow{}^4I_{15/2}$ transitions (in the green spectral region, Figure 21a), and the $^4F_{9/2}\rightarrow{}^4I_{15/2}$ line (in the red spectral region, not shown). The dependence of the emission spectra with the laser power density (P_D) shows a relative decrease of the $^4S_{3/2}\rightarrow{}^4I_{15/2}$ transition as P_D

increases, a clear sign of temperature augmentation induced by the 980 nm laser irradiation [35, 80]. This is evident in Figure 21b that displays the P_D dependence of the ratio between the integrated intensities of the $^2H_{11/2} \rightarrow {}^4I_{15/2}$ (I_H) and $^4S_{3/2} \rightarrow {}^4I_{15/2}$ (I_S) transitions, define as the thermometric parameter $\Delta = I_H/I_S$.

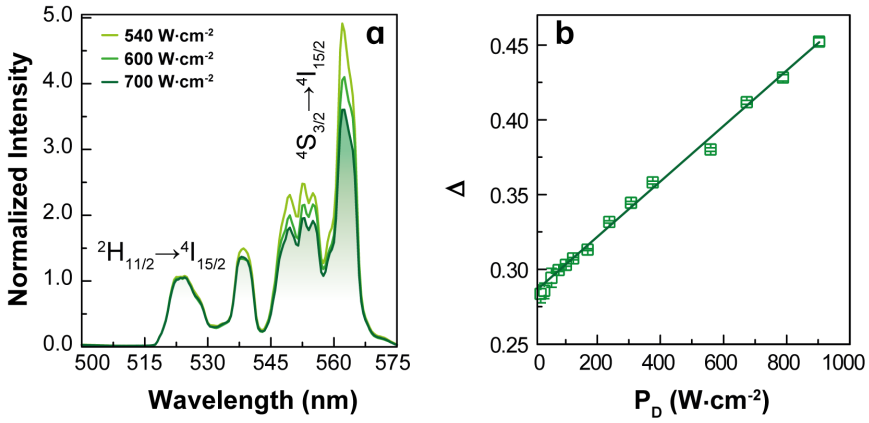

Figure 21. (a) Upconversion partial emission spectra of powdered $(Gd_{0.97}Yb_{0.02}Er_{0.01})_2O_3$ at room temperature upon excitation at 980 nm with different excitation power densities. (b) Dependence of the thermometric parameter with the laser power density. Adapted from[79].

The $(Gd_{0.97}Yb_{0.02}Er_{0.01})_2O_3$ nanoparticles were also characterized by Dynamic light scattering (DLS) and zeta potential.

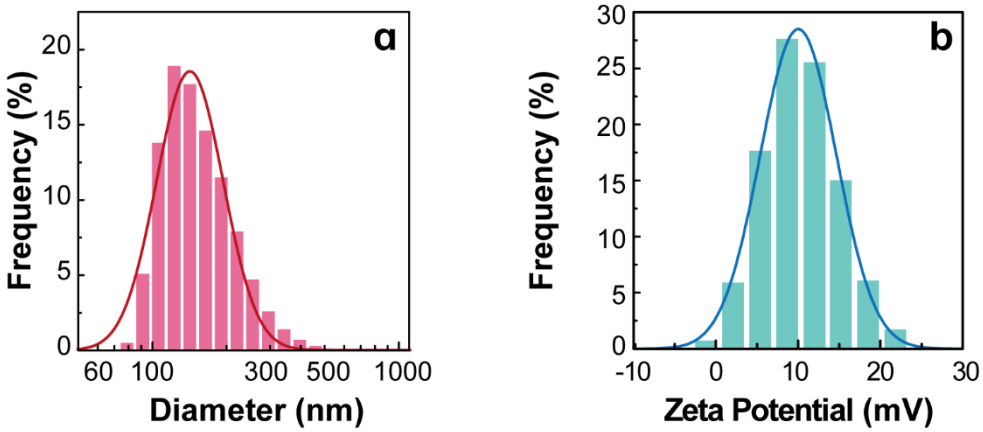

Figure 22. (a) DLS and (b) Zeta potential of an aqueous suspension of the $(Gd_{0.97}Yb_{0.02}Er_{0.01})_2O_3$ nanoparticles (1 mg mL^{-1}). The zeta potential histogram was fitted using a Gaussian function (Equation

3), while the DLS histogram was fitted using a log-normal function (Equation 8). The solid lines are the best fits to the experimental data (Table 5 and Table 6). Source: Author.

Table 5. Fitting parameters of the DLS size histogram presented in Figure 22a.

Parameter	Value	Units
x_c	156 ± 52	nm
w	0.312 ± 0.008	
A	$(2.16 \pm 0.05)\times10^4$	nm
r^2	0.972	

Table 6. Fitting parameters of the Zeta Potential histogram presented in Figure 22b to a Gaussian function.

Parameter	Value	Units
x_c	10.02 ± 4.00	mV
w	9.26 ± 0.05	
A_0	$(3.86 \pm 0.01)\times10^6$	mV
r^2	0.99	

Then, these UCNPs were incorporated into skin cancer cells (MNT-1) by Dr. Helena Oliveira' research group at the Department of Biology at University of Aveiro. Figure 23 shows the *in vitro* cell viability of MNT-1 and A375 melanoma cells treated with $(Gd_{0.97}Yb_{0.02}Er_{0.01})_2O_3$ nanoparticles for 24 and 48 h. The nanoparticles decreased the viability of MNT-1 cells only at the concentration of 200 μg mL^{-1}. For exposure periods of 24 and 48 h the cell viability is similar, 82.4±1.2% and 86.6±11.2%, respectively. Regarding the effects on A375 cells, the nanoparticles did not affect the cell viability at 24 h but induced a decrease in

cell viability for the highest concentrations (87.7% for 100 µg mL^{-1} and 82.5% for 200 µg mL^{-1}) after 48 h. Nevertheless, the viability of both cell lines is above the 70% threshold, and, therefore, according to the norm ISO 10993-5:20099(en) [62], the $(Gd_{0.97}Yb_{0.02}Er_{0.01})_2O_3$ nanoparticles can be considered non-cytotoxic at the range of tested concentrations. These results corroborate our previous study with the exposure of $(Gd_{0.98}Nd_{0.02})_2O_3$ nanoparticles to MNT-1 cells, which did not induce toxicity by 24 h exposure for concentrations up to 400 µg.mL^{-1} [58].

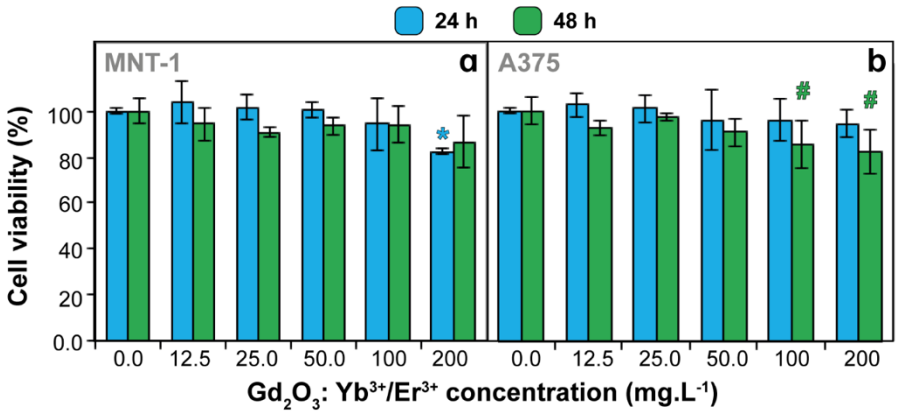

Figure 23. Cell viability of (a) MNT-1 and (b) A375 cell lines exposed to $(Gd_{0.97}Yb_{0.02}Er_{0.01})_2O_3$ nanoparticles for 24 and 48 h. Results are expressed as mean ± SD (standard deviation); the symbols * and # indicate a significant difference ($p<0.05$) between control, respectively at 24 and 48 h exposures. Adapted from[79].

Once the skin cancer cells were fixed, it was possible to obtain optical images. The Figure 24 shows the optical images acquired.

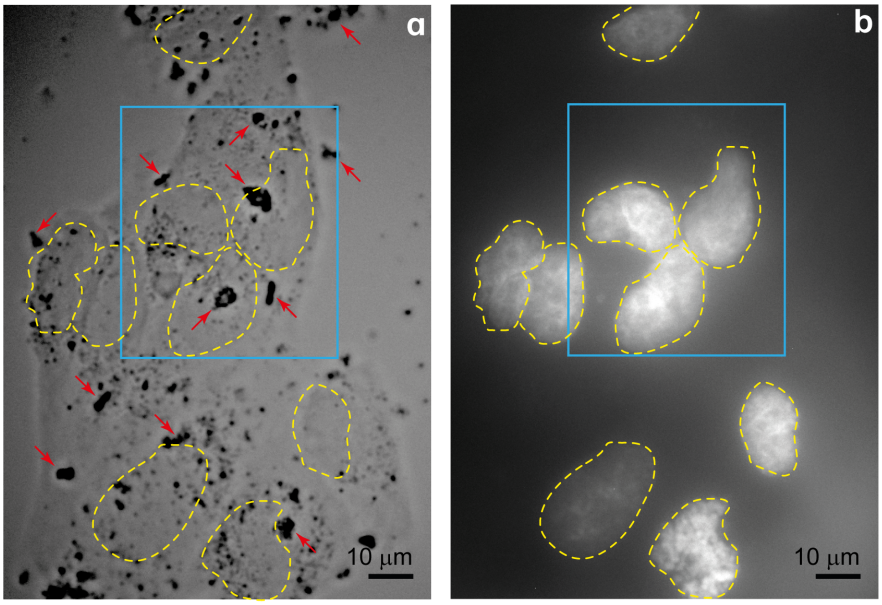

Figure 24. Bright-field optical images of DAPI-marked MNT-1 cells incubated with $(Gd_{0.97}Yb_{0.02}Er_{0.01})_2O_3$ nanoparticles at a fixed configuration acquired with the monochrome camera under (a) white-light illumination (transmission mode) and (b) UV irradiation (365 nm, reflection mode). The dashed lines delimitate the cell nucleus and the arrows mark nanoparticle clusters of different dimensions, visible as dark spots. The blue rectangle indicates the region analyzed in Figure 25. Adapted from[79].

Observing the images, DAPI allows to identify the nucleus of the cells, and unequivocally localize the cells. Using the combination of excitation sources allowed us to observe the UCNPs aggregates as well. Figure 24a displays a bright-field optical image of DAPI-marked MNT-1 cells exposed to $(Gd_{0.97}Yb_{0.02}Er_{0.01})_2O_3$ nanoparticles at a fixed cell preparation. Clusters of nanoparticles of different sizes and degrees of aggregation are visible as dark spots and the nuclei delimitations were detected under UV light illumination by the DAPI staining (fluorescence in the blue spectral range, peaking at 460 nm), Figure 24b, showing overlaid cells due to the density used during the culturing process.

The blue rectangle shown in Figure 24 is magnified in Figure 25a corresponding to the selected area to study the internalization and localization of the Yb(III)/Er(III)-codoped Gd_3O_2 nanoparticles combining 2D optical and hyperspectral images. Under 980 nm irradiation, the optical images of the DAPI-marked MNT-1 cells treated with $(Gd_{0.97}Yb_{0.02}Er_{0.01})_2O_3$

nanoparticles reveal bright spots with distinct intensities displaying red (clusters II and IV) and yellow (clusters I and III) colors, Figure 25b. Because the biological medium has very low absorption at 980 nm, cell autofluorescence is negligible, thus, improving the detection of the upconverting emission. The emission spectra recorded in the hyperspectral image of Figure 25d, (that corresponds to the same region depicted in Figure 25a,b), display the $^2H_{11/2} \rightarrow {}^4I_{15/2}$ and $^4S_{3/2} \rightarrow {}^4I_{15/2}$ transitions, Figure 25c, demonstrating unequivocally that the bright spots correspond to clusters of $(Gd_{0.97}Yb_{0.02}Er_{0.01})_2O_3$ nanoparticles.

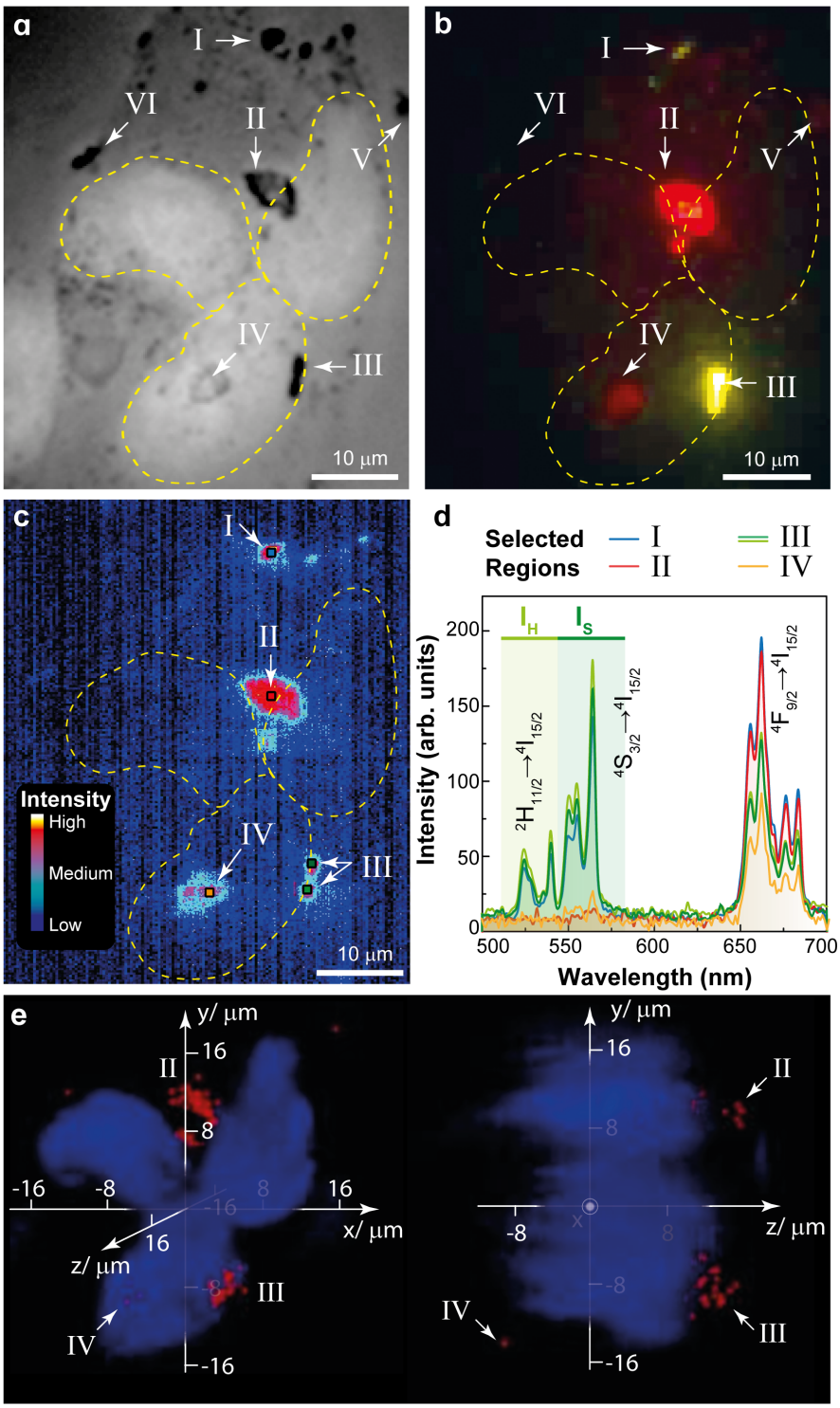

Figure 25. Bright-field 2D optical images of the region delimited by the blue rectangle in Figure 24 recorded at the z = 0 plane under (a) white-light illumination (transmission mode, monochrome camera) and (b) irradiation at 980 nm (reflection mode, color camera). (c) Hyperspectral image of the same region shown in (a) and (b). The color scale is based on the emission intensity at 662 nm (d) Emission spectra recorded in the selected regions (10×10 pixels^2) of the hyperspectral image shown in (c). (e) False-color 3D images showing the localization of the MNT-1 cancer cells nuclei (in blue) and $(Gd_{0.97}Yb_{0.02}Er_{0.01})_2O_3$ clusters in regions II, III, and IV (in red) within the cell culture volume. Adapted from [79].

4.2. ADDITIONAL HYPERSPECTRAL DATA.

The creation of the 3D image with the representation of the location of nanoparticles requires the ability to collect a signature signal [42d]. Here, we used the scattering of the $(Gd_{0.97}Yb_{0.02}Er_{0.01})_2O_3$ nanoparticles as the signature signal because is a well-established method for the detection and location of nanoparticles, especially when using the CytoViva enhanced dark-field illumination system [42d, 81], as it is the case here. Moreover, although the upconversion emission signal can also be used as an alternative signature signal, as, for example, reported in reference[82], the hyperspectral images of Figure 26 show that the pixels where the emission of the nanoparticles is detected correspond exactly to those pixels where the scattering intensity is higher.

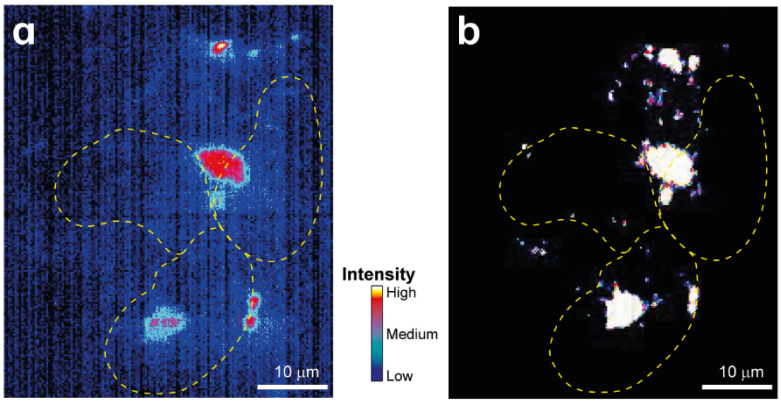

Figure 26. Hyperspectral images in the z = 0 plane recorded under (a) 980 nm irradiation (reflection mode) and (b) with CytoViva enhanced dark-field illumination system. The yellow dash lines delimited the cell's nucleus. The color scales are based on (a) the emission intensity at 662 nm and (b) the scattering intensity of the irradiation band used (peak at ~580 nm). Source: Author.

The emission spectra shown in Figure 25d also pointed out that the distinct colors of the bright spots in Figure 24b are due to distinct intensity ratios between the emissions in the green ($^2H_{11/2}\rightarrow{}^4I_{15/2}/{}^4S_{3/2}\rightarrow{}^4I_{15/2}$) and red ($^4F_{9/2}\rightarrow{}^4I_{15/2}$) spectral regions. The spatial variation of the red-to-green (R/G) intensity ratio has already been reported for confocal [83] and hyperspectral [82] microscopy imaging of single Yb(III)/Er(III)-codoped $LiYF_4$ microparticles. In the first example, the R/G intensity ratio varies twofold depending on if the collected emission arises from the apex, an arris, or a face of the single microcrystals,[83] while in the other work the

variation (also twofold) is linked to the spatial microparticle orientation (difference in the probed emission direction relative to the optic axes of the particles) [82]. Furthermore, the R/G intensity ratio is also dependent on the collection area in the hyperspectral images, as shown in Figure 27 for region IV. This was also reported for β-$NaYF_4$:Yb(III)/Er(III) nanoparticles dispersed in polydimethylsiloxane-based organic-inorganic hybrids[84] and Yb(III)/Er(III)-codoped GeO_2-Ta_2O_5 particles dispersed in poly(methyl methacrylate) [45].

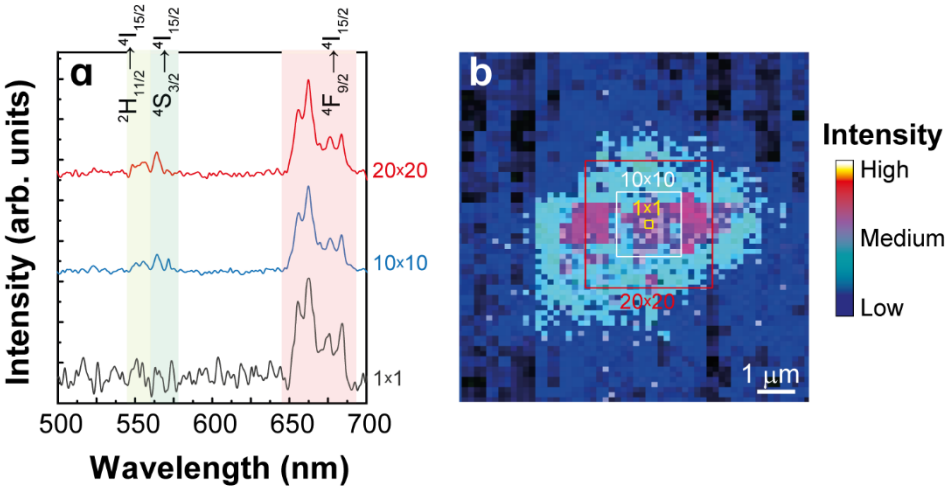

Figure 27. (a) Emission spectra recorded of distinct areas centered at the same pixel of the hyperspectral image of region IV under 980 nm irradiation shown in (b). The color scale is based on the emitted intensity at 662 nm. Source: Author.

Several effects have been suggested to explain the observed R/G intensity ratio variation such as inhomogeneous Yb(III)/Er(III) dopant distribution, different crystal field strengths experienced by doping ions occupying different crystallographic sites within the lattice of the particle, uneven surface-ligand coverage [82], and distinct surface/volume ratios of the particles (or corresponding clusters) [45, 84]. Although for the uniaxially birefringent crystalline $LiYF_4$ host, single-particle polarized emission spectroscopy confirmed that the spatial emission intensity variation exhibited during hyperspectral imaging is due to direction-dependent polarized emission [82], for other examples (as the one reported here) a comprehensive explanation is still needed.

The creation of the 3D image with the representation of the location of nanoparticles requires the ability to collect a signature signal [42d]. Here, we used the scattering of the $(Gd_{0.97}Yb_{0.02}Er_{0.01})_2O_3$ nanoparticles as the signature signal because is a well-established method for the detection and location of nanoparticles, especially when using the CytoViva enhanced dark-field illumination system [42d, 81], as it is the case here. Moreover, although the upconversion emission signal can also be used as an alternative signature signal, as, for example, reported in reference [82], the hyperspectral images of Figure 26 in the Annexes show that the pixels where the emission of the nanoparticles is detected correspond exactly to those pixels where the scattering intensity is higher.

Figure 25e shows a 3D image with the colocalization of the nuclei of the cells and nanoparticles. The image was created by overlaying one 3D image of the cell nuclei and one 3D image representing the localization of the nanoparticles. Each 3D image was obtained by processing sets of optical microscopy images recorded along the spatial *z*-axis. The image of the nuclei of the cells was obtained from the deconvoluted images recorded under UV irradiation. Deconvolution is the process of reversing the optical distortion that takes place in an optical microscope to create clear images [85]. The image with the representation of the position of the nanoparticles was obtained by analyzing the scattering signal observed in the optical images in dark field mode. 3D images show clearly that the $(Gd_{0.97}Yb_{0.02}Er_{0.01})_2O_3$ nanoparticles are distributed in a distinct plane deep in the cell volume in the cytoplasmic and perinuclear regions. This result proves the cell internalization of the nanoparticles. The fact that the clusters of the nanoparticles are in different planes along the *z*-axis (Figure 25e) explains the differences in the brightness of the distinct clusters observed in Figure 25b. It is the case of clusters II and III that are located at a plane closer to the top surface of the cell culture, at $z \approx 9$ μm, their emissions are brighter than that of cluster IV that corresponds to particles located much deeper within the analyzed cell culture volume at $z \approx -8$ μm.

By using the concept of primary thermometers applied to the thermally-coupled $^2H_{11/2}$ and $^4S_{3/2}$ Er(III) electronic levels, introduced in 2017, the temperature (T) can be determined as [17c]:

$$\frac{1}{T} = \frac{1}{T_0} - \frac{k_B}{\Delta E}\ln\left(\frac{\Delta}{\Delta_0}\right) \qquad \text{Equation 34}$$

where Δ_0 is the value Δ at a known temperature T_0 (room temperature), ΔE is the energy separation between the barycenters of the $^2H_{11/2}$ and $^4S_{3/2}$ levels, and k_B is the Boltzmann constant. This innovative concept to predict the temperature does not require a conventional calibration procedure and is used in what follows to determine the temperature of the culture medium imaged in Figure 25. Considering $\Delta_0 = 0.28 \pm 0.01$ (Figure 25), $\Delta E = 762$ cm^{-1},[44] $T_0 = 298 \pm 1$ K (the temperature at the microscope room), and the Δ values determined from the emission spectra recorded by the hyperspectral system in regions I (0.28 ± 0.01) and III (0.28 ± 0.02), Figure 25, the absolute temperature calculated from Equation 2 is 298 ± 1 and 298 ± 2 K, for regions I and II, respectively. Whereas the uncertainty in the Δ values are calculated accordingly to Equation 3, error propagation in Equation 5 yields the temperature uncertainty.

As expected, these values match the registered room temperature because the cells under observation are in a fixed configuration. Moreover, the agreement between the temperature values determined for the two regions confirms this assessment, despite their distinct R/G intensity ratios there are no temperature gradients within the cell culture, as it is expected for fixed cells [7a, 86].

4.3. ADDITIONAL 3D IMAGES.

Once the 2D temperature was obtained, it is important to understand if this temperature is the same in different cell directions. To assess the temperature in those different directions,

locating the nanoparticles throughout the cellular medium is extremely important. The 3D analysis was performed using a custom CytoViva 3D software. The 3D images were created using the procedure mentioned above, in the Characterization section. Figure 28 shows the 3D image created following the previous procedure using the MNT-1 cells treated with Gd_2O_3 (UCNPs) co-doped with Er(III)/Yb(III).

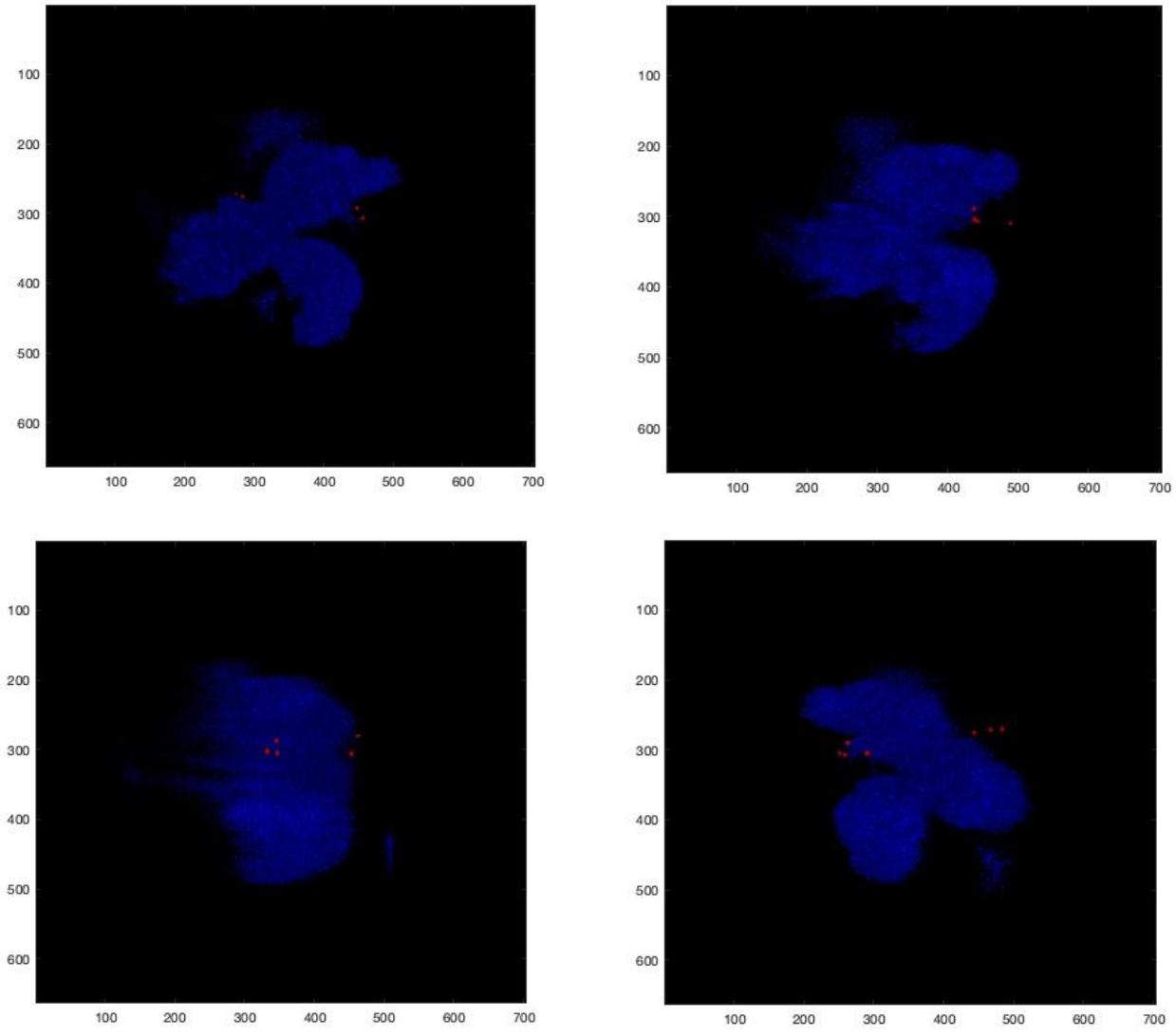

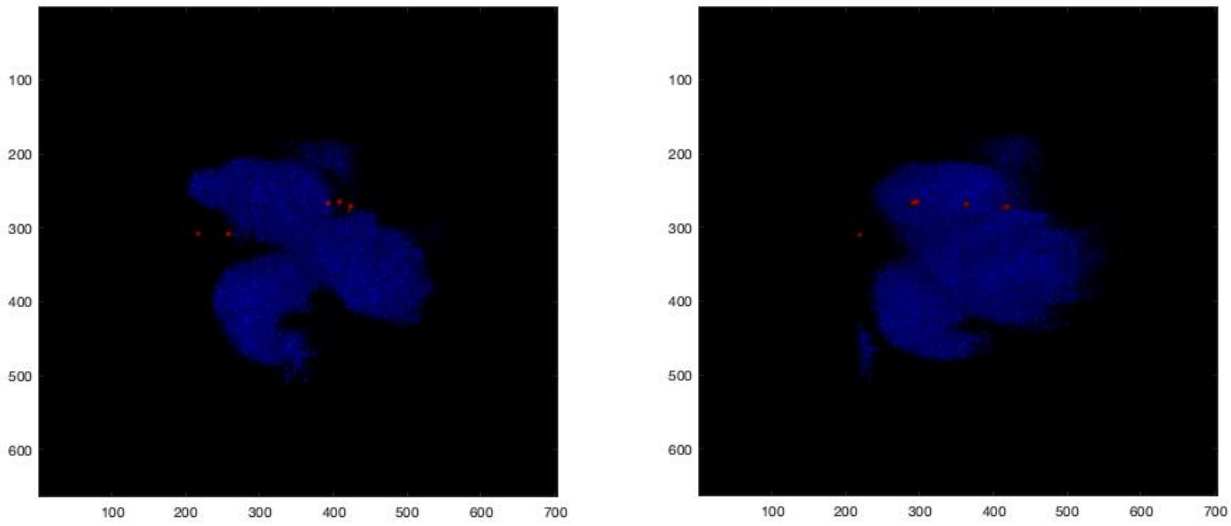

Figure 28. 3D image of MNT-1 cells treated with Gd_2O_3 (UCNPs) co-doped with Er(III)/Yb(III). Source: Author.

Combining the hyperspectral image in 2D and the 3D optical images it is possible to locate the nanoparticles incorporated into the cells. After analyzing the 3D images, it is possible to check that the nanoparticles are located around the nucleus region as well as the perinuclear region. Suggesting that the nanoparticles were incorporated into the MNT-1 cells showing a good agreement with the 2D images (Figure 25)

4.4. CONCLUSION FOR INTRACELLULAR TEMPERATURE MEASUREMENTS USING PRIMARY-T THERMOMETERS.

$(Gd_{0.97}Yb_{0.02}Er_{0.01})_2O_3$ nanoparticles were prepared with uniform spherical morphology, displaying an average size of 60 ± 4 nm, with a typical rougher surface, and moderately dispersibility in water. Their emission spectra under excitation at 980 nm present the usual $^2H_{11/2}\rightarrow{}^4I_{15/2}$, $^4S_{3/2}\rightarrow{}^4I_{15/2}$, and $^4F_{9/2}\rightarrow{}^4I_{15/2}$ Er(III) transitions whose intensity depends

on the laser power density and temperature. In particular, the dependence of the ratio between the integrated intensities of the former two bands on the temperature yields the thermometric parameter $\Delta = I_H/I_S$.

The $(Gd_{0.97}Yb_{0.02}Er_{0.01})_2O_3$ nanoparticles showed no cytotoxicity (at the range of concentrations tested) to the melanoma MNT-1 and A375 cell lines and were successfully internalized by the former cells. The 3D sub-cellular localization of the nanoparticles in MNT-1 cells in a fixed configuration was achieved by processing sets of optical microscopy images obtained along the *z*-direction. The corresponding 2D hyperspectral images are used to unequivocally identify the cell nuclei and the nanoparticles. The results pinpoint the upconverting nanoparticles relatively to the nuclei of the cells distributed in distinct planes deep inside the cell volume in the cytoplasmic and perinuclear regions. As a proof-of-concept experiment, the intracellular temperature was determined using the emission spectra recorded at fixed cells, recovering a temperature value that is compatible with the room temperature. As far as we know, this is the first time that this strategy is applied to luminescent nanoparticles and can be used in real-time providing new avenues in the spatial-temporal characterization and detection of bio-analytes.

5. GENERAL PERSPECTIVES.

Hyperspectral images can be a useful tool in terms of detection and characterization of bio-analytes. In this work we highlighted the successful internalization of Ln(III)-based nanoparticles, so a future step would be to extend the domain of action in terms of different materials incorporated into the cells such as bio-compatible complexes, micelles, or other organic-inorganic hybrids. Considering the specific outcome from this work, new

hyperspectral images using different objective magnifications to improve the signal-to-noise ratio, employed the UC spectra to obtain a hyperspectral image spectral library, to develop a hyperspectral image protocol for temperature determination as well as to improve the 3D image acquisition protocol that combined with the hyperspectral image protocol will be used to develop a 3D temperature mapping.

Regarding the excitation thermometry, the novel approach introduced in this work encouraged us to apply primary thermometers to new materials, such as non-β-diketone complex, e.g., $[Eu(bpyO_2)(Cl)_2(H_2O)_4](Cl)\cdot H_2O$, and other lanthanide-doped nanoparticles like BiF:Eu(III) in different media (solid state and solutions/dispersions); as well as using a multiparametric approach to estimate the temperature and the relative thermal sensitivity.

6. ANNEXES.

6.1. EXCITATION THERMOMETRY – THEORY.

6.1.1. Historical background.

Other thermometers are based on the temperature dependence of the emission energy peak of semiconductors (nanoparticles), which is related to the temperature by the phenomenological equation [16] that depends on three parameters. One of these parameters is determined at cryogenic temperatures (~13 K), whereas the remaining two parameters are fitted to known temperatures within the range of interest [16]. On the other hand, thermometric parameters based on ratios of (integrated) emission intensities of levels in thermal equilibrium satisfy the $\Delta = B\exp[-\Delta E/(kT)]$, where B and ΔE are constants [11a, 15, 17a-e], with ΔE being the energy difference between the levels in thermal equilibrium, and k is the Boltzmann constant. On the other hand, the pre-exponential factor A depends on several properties of system (*e.g.*, refraction index), particularly of these levels (*e.g.*, degeneracies, branching ratios, transition rates, frequencies, etc.). Thus, *ab initio* theories to calculate this constant B are not accurate enough to provide adequate estimates for quantitative thermometry [17b, 17c, 74, 87].

It is interesting to revisit the pioneer primary-S thermometer employed the integrated intensities of the $^5D_0 \rightarrow {}^7F_4$ transition in Y_2O_3:Eu(III) nanocrystals upon excitations at 611 and 580 nm or at 593 and 580 nm [17b]. The ratios provided two thermometric parameters: Δ' suitable for cryogenic temperatures, in the 190−280 K range and Δ for the physiological range , 290−320 K. A comparison of calculated Δ and Δ' with temperature was provided with relative uncertainties of 3% and 2%, respectively [17b]. However, the authors have not compared the predicted temperature with that registered by the thermocouple nor provided the values of

thermometric parameters at the measured temperatures. Thus, the accuracy and precision of these thermometers could not be assessed.

6.1.2. Pros and cons of measuring temperature with the excitation spectra.

Although more elaborated equipment and longer acquisition times can be a disadvantage of thermometers based on the excitation spectrum, some strategies can be employed, however, to minimize this drawback, such as using few excitation bands recorded in a narrower spectral range or even using the excitation intensities at selected wavelengths instead of scanning a given spectral range. These wavelengths should be selected from the maximum of bands with similar widths. Alternatively, arrays of light-emitting diodes can provide tunable excitation sources [88], thus avoiding monochromator and complex optical systems, which combined with CCD detector would allow for fast measurements and possible miniaturization. Complex samples, especially for biological applications, could be a real concern but the excitation-based thermometers proposed here are quite flexible because at least 8 viable bands can be employed yielding ca. 20 primary-T thermometers, which increases the chances of avoiding or eliminating interferences from the medium. Detection is also flexible because for Eu(III) it can be performed at the edge of the first biological window ca. 700 nm as demonstrated in the present text, as well as at ca. 515 nm and, if the equipment allows, at ca. 815 nm ($^5D_0 \longrightarrow {}^7F_6$), which could minimize or even eliminate interferences from the medium.

The primary-T and primary-S thermometers here proposed are firmly grounded on reliable photophysical principles and are truly non-invasive (in the detection). Moreover, they are quite

sensitive, very simple to use, and do not require elaborated data treatment or sophisticated instrumentations, which open many perspectives of improvements and applications.

6.1.3. General remarks.

It is relevant to emphasize that the thermometric equations governing these referenced primary-T and primary-S thermometers were derived from first principles using the emission intensity and rate equations. Because the excitation spectrum is monitored at a selected emission transition, the thermometric parameter defined in Equation 1 can be expressed as the ratio of the emitting level upon different excitations, Equation 2. A consistent and comprehensive set of energy levels describing 4*f*-4*f* transitions in lanthanide ions was constructed Figure 7 and a corresponding set of rate equations was derived. Employing the steady state condition, which requires a continuous and low power density excitation source, the population of the emitting level was determined in terms of the populations and transitions rates between the remaining levels. Under the condition of low excitation power density, the populations of high-lying excited levels are vanishing small and can be neglected compared to the populations of the low-lying thermally coupled levels. As a result, the thermometric parameter becomes the ratio of two thermally coupled levels and the thermometric equation, Equation 1, is derived. The surrounding effects on the transitions of lanthanide ions were considered through its index of refraction within the local field model. This leads to a known dielectric factor for transitions with different mechanisms. In addition, by employing the usual procedure to derive the Einstein coefficients of an absorption $\alpha \rightarrow \beta$ and the corresponding $\beta \rightarrow \alpha$ emission, it is possible to express the pre-exponential factor as ratio of integrated intensities in the emission spectrum,

Equation 20. A detailed derivation is presented in what follows providing a consistent physical basis for the thermometric equations, which is relevant for developing primary thermometers with known applications and limitations.

6.1.4. Thermometric parameters based on excitation spectroscopy: energy levels.

Consider an excitation spectrum monitored at a given emission wavelength, which has several bands associated to transitions from a manifold of low-lying states ($\alpha = a, b, c, ...$) to a set of high-lying excited states ($\beta = e, f, g, ...$), depicted in Figure 7.

The emitting level used in the monitoring of the excitation spectrum is the lowest energy level e of the excited state set. Some of these low-lying levels, e.g., a, b, c, are thermally coupled, hence the representation of the non-radiative transitions to and from these levels. The thermally coupled levels will be employed in developing thermometric parameters based on excitation spectrum.

6.1.5. Self-referencing and primary-T thermometers (excitation spectrum).

The excitation intensities $I_{\alpha\beta}$ are monitored at the same wavelength (e.g., *ca*. 615 nm for $^5D_0 \longrightarrow {}^7F_2$ or *ca*. 700 nm for $^5D_0 \longrightarrow {}^7F_4$) for all transitions in the excitation spectrum of $Eu(hfa)_3bpyO_2$. These excitation intensities $I_{\alpha\beta}$ are proportional to the number of the emitters in level e, $N_e(\alpha \rightarrow \beta)$, which depends on the transition from the low-lying thermally coupled states ($\alpha = a, b,$ or c) to the high-lying state ($\beta = e, f, g, ...$), namely [67, 89]

$$I_{\alpha\beta} \propto h\nu_e A_e N_e(\alpha \rightarrow \beta), \qquad \alpha = a, b, c, \qquad \beta = e, f, g, \ldots \qquad \textbf{Equation A35}$$

when the emitted intensity is measured as energy per unit of time (power), or

$$I_{\alpha\beta} \propto A_e N_e(\alpha \rightarrow \beta), \qquad \alpha = a, b, c, \qquad \beta = e, f, g, \ldots \qquad \textbf{Equation A36}$$

when it is measured as the number of photons per unit of time (photon counts per second), where $h\nu_e$ and A_e is the energy of the monitored emission and the radiative emission rate from level e, respectively, and $N_e(\alpha \rightarrow \beta)$ is the number of the emitters in level e, when the excitation occurs from a low-lying state α to a high-lying state β. Because the emitted radiation is monitored at the same wavelength for all transitions in the excitation spectrum, the initial and final levels are the same, so the radiative rate A_e as well as the energy of the monitored emission $h\nu_e$ are independent of the excitation wavelength.

Taking the thermometric parameter, Δ_i, as the ratio of the integrated intensity $I_{\alpha\beta}$ to that of $I_{\alpha'\beta'}$ in the excitation spectrum and applying **Equation A35** or **Equation A36** yields,

$$\Delta_i \equiv \Delta^{\alpha\beta}_{\alpha'\beta'} = \frac{I_{\alpha\beta}}{I_{\alpha'\beta'}} = \frac{S^{\mathrm{ex}}_{\alpha\rightarrow\beta}}{S^{\mathrm{ex}}_{\alpha'\rightarrow\beta'}} = \frac{h\nu_e A_e N_e(\alpha \rightarrow \beta)}{h\nu_e A_e N_e(\alpha' \rightarrow \beta')} = \frac{N_e(\alpha \rightarrow \beta)}{N_e(\alpha' \rightarrow \beta')} \qquad \textbf{Equation A37}$$

where the proportionality constant in Eq. (S28) is the same for both transitions $\alpha \rightarrow \beta$ and $\alpha' \rightarrow \beta'$, because the intensities $I_{\alpha\beta}$ and $I_{\alpha'\beta'}$ are monitored at the same wavelength using the same experimental parameters. In **Equation A37**, $S^{\mathrm{ex}}_{\alpha\rightarrow\beta}$ and $S^{\mathrm{ex}}_{\alpha'\rightarrow\beta'}$ are the areas of the bands associated with transitions $\alpha \rightarrow \beta$ and $\alpha' \rightarrow \beta'$, respectively, in the excitation spectrum.

The number of ions or the population at each level is governed by a set of rate equations, which relates the rate of change of the number of ions at each level with the net pathways that populate and depopulate each level.

For the energy diagram and transitions depicted in Figure 7. Simplified energy level scheme used to describe the excitation spectrum from a manifold of low-lying, denoted collectively as α, where α = a, b, c, ... (in increasing order of energy), to a set of high-lying excited states, denoted

collectively as β, where $\beta = e, f, g, \ldots$ (in increasing order of energy). The low-lying levels a, b, and c are thermally coupled. Dashed arrows represent nonradiative transitions and solid arrows correspond to radiative transitions., the rate equations for an excitation from level b in the thermally couple manifold to a level i in the set of high-lying excited state, namely $b \rightarrow i$, are:

$$\frac{\mathrm{d}N_a}{\mathrm{d}t} = (k_{ea}N_e + k_{fa}N_f + k_{ga}N_g + \cdots + k_{ia}N_i + k_{ja}N_j) + k_{ba}N_b - k_{ab}N_a$$

$$\frac{\mathrm{d}N_b}{\mathrm{d}t} = (k_{eb}N_e + k_{fb}N_f + k_{gb}N_g + \cdots + k_{ib}N_i + k_{jb}N_j) + k_{ab}N_a + k_{cb}N_c - k_{ba}N_b - k_{bc}N_b - k_{bi}N_b$$

$$\frac{\mathrm{d}N_c}{\mathrm{d}t} = (k_{ec}N_e + k_{fc}N_f + k_{gc}N_g + \cdots + k_{ic}N_i + k_{jc}N_j) + k_{dc}N_d + k_{bc}N_b - k_{cb}N_c$$

$$\frac{\mathrm{d}N_d}{\mathrm{d}t} = (k_{ed}N_e + k_{fd}N_f + k_{gd}N_g + \cdots + k_{id}N_i + k_{jd}N_j) - k_{dc}N_d$$

for the number of ions in the low-lying levels of the manifold α. Summation of these equations describing the manifold α gives

$$\frac{\mathrm{d}(N_a + N_b + N_c + \cdots + N_d)}{\mathrm{d}t} \equiv \frac{\mathrm{d}N_\alpha}{\mathrm{d}t}$$

$$= (k_{ea}N_e + k_{fa}N_f + k_{ga}N_g + \cdots + k_{ia}N_i + k_{ja}N_j) + k_{ba}N_b - k_{ab}N_a$$

$$+ (k_{eb}N_e + k_{fb}N_f + k_{gb}N_g + \cdots + k_{ib}N_i + k_{jb}N_j) + k_{ab}N_a + k_{cb}N_c$$

$$- k_{ba}N_b - k_{bc}N_b - k_{bi}N_b + (k_{ec}N_e + k_{fc}N_f + k_{gc}N_g + \cdots + k_{ic}N_i + k_{jc}N_j)$$

$$+ k_{dc}N_d + k_{bc}N_b - k_{cb}N_c + (k_{ed}N_e + k_{fd}N_f + k_{gd}N_g + \cdots + k_{id}N_i$$

$$+ k_{jd}N_j) - k_{dc}N_d$$

$$= (k_{ea} + k_{eb} + k_{ec} + \cdots + k_{ed})N_e + (k_{fa} + k_{fb} + k_{fc} + \cdots + k_{fd})N_f + (k_{ga}$$

$$+ k_{gb} + k_{gc} + \cdots + k_{gd})N_g + \cdots + (k_{ia} + k_{ib} + k_{ic} + \cdots + k_{id})N_i + (k_{ja}$$

$$+ k_{jb} + k_{jc} + \cdots + k_{jd})N_j - k_{bi}N_b$$

$$= \sum_{\alpha''}^{a,b,c,\ldots} k_{e\alpha''}N_e + \sum_{\alpha''}^{a,b,c,\ldots} k_{f\alpha''}N_f + \sum_{\alpha''}^{a,b,c,\ldots} k_{g\alpha''}N_g + \cdots + \sum_{\alpha''}^{a,b,c,\ldots} k_{i\alpha''}N_i$$

$$+ \sum_{\alpha''}^{a,b,c,\ldots} k_{j\alpha''}N_j - k_{bi}N_b$$

or,

$$\frac{\mathrm{d}N_\alpha}{\mathrm{d}t} = \sum_{\beta''}^{e,f,g,\ldots} \sum_{\alpha''}^{a,b,c,\ldots} \left(k_{\beta''\alpha''}N_{\beta''}\right) - k_{bi}N_b$$

where

$$N_\alpha = N_a + N_b + N_c + \cdots + N_d = \sum_{\alpha''}^{a,b,c,\ldots} N_{\alpha''}$$

For the levels in the set of high-lying excited states β, the rate equations are

$$\frac{\mathrm{d}N_e}{\mathrm{d}t} = k_{fe}N_f - (k_{ea} + k_{eb} + k_{ec} + \cdots + k_{ed})N_e = k_{fe}N_f - \sum_{\alpha''}^{a,b,c,\ldots} k_{e\alpha''}N_e$$

$$\frac{\mathrm{d}N_f}{\mathrm{d}t} = k_{gf}N_g - (k_{fa} + k_{fb} + k_{fc} + \cdots + k_{fd})N_f - k_{fe}N_f$$

$$= k_{gf}N_g - \sum_{\alpha''}^{a,b,c,\ldots} k_{f\alpha''}\,N_f - k_{fe}N_f$$

$$\frac{\mathrm{d}N_g}{\mathrm{d}t} = k_{ig}N_i - (k_{ga} + k_{gb} + k_{gc} + \cdots + k_{gd})N_g - k_{gf}N_g$$

$$= k_{ig}N_i - \sum_{\alpha''}^{a,b,c,\ldots} k_{g\alpha''}\,N_g - k_{gf}N_g$$

$$\frac{\mathrm{d}N_i}{\mathrm{d}t} = k_{bi}N_b + k_{ji}N_j - (k_{ia} + k_{ib} + k_{ic} + \cdots + k_{id})N_i - k_{ig}N_i$$

$$= k_{bi}N_b + k_{ji}N_j - \sum_{\alpha''}^{a,b,c,\ldots} k_{i\alpha''}\,N_i - k_{ig}N_i$$

$$\frac{\mathrm{d}N_j}{\mathrm{d}t} = -(k_{ia} + k_{ib} + k_{ic} + \cdots + k_{id})N_j - k_{ji}N_j = -\sum_{\alpha''}^{a,b,c,\ldots} k_{j\alpha''}\,N_j - k_{ji}N_j$$

Summation of these rate equations describing levels in the set of high-lying excited states β yields

$$\frac{\mathrm{d}(N_e + N_f + N_g + \cdots + N_i + N_j)}{\mathrm{d}t} \equiv \frac{\mathrm{d}N_\beta}{\mathrm{d}t}$$

$$= k_{bi}N_b$$

$$-\left(\sum_{\alpha''}^{a,b,c,\ldots} k_{e\alpha''}\,N_e + \sum_{\alpha''}^{a,b,c,\ldots} k_{f\alpha''}\,N_f + \sum_{\alpha''}^{a,b,c,\ldots} k_{g\alpha''}\,N_g + \cdots + \sum_{\alpha''}^{a,b,c,\ldots} k_{i\alpha''}\,N_i\right.$$

$$\left. + \sum_{\alpha''}^{a,b,c,\ldots} k_{j\alpha''}\,N_j\right)$$

or,

$$\frac{\mathrm{d}N_\beta}{\mathrm{d}t} = k_{bi}N_b - \sum_{\beta''}^{e,f,g,\ldots} \sum_{\alpha''}^{a,b,c,\ldots} k_{\beta''\alpha''}N_{\beta''} = -\frac{\mathrm{d}N_\alpha}{\mathrm{d}t}$$

where

$$N_\beta = N_e + N_f + N_g + \cdots + N_i + N_j = \sum_{\beta''}^{e,f,g,\ldots} N_{\beta''}$$

Similarly, for $a \rightarrow j$ excitation:

$$\frac{\mathrm{d}N_a}{\mathrm{d}t} = (k_{ea}N_e + k_{fa}N_f + k_{ga}N_g + \cdots + k_{ia}N_i + k_{ja}N_j) + k_{ba}N_b - k_{ab}N_a - k_{aj}N_a$$

$$\frac{\mathrm{d}N_b}{\mathrm{d}t} = (k_{eb}N_e + k_{fb}N_f + k_{gb}N_g + \cdots + k_{ib}N_i + k_{jb}N_j) + k_{ab}N_a + k_{cb}N_c - k_{ba}N_b - k_{bc}N_b$$

$$\frac{\mathrm{d}N_c}{\mathrm{d}t} = (k_{ec}N_e + k_{fc}N_f + k_{gc}N_g + \cdots + k_{ic}N_i + k_{jc}N_j) + k_{dc}N_d + k_{bc}N_b - k_{cb}N_c$$

$$\frac{\mathrm{d}N_d}{\mathrm{d}t} = (k_{ed}N_e + k_{fd}N_f + k_{gd}N_g + \cdots + k_{id}N_i + k_{jd}N_j) - k_{dc}N_d$$

whose summation gives,

$$\frac{\mathrm{d}(N_a + N_b + N_c + \cdots + N_d)}{\mathrm{d}t} \equiv \frac{\mathrm{d}N_\alpha}{\mathrm{d}t}$$

$$= (k_{ea} + k_{eb} + k_{ec} + \cdots + k_{ed})N_e + (k_{fa} + k_{fb} + k_{fc} + \cdots + k_{fd})N_f + (k_{ga} + k_{gb} + k_{gc} + \cdots + k_{gd})N_g + \cdots + (k_{ia} + k_{ib} + k_{ic} + \cdots + k_{id})N_i + (k_{ja} + k_{jb} + k_{jc} + \cdots + k_{jd})N_j - k_{aj}N_a$$

$$= \sum_{\alpha''}^{a,b,c,\ldots} k_{e\alpha''}N_e + \sum_{\alpha''}^{a,b,c,\ldots} k_{f\alpha''}N_f + \sum_{\alpha''}^{a,b,c,\ldots} k_{g\alpha''}N_g + \cdots + \sum_{\alpha''}^{a,b,c,\ldots} k_{i\alpha''}N_i + \sum_{\alpha''}^{a,b,c,\ldots} k_{j\alpha''}N_j - k_{aj}N_a$$

or,

$$\frac{\mathrm{d}N_\alpha}{\mathrm{d}t} = \sum_{\beta''}^{e,f,g,\ldots} \sum_{\alpha''}^{a,b,c,\ldots} \left(k_{\beta''\alpha''} N_{\beta''}\right) - k_{aj} N_a$$

And, for the set β:

$$\frac{\mathrm{d}N_e}{\mathrm{d}t} = k_{fe} N_f - (k_{ea} + k_{eb} + k_{ec} + \cdots + k_{ed}) N_e = k_{fe} N_f - \sum_{\alpha''}^{a,b,c,\ldots} k_{e\alpha''} N_e$$

$$\frac{\mathrm{d}N_f}{\mathrm{d}t} = k_{gf} N_g - (k_{fa} + k_{fb} + k_{fc} + \cdots + k_{fd}) N_f - k_{fe} N_f$$

$$= k_{gf} N_g - \sum_{\alpha''}^{a,b,c,\ldots} k_{f\alpha''} N_f - k_{fe} N_f$$

$$\frac{\mathrm{d}N_g}{\mathrm{d}t} = k_{ig} N_i - (k_{ga} + k_{gb} + k_{gc} + \cdots + k_{gd}) N_g - k_{gf} N_g$$

$$= k_{ig} N_i - \sum_{\alpha''}^{a,b,c,\ldots} k_{g\alpha''} N_g - k_{gf} N_g$$

$$\frac{\mathrm{d}N_i}{\mathrm{d}t} = k_{ji} N_j - (k_{ia} + k_{ib} + k_{ic} + \cdots + k_{id}) N_i - k_{ig} N_i = k_{ji} N_j - \sum_{\alpha''}^{a,b,c,\ldots} k_{i\alpha''} N_i - k_{ig} N_i$$

$$\frac{\mathrm{d}N_j}{\mathrm{d}t} = k_{aj} N_a - (k_{ia} + k_{ib} + k_{ic} + \cdots + k_{id}) N_j - k_{ji} N_j = k_{aj} N_a - \sum_{\alpha''}^{a,b,c,\ldots} k_{j\alpha''} N_j - k_{ji} N_j$$

whose summation gives,

$$\frac{\mathrm{d}(N_e + N_f + N_g + N_i + N_j)}{\mathrm{d}t} \equiv \frac{\mathrm{d}N_\beta}{\mathrm{d}t}$$

$$= k_{aj} N_a$$

$$-\left(\sum_{\alpha''}^{a,b,c,\ldots} k_{e\alpha''} N_e + \sum_{\alpha''}^{a,b,c,\ldots} k_{f\alpha''} N_f + \sum_{\alpha''}^{a,b,c,\ldots} k_{g\alpha''} N_g + \cdots + \sum_{\alpha''}^{a,b,c,\ldots} k_{i\alpha''} N_i \right.$$

$$\left. + \sum_{\alpha''}^{a,b,c,\ldots} k_{j\alpha''} N_j \right)$$

or,

$$\frac{\mathrm{d}N_\beta}{\mathrm{d}t} = k_{aj} N_a - \sum_{\beta''}^{e,f,g,\ldots} \sum_{\alpha''}^{a,b,c,\ldots} k_{\beta''\alpha''} N_{\beta''} = -\frac{\mathrm{d}N_\alpha}{\mathrm{d}t}$$

In general, for an $\alpha' \rightarrow \beta'$ excitation

$$\frac{\mathrm{d}N_\alpha(t)}{\mathrm{d}t} = -\frac{\mathrm{d}N_\beta(t)}{\mathrm{d}t} = \sum_{\beta''}^{e,f,g,\ldots} \sum_{\alpha''}^{a,b,c,\ldots} k_{\beta''\alpha''} N_{\beta''}(t) - k_{\alpha'\beta'} N_{\alpha'}(t) \qquad \textbf{Equation A38}$$

where

$$N_\alpha = N_a + N_b + N_c + \cdots + N_d = \sum_{\alpha''}^{a,b,c,\ldots} N_{\alpha''}\,,$$

$$N_\beta = N_e + N_f + N_g + \cdots + N_i + N_j = \sum_{\beta''}^{e,f,g,\ldots} N_{\beta''} \qquad \textbf{Equation A39}$$

Applying the steady-state approximation, $\mathrm{d}N_\alpha/\mathrm{d}t = \mathrm{d}N_\beta/\mathrm{d}t = 0$, yields

$$0 = \sum_{\beta''}^{e,f,g,\ldots} \sum_{\alpha''}^{a,b,c,\ldots} k_{\beta''\alpha''} N_{\beta''} - k_{\alpha'\beta'} N_{\alpha'} \qquad \textbf{Equation A40}$$

where N_α and N_β are no longer time dependent. From the summation, the number of ions or the population in the emitting level, N_e, can be separated as

$$\sum_{\alpha''}^{a,b,c,\ldots} k_{e\alpha''}\, N_e(\alpha' \rightarrow \beta') = k_{\alpha'\beta'} N_{\alpha'} - \sum_{\beta''}^{f,g,\ldots} \sum_{\alpha''}^{a,b,c,\ldots} k_{\beta''\alpha''} N_{\beta''} \qquad \textbf{Equation A41}$$

or

$$k_{e\alpha} N_e(\alpha' \rightarrow \beta') = k_{\alpha'\beta'} N_{\alpha'} - \sum_{\beta''}^{f,g,\ldots} \sum_{\alpha''}^{a,b,c,\ldots} k_{\beta''\alpha''} N_{\beta''}\,, \qquad \textbf{Equation A42}$$

$$k_{e\alpha} = \sum_{\alpha''}^{a,b,c,\ldots} k_{e\alpha''}$$

Considering that the excitation source is not very powerful, then the number of ions in the high-lying excited states $f, g, \ldots$ are vanishing small, because the transition rates from high-lying excited states $k_{\beta\alpha}$ are much smaller than the decay rates within the set of excited states $k_{\beta\beta'}$, then **Equation A42** can be approximated as

$$k_{e\alpha} N_e(\alpha' \rightarrow \beta') \cong k^{\text{abs}}_{\alpha' \rightarrow \beta'} N_{\alpha'}, \qquad k_{e\alpha} = \sum_{\alpha''}^{a,b,c,\ldots} k_{e\alpha''} \qquad \textbf{Equation A43}$$

where the absorption rate associated with the $\alpha' \rightarrow \beta'$ excitation has been made explicit.

Notice that this derivation is general and involves a comprehensive and complete set of energy levels describing 4*f*-4*f* transitions in lanthanide ions.

Employing **Equation A39** as the population of the emitting level upon $\alpha \rightarrow \beta$ and $\alpha' \rightarrow \beta'$ excitations, the thermometric parameter defined in Equation 33 becomes

$$\Delta_i \equiv \frac{S^{\text{ex}}_{\alpha \rightarrow \beta}}{S^{\text{ex}}_{\alpha' \rightarrow \beta'}} = \frac{N_e(\alpha \rightarrow \beta)}{N_e(\alpha' \rightarrow \beta')} = \frac{k^{\text{abs}}_{\alpha \rightarrow \beta} N_{\alpha}}{k^{\text{abs}}_{\alpha' \rightarrow \beta'} N_{\alpha'}} \qquad \textbf{Equation A44}$$

where N_{α} and $N_{\alpha'}$ are the number of ions (or population) at steady state upon continuous excitation from α and α' levels, respectively. It is important to realize that α and α' levels are thermally coupled, and that the continuous excitation is kept long enough to establish thermal

equilibrium at temperature T and steady state. Then, the fraction of ions (or population) in the α level follows the Boltzmann distribution

$$\frac{N_\alpha}{N_{\text{t.c.}}} = g_\alpha e^{-E_\alpha/(kT)}, \qquad N_{\text{t.c.}} = \sum_{\alpha''=a,b,c}^{\text{t.c.}} N_{\alpha''} \qquad \textbf{Equation A45}$$

where $N_{\text{t.c.}}$ is the total number of ions in the sample that are in thermally coupled (t.c.) states, g_α and E_α is the degeneracy and energy of the α level, and k is the Boltzmann constant. Notice that because the populations of the thermally coupled states depend only on the temperature, then $N_{\text{t.c.}}$ is the same for any excitation. Thus, the thermometric parameter in **Equation A40** becomes

$$\Delta_i = \frac{S^{\text{ex}}_{\alpha\to\beta}}{S^{\text{ex}}_{\alpha'\to\beta'}} = \frac{k^{\text{abs}}_{\alpha\to\beta}\, g_\alpha e^{-E_\alpha/(kT)}/N_{\text{t.c.}}}{k^{\text{abs}}_{\alpha'\to\beta'}\, g_{\alpha'} e^{-E_{\alpha'}/(kT)}/N_{\text{t.c.}}} = \frac{k^{\text{abs}}_{\alpha\to\beta} g_\alpha}{k^{\text{abs}}_{\alpha'\to\beta'} g_{\alpha'}} e^{-\Delta E_{\alpha\alpha'}/(kT)} \qquad \textbf{Equation A46}$$

$$= A_i e^{-\Delta E_i/(kT)}$$

where $\Delta E_i \equiv \Delta E_{\alpha\alpha'} = E_\alpha - E_{\alpha'}$ is the energy difference between the low-lying α and α' levels and A_i is a pre-exponential factor that depends only on the ratio of the absorption rates and of the degeneracies.

This derivation of the thermometric parameter considers independent and isolated ions. However, for real samples, the ions are placed in a material medium or matrix with a refractive index, n, which alters the speed of light and affects the transition rates by a dielectric correction $\chi_{\alpha\to\beta}(n)$. The absorption $\alpha \to \beta$ transition rate in a medium with refractive index n is replaced by

$$k^{\text{abs}}_{\alpha\to\beta} \to \frac{k^{\text{abs}}_{\alpha\to\beta}}{\chi^{\text{abs}}_{\alpha\to\beta}(n)} \qquad \textbf{Equation A47}$$

that is, the $\alpha \to \beta$ transition rate in vacuum is replaced by $k^{\text{abs}}_{\alpha\to\beta}/\chi^{\text{abs}}_{\alpha\to\beta}(n)$.

So, the pre-exponential factor, A_i, in the thermometric parameter given by **Equation A42** becomes

$$A_i = \frac{k^{\mathrm{abs}}_{\alpha\to\beta}/\chi^{\mathrm{abs}}_{\alpha\to\beta}(n)\, g_\alpha}{k^{\mathrm{abs}}_{\alpha'\to\beta'}/\chi^{\mathrm{abs}}_{\alpha'\to\beta'}(n)\, g_{\alpha'}} = \frac{\chi^{\mathrm{abs}}_{\alpha'\to\beta'}(n)}{\chi^{\mathrm{abs}}_{\alpha\to\beta}(n)} \frac{k^{\mathrm{abs}}_{\alpha\to\beta} g_\alpha}{k^{\mathrm{abs}}_{\alpha'\to\beta'} g_{\alpha'}}$$

or

$$A_i = f(n)\frac{k^{\mathrm{abs}}_{\alpha\to\beta} g_\alpha}{k^{\mathrm{abs}}_{\alpha'\to\beta'} g_{\alpha'}}, \qquad f(n) = \frac{\chi_{\alpha'\to\beta'}(n)}{\chi_{\alpha\to\beta}(n)} \qquad \textbf{Equation A48}$$

where $f(n)$ is the dielectric factor, which is 1 when both $\alpha \to \beta$ and $\alpha' \to \beta'$ transitions have the same mechanism, so A_i is independent of the temperature. Otherwise, $f(n)$ depends on the refractive index, which varies with the temperature. However, it is shown that $f(n)$ is practically constant in a wide range of temperature. Thus, the thermometers based on excitation spectrum are described by the following thermometric equation

$$\Delta_i = \frac{S^{\mathrm{ex}}_{\alpha\to\beta}}{S^{\mathrm{ex}}_{\alpha'\to\beta'}} = A_i e^{-\Delta E_i/(kT)}, \qquad A_i = f(n)\frac{k^{\mathrm{abs}}_{\alpha\to\beta} g_\alpha}{k^{\mathrm{abs}}_{\alpha'\to\beta'} g_{\alpha'}},$$

$$f(n) = \frac{\chi_{\alpha'\to\beta'}(n)}{\chi_{\alpha\to\beta}(n)} \qquad \textbf{Equation A49} = (19)$$

where the pre-exponential factor A_i can be considered as constant, which demonstrate Equation 19 in the main text.

An immediate prediction from the thermometric equation **Equation A42** consists in selecting bands in the excitation spectrum that have the same initial level, i.e., $\alpha = \alpha'$, which yields $\Delta E_i = 0$ and self-referencing thermometers:

$$\Delta_i = \frac{S^{\mathrm{ex}}_{\alpha\to\beta}}{S^{\mathrm{ex}}_{\alpha\to\beta'}} = A_i = \text{constant} \qquad \textbf{Equation A50}$$

That is, thermometric parameters that do not change with the temperature.

On the other hand, when $\alpha \neq \alpha' \Rightarrow \Delta E_i \neq 0$, the thermometric parameters, Δ_i, have a well-known and well-defined dependence with the temperature and can be employed as primary-T thermometers. In this case, at a known (or reference) temperature, T_0, the thermometric parameter, Δ_{i0}, is determined from the excitation spectrum and allows to predict the temperature as

$$\Delta_i = \frac{S^{\mathrm{ex}}_{\alpha\to\beta}}{S^{\mathrm{ex}}_{\alpha'\to\beta'}} = A_i e^{-\Delta E_i/(kT)} \Rightarrow \ln(\Delta_i/A_i) = -\frac{\Delta E_i}{k}\frac{1}{T} = -\ln(A_i/\Delta_i) \Rightarrow \frac{1}{T} = \frac{k}{\Delta E_i}\ln(A_i/\Delta_i)$$

At a known (or reference) temperature, T_0,

$$\frac{1}{T_0} = \frac{k}{\Delta E_i}\ln(A_i/\Delta_{i0})$$

where the subtraction yields

$$\frac{1}{T} - \frac{1}{T_0} = \frac{k}{\Delta E_i}\ln(A_i/\Delta_i) - \frac{k}{\Delta E_i}\ln(A_i/\Delta_{i0}) = \frac{k}{\Delta E_i}[\ln(A_i/\Delta_i) - \ln(A_i/\Delta_{i0})]$$

$$= \frac{k}{\Delta E_i}\ln\left(\frac{A_i/\Delta_i}{A_i/\Delta_{i0}}\right)$$

or

$$\frac{1}{T} = \frac{1}{T_0} + \frac{k}{\Delta E_i}\ln\left(\frac{\Delta_{i0}}{\Delta_i}\right) = \frac{1}{T_0} - \frac{k}{\Delta E_i}\ln\left(\frac{\Delta_i}{\Delta_{i0}}\right) \qquad \textbf{Equation A51= (14)}$$

which demonstrate Equation 14 in the main text.

The thermometric equation Equation A47 or, Equation 14 in the main text, can promptly provide the relative sensitivity, $S_{\mathrm{r},i}$, of each thermometric parameter Δ_i as[3a]

$$S_{\mathrm{r},i} = \frac{1}{\Delta_i}\left|\frac{\mathrm{d}\Delta_i}{\mathrm{d}T}\right| = \frac{1}{\Delta_i}\left|\frac{\mathrm{d}}{\mathrm{d}T}A_i e^{-\Delta E_i/(kT)}\right| = \frac{1}{\Delta_i}A_i\left|\frac{\mathrm{d}}{\mathrm{d}T}e^{-\Delta E_i/(kT)}\right|$$

$$= \frac{1}{\Delta_i}A_i\left|-\frac{\Delta E_i}{k}e^{-\Delta E_i/(kT)}\frac{\mathrm{d}T^{-1}}{\mathrm{d}T}\right| = \frac{1}{\Delta_i}A_i\left|-\frac{\Delta E_i}{k}e^{-\Delta E_i/(kT)}\left(-\frac{1}{T^2}\right)\right|$$

$$= \frac{\Delta E_i}{k}\frac{1}{T^2}\frac{1}{\Delta_i}A_i e^{-\Delta E_i/(kT)} = \frac{\Delta E_i}{k}\frac{1}{T^2}\frac{1}{\Delta_i}\Delta_i$$

or

$$S_{\mathrm{r},i} = \frac{1}{\Delta_i}\left|\frac{\mathrm{d}\Delta_i}{\mathrm{d}T}\right| = \frac{\Delta E_i}{k}\frac{1}{T^2} \qquad \textbf{Equation A52} = (21)$$

which demonstrate Equation 21 in the main text.

6.1.6. Refractive index and dielectric factor.

The dielectric correction $\chi_{\alpha\to\beta}(n)$ employed to describe the process occurring in a medium or matrix of refractive index n, depends on speed of light entering in the description of the process of interest, such as absorption, spontaneous emission, cross section, or oscillator strength, as well as on the mechanism of the transitions (electric dipole, FED, or magnetic dipole, MD). That is the reason to introduce an explicit dependence on the process (e.g., abs) and on the transition mechanism in the dielectric correction, for instance, $\chi_{\mathrm{ED}}^{\mathrm{abs}}(n)$ or $\chi_{\mathrm{MD}}^{\mathrm{abs}}(n)$ for correcting the absorption rate via electric dipole (FED) or magnetic dipole (MD). The dielectric correction takes into consideration the changes of the speed of light in the medium as well as the effects of the local field on the electric dipole. These dielectric factors are summarized in Table A7.

Table A7. Dielectric corrections $\chi(n)$ for a non-magnetic dielectric medium with refractive index n and a local field correction χ_{L}.[90]

Quantity	Forced Electric dipole (FED)	Magnetic Dipole (MD)
Absorption and stimulated emission rates	$\chi(n) = n^3\chi_{\mathrm{L}}$	$\chi(n) = n^5$
Spontaneous emission rates	$\chi(n) = n\chi_{\mathrm{L}}$	$\chi(n) = n^3$
Cross sections and oscillator strengths	$\chi(n) = \frac{1}{n}\chi_{\mathrm{L}}$	$\chi(n) = n$

It is noteworthy that the ratio of $\chi_{\mathrm{ED}}(n)$ to $\chi_{\mathrm{MD}}(n)$, which is denoted as the dielectric factor $f_{\mathrm{process}}(n)$, is the same for absorption, stimulated, and spontaneous emission rates, namely,

$$f_{\mathrm{abs}}(n) = \frac{\chi_{\mathrm{ED}}^{\mathrm{abs}}(n)}{\chi_{\mathrm{MD}}^{\mathrm{abs}}(n)} = f_{\mathrm{stim}}(n) = \frac{\chi_{\mathrm{ED}}^{\mathrm{stim}}(n)}{\chi_{\mathrm{MD}}^{\mathrm{stim}}(n)} = \frac{n^3\chi_{\mathrm{L}}}{n^5} = \frac{\chi_{\mathrm{L}}}{n^2} = f(n),$$

$$f_{\mathrm{spon}}(n) = \frac{\chi_{\mathrm{ED}}^{\mathrm{spon}}(n)}{\chi_{\mathrm{MD}}^{\mathrm{spon}}(n)} = \frac{n\chi_{\mathrm{L}}}{n^3} = \frac{\chi_{\mathrm{L}}}{n^2} = f(n) \qquad \textbf{Equation A53}$$

Of course, the ratio of $\chi_{\mathrm{MD}}(n)$ to $\chi_{\mathrm{ED}}(n)$ is the same for rate processes. Therefore, for transition rates, the dielectric factors are the same for all processes and will be denoted simply as $f(n)$.

The local field correction χ_{L} is[90]

$$\chi_{\mathrm{L}} = \left(\frac{\mathcal{E}_{\mathrm{eff}}}{\mathcal{E}_0}\right)^2 \qquad \textbf{Equation A54}$$

where $\mathcal{E}_{\mathrm{eff}}$ is the actual or effective or local field at the optical center and $\mathcal{E}_0$ is the average field in the medium. For tightly bound centers, it can be shown that[90]

$$\chi_{\mathrm{L}} = \left(\frac{\mathcal{E}_{\mathrm{eff}}}{\mathcal{E}_0}\right)^2 \cong \left(1 + \frac{n^2 - 1}{3} + O((n^2 - 1)^2/9) + J + X + K\right)^2 \qquad \textbf{Equation A55}$$

where the first correction is known as the Lorentz local field ratio, and it is the only important term for well-localized center in a tightly bound matrix. The next term is of the order of the square of the Lorentz correction, whereas J, X, K represent corrections arising from overlap of neighbouring atom wave functions, exchange effects, and higher multipole interactions, respectively. Lanthanide ions do satisfy the condition of a well-localized center in a tightly bound matrix, so[91]

$$\chi_{\mathrm{L}} = \left(1 + \frac{n^2 - 1}{3}\right)^2 = \left(\frac{n^2 + 2}{3}\right)^2 = \frac{(n^2 + 2)^2}{9} \qquad \textbf{Equation A56}$$

As a result, the dielectric factor becomes

$$f(n) = \frac{\chi_{\mathrm{L}}}{n^2} \cong \frac{(n^2 + 2)^2}{9n^2} \qquad \textbf{Equation A57}$$

which has a weak dependence on the refractive index n as illustrated in Figure A29 for n varying from 1.0 to 2.5 and from 1.5 to 1.6.

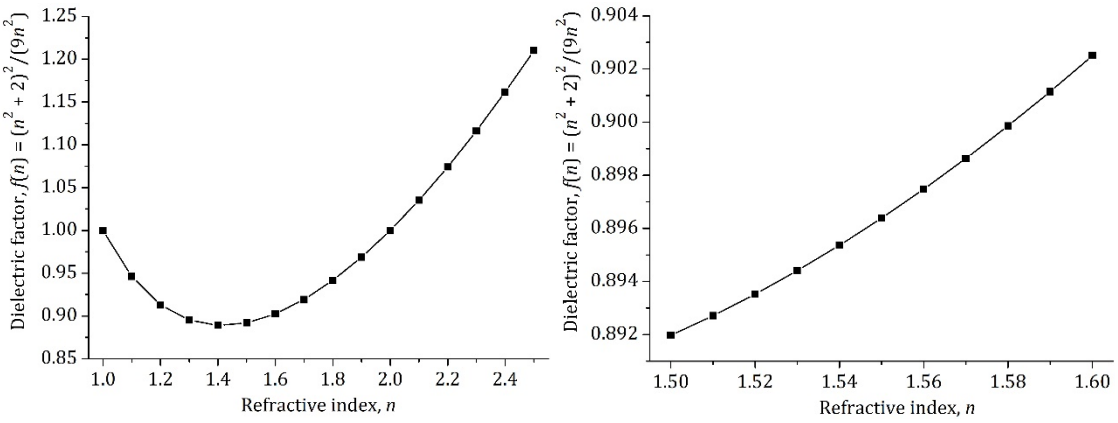

Figure A29. Dependence of the dielectric factor $f(n) = (n^2 + 2)^2/9n^2$ with the refractive index n in the range of 1.0 to 2.5 (left panel) and of 1.5 to 1.6 (right panel). Source: Author.

6.1.7.Temperature dependence of the refractive index.

The dielectric factor, $f(n)$, has a weak dependence on n (Figure A29) and the refractive index varies slowly with the temperature, which leads to a very weak dependence of $f(n)$ on the temperature (Figure A30). For typical values of the refractive index (*e.g.,* 1.55), the dielectric factor $f(n)$ varies less than 0.05% in the temperature range 10−400 K for materials with thermo-optic coefficient[69] of ca. 10^{-5} K^{-1}.[70] Even for materials with large thermo-optic coefficient of ca. 10^{-4} K^{-1}, the variation of $f(n)$ in this temperature range is less than 0.5% (Figure A30). As a result, the dielectric factor $f(n)$ in the pre-exponential factor of the thermometric parameter can be considered constant (independent of the temperature). The refractive index of most materials varies with temperature as[69-70]

$$n(T) = n_0 + aT, \qquad a = \frac{\mathrm{d}n}{\mathrm{d}T} \qquad \textbf{Equation A58}$$

where n_0 is the refractive index near 0 K and a is the thermo-optic coefficient of the material. So, the dependence of the dielectric factor in **Equation A53** with the temperature becomes

$$f(n(T)) \cong \frac{[(n_0 + aT)^2 + 2]^2}{9(n_0 + aT)^2} \qquad \textbf{Equation A59}$$

and its variation with temperature is depicted in Figure A30.

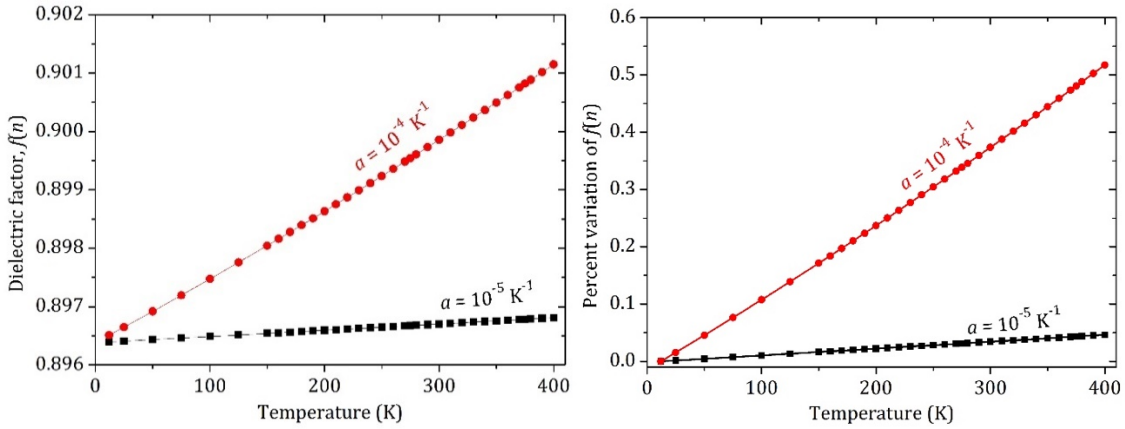

Figure A30. Dependence of the dielectric factor $f(n) = (n^2 + 2)^2/9n^2$ with the temperature (left panel) and the relative (percentage) variation of f(n) with temperature (right panel) for a refractive index at 0 K of $n_0 = 1.55$ and thermo-optic coefficient a of 10^{-4} K^{-1} and 10^{-5} K^{-1}. Source: Author.

Clearly, for typical thermo-optic coefficient $a \sim 10^{-5}$ K^{-1}, the dielectric factor $f(n)$ is constant in a wide range of temperature, e.g., from 10 to 400 K the change in $f(n)$ is ca. 0.05%, whereas for atypically large thermo-optic coefficient $a \sim 10^{-4}$ K^{-1}, relative variation of the dielectric factor is ca. 0.5% within [10−400 K]. As a result, $f(n)$ in the pre-exponential factor of the thermometric parameter can be considered independent on the temperature.

6.1.8. Primary-S thermometers (excitation and emission spectra).

The proposed thermometric parameter becomes also a primary-S thermometer if the absorption transition rates, $k_{\alpha\to\beta}^{\mathrm{abs}}$, in the pre-exponential factor can be determined. It is shown that $k_{\alpha\to\beta}^{\mathrm{abs}}$ can be related to the corresponding stimulated, $k_{\beta\to\alpha}^{\mathrm{stim}}$, and spontaneous, $A_{\beta\to\alpha}$, emission rates, which could be determined from the emission spectrum. Therefore, the pre-exponential factor A_i becomes known from another spectral measurement, hence a primary-S thermometer.

Consider the transition from the lower energy α level by absorption of photons to a higher energy β level, which can be transitioned back to the α level by stimulated and spontaneous emissions. These two α and β levels are characterized by the total angular momentum quantum numbers J_α and J_β, the crystal quantum numbers μ_α and μ_β, and additional sets of numbers Ψ_α and Ψ_β. Within the Fermi's golden rule approximation,[92] the absorption rate can be expressed as,[72b]

$$k_{\alpha\to\beta}^{\text{abs}} = \frac{64\pi^4\nu_{\alpha\beta}^3 D_{\alpha,\beta}}{3hc^3 g_\alpha} N_{\nu_{\alpha\beta}} \to g_\alpha k_{\alpha\to\beta}^{\text{abs}} = \frac{64\pi^4\nu_{\alpha\beta}^3 D_{\alpha,\beta}}{3hc^3} N_{\nu_{\alpha\beta}} \qquad \textbf{Equation A60}$$

the stimulated emission as,

$$k_{\beta\to\alpha}^{\text{stim}} = \frac{64\pi^4\nu_{\alpha\beta}^3 D_{\alpha,\beta}}{3hc^3 g_\beta} N_{\nu_{\alpha\beta}} \to g_\beta k_{\beta\to\alpha}^{\text{stim}} = \frac{64\pi^4\nu_{\alpha\beta}^3 D_{\alpha,\beta}}{3hc^3} N_{\nu_{\alpha\beta}} \qquad \textbf{Equation A61}$$

and spontaneous emission as

$$A_{\beta\to\alpha} = \frac{64\pi^4\nu_{\alpha\beta}^3 D_{\alpha,\beta}}{3hc^3 g_\beta} \to g_\beta A_{\beta\to\alpha} N_{\nu_{\alpha\beta}} = \frac{64\pi^4\nu_{\alpha\beta}^3 D_{\alpha,\beta}}{3hc^3} N_{\nu_{\alpha\beta}} \qquad \textbf{Equation A62}$$

where $D_{\alpha,\beta}$ is the (electric and magnetic) dipole strength and $N_{\nu_{\alpha\beta}}$ is the number of photons with frequency $\nu_{\alpha\beta}$ in a volume V, which is given by[93]

$$N_{\nu_{\alpha\beta}} = \frac{\pi A_0^2 V}{2hc^2}\nu_{\alpha\beta} \qquad \textbf{Equation A63}$$

with A_0 being the strength of the vector potential of the radiation field.

It thus follows that,

$$\begin{aligned} g_\alpha k_{\alpha\to\beta}^{\text{abs}} = \frac{64\pi^4\nu_{\alpha\beta}^3 D_{\alpha,\beta}}{3hc^3} N_{\nu_{\alpha\beta}} &= g_\beta k_{\beta\to\alpha}^{\text{stim}} = g_\beta A_{\beta\to\alpha} N_{\nu_{\alpha\beta}} \\ &= g_\beta A_{\beta\to\alpha} \frac{\pi A_0^2 V}{2hc^2}\nu_{\alpha\beta} \end{aligned} \qquad \textbf{Equation A64}$$

The integrated intensity $I_{\mathrm{em}}(\beta \to \alpha)$, in energy per unit of time, of a $\beta \to \alpha$ transition is[89]

$$I_{\mathrm{em}}(\beta \to \alpha) \propto h\nu_{\alpha\beta} A_{\beta\to\alpha} N_\beta \qquad \textbf{Equation A65}$$

where N_β is the number of emitters in state β. This expression is valid for emissions in the optical region because the stimulated emission $k_{\beta\to\alpha}^{\mathrm{stim}}$ is negligible, so the total radiative rate $k_{\beta\to\alpha}^{\mathrm{rad}}$ is approximated by the spontaneous emission $A_{\iota\to\alpha}$.[94]

Then, the absorption rate becomes,

$$g_\alpha k_{\alpha\to\beta}^{\mathrm{abs}} = \frac{\pi A_0^2 V g_\beta}{2h^2c^2N_\beta} h\nu_{\alpha\beta} A_{\beta\to\alpha} N_\beta \propto \frac{\pi A_0^2 V g_\beta}{2h^2c^2N_\beta} I_{\mathrm{em}}(\beta \to \alpha) \qquad \textbf{Equation A66}$$

The integrated intensity $I_{\mathrm{em}}(\beta \to \alpha)$ is proportional to the area $S_{\beta\to\alpha}^{\mathrm{em}}$ of the band in the emission spectrum corresponding to the $\beta \to \alpha$ transition, namely[67]

$$I_{\mathrm{em}}(\beta \to \alpha) = k_{\mathrm{g}} S_{\beta\to\alpha}^{\mathrm{em}} = k_{\mathrm{g}} \int_{\beta\to\alpha} I(\nu)\mathrm{d}\nu \qquad \textbf{Equation A67}$$

where the proportionality constant k_{g} depends on several experimental parameters such as slit widths, geometry, solid angle, detector sensibility, etc.

This gives the following relation

$$g_\alpha k_{\alpha\to\beta}^{\mathrm{abs}} \propto \frac{\pi A_0^2 V g_\beta}{2h^2c^2N_\beta} I_{\mathrm{em}}(\beta \to \alpha) = \frac{k_g \pi A_0^2 V g_\beta}{2h^2c^2N_\beta} S_{\beta\to\alpha}^{\mathrm{em}} \qquad \textbf{Equation A68}$$

This relationship is valid for isolated and independent optical centers. However, the right hand-side of Eq. (S61) is related to measurements on actual samples. In other words, the area $S_{\beta\to\alpha}^{\mathrm{em}}$ takes into consideration that the optical centres are within a material medium. So, if this medium is a non-magnetic dielectric one, described by a refractive index n, then the measured area $S_{\beta\to\alpha}^{\mathrm{em}}$ becomes dependent on n, that is, $S_{\beta\to\alpha}^{\mathrm{em}}(n)$, and it should be corrected to

the corresponding value for isolated centres. As discussed before, in the determination of the absorption rate in this medium, the area $S^{\mathrm{em}}_{\beta\to\alpha}$ should be

$$k^{\mathrm{abs}}_{\alpha\to\beta} \to \frac{k^{\mathrm{abs}}_{\alpha\to\beta}}{\chi^{\mathrm{abs}}_{\alpha\to\beta}(n)} \Rightarrow S^{\mathrm{em}}_{\beta\to\alpha} \to \frac{S^{\mathrm{em}}_{\beta\to\alpha}}{\chi^{\mathrm{abs}}_{\alpha\to\beta}(n)} \qquad \textbf{Equation A69}$$

as presented in **Equation A43**, where $\chi^{\mathrm{abs}}_{\alpha\to\beta}(n)$ is the dielectric correction.

As a result, the absorption rate expression in terms of the measured area should be

$$g_\alpha k^{\mathrm{abs}}_{\alpha\to\beta} \propto \frac{\pi A_0^2 V g_\beta}{2h^2c^2N_\beta} I_{\mathrm{em}}(\beta\to\alpha) = \frac{k_g \pi A_0^2 V g_\beta}{2h^2c^2N_\beta} \frac{S^{\mathrm{em}}_{\beta\to\alpha}}{\chi^{\mathrm{abs}}_{\alpha\to\beta}(n)} \qquad \textbf{Equation A70}$$

with $S^{\mathrm{em}}_{\beta\to\alpha}$ being the area of the band measured in the actual sample (optical centers in a dielectric medium).

Considering two transitions with the same final state, namely, $\alpha\to\beta$ and $\alpha'\to\beta$, the associated pre-exponential factor in the thermometric parameter becomes

$$A_i = \frac{g_\alpha k^{\mathrm{abs}}_{\alpha\to\beta}}{g_{\alpha'} k^{\mathrm{abs}}_{\alpha'\to\beta}} = \frac{\frac{k_g \pi A_0^2 V g_\beta}{2h^2c^2N_\beta} \frac{S^{\mathrm{em}}_{\beta\to\alpha}}{\chi^{\mathrm{abs}}_{\alpha\to\beta}}}{\frac{k_g \pi A_0^2 V g_\beta}{2h^2c^2N_\beta} \frac{S^{\mathrm{em}}_{\beta\to\alpha'}}{\chi^{\mathrm{abs}}_{\alpha'\to\beta}}} = \frac{\chi^{\mathrm{abs}}_{\alpha'\to\beta}(n)}{\chi^{\mathrm{abs}}_{\alpha\to\beta}(n)} \frac{S^{\mathrm{em}}_{\beta\to\alpha}}{S^{\mathrm{em}}_{\beta\to\alpha'}} = f(n) \frac{S^{\mathrm{em}}_{\beta\to\alpha}}{S^{\mathrm{em}}_{\beta\to\alpha'}} \qquad \textbf{Equation A71}$$

In the case where the emission intensity $I_{\mathrm{em}}(\beta\to\alpha)$ is measured as the number of emitted photons per unit of time (photon counting per second), the integrated intensity is

$$I_{\mathrm{em}}(\beta\to\alpha) \propto A_{\beta\to\alpha} N_\beta = k_g \frac{S^{\mathrm{em}}_{\beta\to\alpha}}{\chi^{\mathrm{abs}}_{\alpha\to\beta}(n)} \qquad \textbf{Equation A72}$$

So, the absorption rate in **Equation A60** becomes

$$g_\alpha k^{\text{abs}}_{\alpha\to\beta} = \frac{\pi A_0^2 V g_\beta}{2hc^2}\nu_{\alpha\beta}A_{\beta\to\alpha} = \frac{\pi A_0^2 V g_\beta \nu_{\alpha\beta}}{2hc^2 N_\beta}A_{\beta\to\alpha}N_\beta$$

$$\propto \frac{\pi A_0^2 V g_\beta \nu_{\alpha\beta}}{2hc^2 N_\beta} I_{\text{em}}(\beta\to\alpha) = \frac{\pi A_0^2 V g_\beta \nu_{\alpha\beta}}{2hc^2 N_\beta} k_g \frac{S^{\text{em}}_{\beta\to\alpha}}{\chi^{\text{abs}}_{\alpha\to\beta}(n)} \quad \textbf{Equation A73}$$

$$= \frac{\pi A_0^2 V g_\beta k_g}{2hc^2 N_\beta}\frac{\nu_{\alpha\beta}S^{\text{em}}_{\beta\to\alpha}}{\chi^{\text{abs}}_{\alpha\to\beta}(n)}$$

upon substitution of Eq. (S65). The pre-exponential factor is written as

$$A_i = \frac{g_\alpha k^{\text{abs}}_{\alpha\to\beta}}{g_{\alpha'}k^{\text{abs}}_{\alpha'\to\beta}} = \frac{\chi^{\text{abs}}_{\alpha'\to\beta}(n)}{\chi^{\text{abs}}_{\alpha\to\beta}(n)}\frac{\nu_{\alpha\beta}}{\nu_{\alpha'\beta}}\frac{S^{\text{em}}_{\beta\to\alpha}}{S^{\text{em}}_{\beta\to\alpha'}} = f(n)\frac{\nu_{\alpha\beta}}{\nu_{\alpha'\beta}}\frac{S^{\text{em}}_{\beta\to\alpha}}{S^{\text{em}}_{\beta\to\alpha'}} \quad \textbf{Equation A74}$$

In summary,

$$A_i = f(n)\frac{S^{\text{em}}_{\beta\to\alpha}(\text{power})}{S^{\text{em}}_{\beta\to\alpha'}(\text{power})} = f(n)\frac{\nu_{\alpha\beta}}{\nu_{\alpha'\beta}}\frac{S^{\text{em}}_{\beta\to\alpha}(\text{photon counting})}{S^{\text{em}}_{\beta\to\alpha'}(\text{photon counting})}, \quad \textbf{Equation A75}$$

$$f(n) = \frac{\chi_{\alpha'\to\beta'}(n)}{\chi_{\alpha\to\beta}(n)}$$

where $S^{\text{em}}_{\beta\to\alpha}(\text{power})$ and $S^{\text{em}}_{\beta\to\alpha}(\text{photon counting})$ is the area of the band in the emission acquired as energy per unit of time (power) and as number of photons per unit of time (photon counting), respectively. As discussed before, the dielectric factor $f(n)$ is 1 when both transitions have the same dipole character, whereas it is practically constant (independent of temperature) for transition with distinct dipole character. However, despite being constant, the value of $f(n)$ needs to be considered when determining the pre-exponential factor of the thermometric parameter.

Primary-S thermometers can then predict the temperature as

$$T = \frac{\Delta E_i}{k}\frac{1}{\ln(A_i/\Delta_i)}, \qquad \Delta_i = \frac{S^{\text{ex}}_{\alpha\to\beta}}{S^{\text{ex}}_{\alpha'\to\beta}} \quad \textbf{Equation A76}$$

where

$$A_i = f(n)\frac{S^{\mathrm{em}}_{\beta\to\alpha}(\text{power})}{S^{\mathrm{em}}_{\beta\to\alpha'}(\text{power})} = f(n)\frac{\tilde{\nu}_{\alpha\beta}}{\tilde{\nu}_{\alpha'\beta}}\frac{S^{\mathrm{em}}_{\beta\to\alpha}(\text{photon counting})}{S^{\mathrm{em}}_{\beta\to\alpha'}(\text{photon counting})},$$

$$f(n) = \frac{\chi_{\alpha'\to\beta'}(n)}{\chi_{\alpha\to\beta}(n)} \qquad \textbf{Equation A77}$$

which demonstrate Equation 4 in the main text.

So, the temperature can be predicted by determining the thermometric parameter Δ_i from the excitation spectrum and the pre-exponential factor A_i from the integrated intensities in the emission spectrum, corrected by the dielectric factor $f(n)$, and by the ratio of the wavenumbers in the case of acquiring the emission spectrum in the photon counting mode.

For instance, consider the thermometric parameter associated with $^7\mathrm{F}_1 \to {}^5\mathrm{D}_0$ (MD) and $^7\mathrm{F}_0 \to {}^5\mathrm{D}_0$ (ED) transitions in the excitation spectrum and the corresponding $^5\mathrm{D}_0 \to {}^7\mathrm{F}_1$ (MD) and $^5\mathrm{D}_0 \to {}^7\mathrm{F}_0$ (ED) transitions in the emission spectrum, which lead to:

$$\Delta_i = \frac{S^{\mathrm{ex}}_{\alpha\to\beta}}{S^{\mathrm{ex}}_{\alpha'\to\beta}} = \frac{S^{\mathrm{ex}}_{^7\mathrm{F}_1\to{}^5\mathrm{D}_0}}{S^{\mathrm{ex}}_{^7\mathrm{F}_0\to{}^5\mathrm{D}_0}} \qquad \textbf{Equation A78}$$

and

$$A_i = \frac{\chi_{\alpha'\to\beta'}(n)}{\chi_{\alpha\to\beta}(n)}\frac{\tilde{\nu}_{\alpha\beta}}{\tilde{\nu}_{\alpha'\beta}}\frac{S^{\mathrm{em}}_{\beta\to\alpha}}{S^{\mathrm{em}}_{\beta\to\alpha'}} = \frac{\chi_{^7\mathrm{F}_0\to{}^5\mathrm{D}_0}(n)}{\chi_{^7\mathrm{F}_1\to{}^5\mathrm{D}_0}(n)}\frac{\tilde{\nu}_{01}}{\tilde{\nu}_{00}}\frac{S^{\mathrm{em}}_{^5\mathrm{D}_0\to{}^7\mathrm{F}_1}}{S^{\mathrm{em}}_{^5\mathrm{D}_0\to{}^7\mathrm{F}_0}}$$

$$= \frac{\chi_{\mathrm{ED}}(n)}{\chi_{\mathrm{MD}}(n)}\frac{\tilde{\nu}_{01}}{\tilde{\nu}_{00}}\frac{S^{\mathrm{em}}_{^5\mathrm{D}_0\to{}^7\mathrm{F}_1}}{S^{\mathrm{em}}_{^5\mathrm{D}_0\to{}^7\mathrm{F}_0}} = f(n)\frac{\tilde{\nu}_{01}}{\tilde{\nu}_{00}}\frac{S^{\mathrm{em}}_{^5\mathrm{D}_0\to{}^7\mathrm{F}_1}}{S^{\mathrm{em}}_{^5\mathrm{D}_0\to{}^7\mathrm{F}_0}} \qquad \textbf{Equation A79}$$

where

$$f(n) = \frac{\chi_{\mathrm{L}}}{n^2} \cong \frac{(n^2+2)^2}{9n^2}. \qquad \textbf{Equation A80}$$

Therefore, knowing the refractive index n allows to estimate $f(n)$, and measuring the integrated intensities, $S^{\mathrm{em}}_{\beta\to\alpha}$, in the emission spectrum as well as the barycenter of the transitions, $\tilde{\nu}_{\alpha\beta}$, the pre-exponential factor, A_i, of the thermometer becomes fully determined.

6.2. PUBLICATIONS

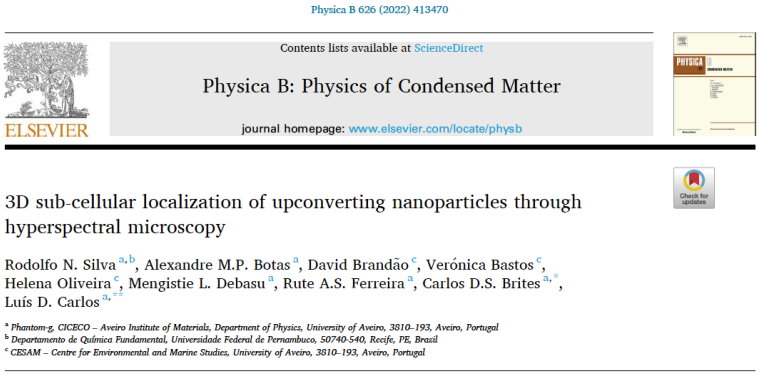

Physica B 626 (2022) 413470

Contents lists available at ScienceDirect

Physica B: Physics of Condensed Matter

journal homepage: www.elsevier.com/locate/physb

3D sub-cellular localization of upconverting nanoparticles through hyperspectral microscopy

Rodolfo N. Silva [a,b], Alexandre M.P. Botas [a], David Brandão [c], Verónica Bastos [c], Helena Oliveira [c], Mengistie L. Debasu [a], Rute A.S. Ferreira [a], Carlos D.S. Brites [a,*], Luís D. Carlos [a,*]

[a] Phantom-g, CICECO – Aveiro Institute of Materials, Department of Physics, University of Aveiro, 3810-193, Aveiro, Portugal
[b] Departamento de Química Fundamental, Universidade Federal de Pernambuco, 50740-540, Recife, PE, Brasil
[c] CESAM – Centre for Environmental and Marine Studies, University of Aveiro, 3810-193, Aveiro, Portugal

https://doi.org/10.1016/j.physb.2021.413470

RESEARCH ARTICLE

Editor's Choice

ADVANCED OPTICAL MATERIALS

www.advopticalmat.de

Novel and High-Sensitive Primary and Self-Referencing Thermometers Based on the Excitation Spectra of Lanthanide Ions

Keyla M. N. de Souza, Rodolfo N. Silva, Juliana A. B. Silva, Carlos D. S. Brites, Biju Francis, Rute A. S. Ferreira, Luís D. Carlos, and Ricardo L. Longo**

https://doi.org/10.1002/adom.202200770

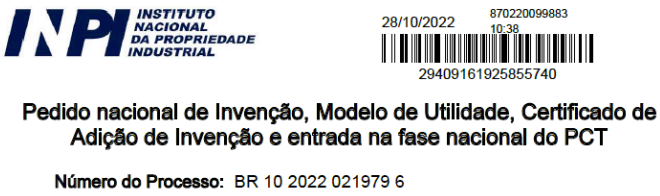

INPI INSTITUTO NACIONAL DA PROPRIEDADE INDUSTRIAL

28/10/2022 870220099883 10:38

29409161925855740

Pedido nacional de Invenção, Modelo de Utilidade, Certificado de Adição de Invenção e entrada na fase nacional do PCT

Número do Processo: BR 10 2022 021979 6

Ricardo Luiz Longo, Keyla Mirelly Nunes de Souza, Rodolfo Rodrigues Nunes da Silva, Luís António Ferreira Martins Dias Carlos, Maria Rute de Amorim e Sá Ferreira André, Carlos António Delgado Sousa Brites e Juliana Angeiras Batista da Silva.

6.3. RESUMO SIMPLIFICADO

Íons de Lantanídeos: Revolucionando a Medição de Temperatura

Um estudo recente introduziu dois termômetros primários: o primary-T, que necessita de calibração em apenas uma temperatura conhecida e utiliza dados ratiométricos autorreferenciados dos espectros de excitação, e o primary-S, que supera o primary-T por não precisar de nenhuma calibração e utiliza dados ratiométricos originários tanto dos espectros de excitação quanto de emissão. Termômetros primários são desenvolvidos a partir de princípios físicos e requerem uma calibração mínima em temperaturas pré determinadas. Estes novos termômetros foram desenvolvidos na tese de doutorado em regime de cotutela desenvolvida em colaboração entre o Programa de Pós-Graduação erm Química do Departamento de Química Fundamental (DQF), da Universidade Federal de Pernambuco (UFPE) e o CICECO – Instituto de Materiais de Aveiro, e Departamento de Física da Universidade de Aveiro (UA). O estudante, Rodolfo Silva, teve a orientação científica dos doutores Ricardo Longo e Ivani Malvestiti, Professor Titular e Professora Associada, respectivamente, do DQF da UFPE, e Luís António Ferreira Martins Dias Carlos e Maria Rute de Amorim e Sá Ferreira André, Professores Catedráticos do Departamento de Física da Universidade de Aveiro (Portugal). A tese foi financiada por fundos portugueses (NanoHeatControl, The Shape of Water e LogicALL) e europeu (NanoTBTech) de fomento a ciência e a tecnologia.

Prova de Conceito: O estudante utilizou um complexo Eu(III)-β-dicetonato para determinar a temperatura e demonstraram a aplicabilidade universal do método para outros materiais à base de Ln(III), alcançando uma precisão de 0,2% na faixa de temperatura fisiológica, superando as tecnologias existentes.

Microscopia Hiperespectral: Unindo Informações Espectrais e Espaciais

A pesquisa se estendeu à microscopia hiperespectral, combinando espectroscopia com microscopia óptica para obter informações espectrais e espaciais simultaneamente. Esta técnica revolucionou as aplicações biomédicas, auxiliando no monitoramento de agentes de bioimagem, detecção de patógenos, identificação de células cancerígenas e avaliação da absorção de nanopartículas. Nanopartículas são partículas que têm aproximadamente o tamanho 1000 vezes menor que um fio de cabelo.

Uma Estratégia Potencial em Oncologia - Foram preparadas nanopartículas de Gd_2O_3 dopadas com Yb(III)/Er(III), analisando suas propriedades estruturais e luminescentes. Eles estudaram a viabilidade celular dessas partículas com linhagens de células de melanoma humano (MNT-1 e A375). Usando imagem hiperespectral 2D, eles acompanharam o processo de internalização e mapearam a distribuição 3D nas culturas celulares. As partículas estavam localizadas principalmente nas regiões citoplasmática e ao redor do núcleo da célula. Foi possível determinar a temperatura intracelular utilizando esse método.

Implicações Futuras - Esses avanços abrem novas possibilidades na medição de temperatura e imagem biomédica, tornando os termômetros primários e a microscopia hiperespectral adequados para monitoramento preciso em diagnósticos médicos e ciência dos materiais. À medida que esses métodos evoluem, provavelmente criarão novas oportunidades na pesquisa científica e nas aplicações práticas.

7. REFERENCES.

[1] R. Paricio-Montesinos, F. Schwaller, A. Udhayachandran, F. Rau, J. Walcher, R. Evangelista, J. Vriens, T. Voets, J. F. A. Poulet, G. R. Lewin, *Neuron* **2020**, 106, 830.

[2] M. Quintanilla, A. Benayas, R. Naccache, F. Vetrone, in *Thermometry at the Nanoscale: Techniques and Selected Applications*, DOI: 10.1039/9781782622031-00124, The Royal Society of Chemistry, 2016, 124.

[3] a) L. D. Carlos, F. Palacio, *Thermometry at the Nanoscale: Techniques and Selected Applications*, Royal Society of Chemistry, Oxfordshire **2016**; b) C. D. S. Brites, S. Balabhadra, L. D. Carlos, *Advanced Optical Materials* **2019**, 7, 1801239.

[4] H. Zhang, Y. Wu, Z. Gan, Y. Yang, Y. Liu, P. Tang, D. Wu, **2019**, 7, 2835.

[5] C. D. S. Brites, P. P. Lima, N. J. O. Silva, A. Millán, V. S. Amaral, F. Palacio, L. D. Carlos, *Nanoscale* **2012**, 4, 4799.

[6] M. Jia, Z. Fu, G. Liu, Z. Sun, P. Li, A. Zhang, F. Lin, B. Hou, G. Chen, *Advanced Optical Materials* **2020**, 8, 1901173.

[7] a) R. Pinol, J. Zeler, C. D. S. Brites, Y. Y. Gu, P. Tellez, A. N. C. Neto, T. E. da Silva, R. Moreno-Loshuertos, P. Fernandez-Silva, A. I. Gallego, L. Martinez-Lostao, A. Martinez, L. D. Carlos, A. Millan, *Nano Letters* **2020**, 20, 6466; b) A. M. Kaczmarek, Y. Y. Liu, M. K. Kaczmarek, H. S. Liu, F. Artizzu, L. D. Carlos, P. Van Der Voort, *Angewandte Chemie-International Edition* **2020**, 59, 1932; c) J. Y. R. Silva, Y. G. Proenza, L. L. Da Luz, S. De Sousa Araújo, M. A. G. Filho, S. A. Junior, T. A. Soares, R. L. Longo, *Materials Science and Engineering: C* **2019**, 102, 578; d) A. M. Ibarra-Ruiz, D. C. Rodríguez Burbano, J. A. Capobianco, *Advances in Physics: X* **2016**, 1, 194.

[8] C. D. S. Brites, P. P. Lima, L. D. Carlos, *Journal of Luminescence* **2016**, 169 B, 497.

[9] a) M. L. Debasu, H. Oliveira, J. Rocha, L. D. Carlos, in *Journal of Rare Earths*, Vol. 38, Elsevier Ltd, 2020, 483; b) A. R. N. Bastos, C. D. S. Brites, P. A. Rojas-Gutierrez, R. A. S. Ferreira, R. L. Longo, C. Dewolf, J. A. Capobianco, L. D. Carlos, *Nanoscale* **2020**, 12, 24169; c) G. A. Mandl, P. A. Rojas-Gutierrez, J. A. Capobianco, *Chemical Communications* **2018**, 54, 5847; d) P. A. Rojas-Gutierrez, D. Bekah, J. Seuntjens, C. DeWolf, J. A. Capobianco, *ACS Applied Bio Materials* **2019**, 2, 4527.

[10] D. M. Samhadaneh, G. A. Mandl, Z. Han, M. Mahjoob, S. C. Weber, M. Tuznik, D. A. Rudko, J. A. Capobianco, U. Stochaj, *ACS Applied Bio Materials* **2020**, 3, 4358.

[11] a) M. Back, E. Casagrande, C. A. Brondin, E. Ambrosi, D. Cristofori, J. Ueda, S. Tanabe, E. Trave, P. Riello, *ACS Applied Nano Materials* **2020**, 3, 2594; b) C. D. S. Brites, P. P. Lima, N. J. O. Silva, A. Millán, V. S. Amaral, F. Palacio, L. D. Carlos, *Nanoscale* **2013**, 5, 7572; c) C. D. S. Brites, P. P. Lima, N. J. O. Silva, A. Millán, V. S. Amaral, F. Palacio, L. D. Carlos, *Journal of Luminescence* **2013**, 133, 230.

[12] J.-C. G. Bünzli, *Coordination Chemistry Reviews* **2015**, 293, 19.

[13] A. N. Carneiro Neto, E. E. S. Teotonio, G. F. de Sá, H. F. Brito, J. Legendziewicz, L. D. Carlos, M. C. F. C. Felinto, P. Gawryszewska, R. T. Moura, R. L. Longo, W. M. Faustino, O. L. Malta, in *Handbook on the Physics and Chemistry of Rare Earths*, Vol. 56 (Eds: J.-C. G. Bünzli, V. K. Pecharsky), Elsevier B.V., Amsterdam **2019**, Ch. 310 p. 55.

[14] M. Sójka, J. F. C. B. Ramalho, C. D. S. Brites, K. Fiaczyk, L. D. Carlos, E. Zych, *Advanced Optical Materials* **2019**, 7, 1901102.

[15] J. C. Martins, A. R. N. Bastos, R. A. S. Ferreira, X. Wang, G. Chen, L. D. Carlos, *Advanced Photonics Research* **2021**, 2, 2000169.

[16] a) D. Pugh-Thomas, B. M. Walsh, M. C. Gupta, *Nanotechnology* **2011**, 22, 185503; b) A. M. P. Botas, C. D. S. Brites, J. Wu, U. Kortshagen, R. N. Pereira, L. D. Carlos, R. A. S. Ferreira, *Particle and Particle System Characterization* **2016**, 33, 740.

[17] a) E. D. Martínez, C. D. S. Brites, L. D. Carlos, A. F. García-Flores, R. R. Urbano, C. Rettori, *Advanced Functional Materials* **2019**, 29, 1807758; b) A. S. Souza, L. A. O. Nunes, I. G. N. Silva, F. A. M. Oliveira, L. L. da Luz, H. F. Brito, M. C. F. C. Felinto, R. A. S. Ferreira, S. A. Junior, L. D. Carlos, O. L. Malta, *Nanoscale* **2016**, 8, 5327; c) S. Balabhadra, M. L. Debasu, C. D. S. Brites, R. A. S. Ferreira, L. D. Carlos, *Journal of Physical Chemistry C* **2017**, 121, 13962; d) J. F. C. B. Ramalho, S. F. H. Correia, L. S. Fu, L. L. F. Antonio, C. D. S. Brites, P. S. Andre, R. A. S. Ferreira, L. D. Carlos, *Advanced Science* **2019**, 6, 1900950; e) C. D. S. Brites, E. D. Martínez, R. R. Urbano, C. Rettori, L. D. Carlos, *Frontiers in Chemistry* **2019**, 7, 267; f) R. A. S. Ferreira, E. Mamontova, A. M. P. Botas, M. Shestakov, J. Vanacken, V. Moshchalkov, Y. Guari, L. F. Chibotaru, D. Luneau, P. S. Andre, J. Larionova, J. Long, L. D. Carlos, *Adv Opt Mater* **2021**, 9, 2101495.

[18] X. Zhou, L. Chen, S. Jiang, G. Xiang, L. Li, X. Tang, X. Luo, Y. Pang, *Dyes and Pigments* **2018**, 151, 219.

[19] a) I. E. Kolesnikov, A. A. Kalinichev, M. A. Kurochkin, D. V. Mamonova, E. Y. Kolesnikov, E. Lähderanta, *J. Phys. Chem. C* **2019**, 123, 5136; b) S. S. Zhou, C. K. Duan, M. Yin, S. B. Zhang, C. Wang, *J. Alloy. Compd.* **2019**, 784, 970; c) A. Ćirić, L. Marciniak, M. D. Dramićanin, *J. Appl. Phys.* **2022**, 131, 114501.
[20] D. L. Duan, Y. J. Wang, S. Jiang, L. Li, G. T. Xiang, X. Tang, Y. H. Li, X. J. Zhou, *J. Lumin.* **2019**, 215, 116636.
[21] K. Trejgis, A. Bednarkiewicz, L. Marciniak, *Nanoscale* **2020**, 12, 4667.
[22] K. Trejgis, K. Maciejewska, A. Bednarkiewicz, L. Marciniak, *ACS Applied Nano Materials* **2020**, 3, 4818.
[23] Z. Yuan, P. Lixin, T. Peng, Z. Zhiguo, *Opt. Express* **2021**, 29, 22805.
[24] L. Li, P. Yang, W. Xia, Y. Wang, F. Ling, Z. Cao, S. Jiang, G. Xiang, X. Zhou, Y. Wang, *Ceramics International* **2021**, 47, 769.
[25] I. E. Kolesnikov, D. V. Mamonova, M. A. Kurochkin, E. Y. Kolesnikov, E. Lahderanta, *J. Lumin.* **2021**, 231, 117828.
[26] B. Valeur, M. N. Berberan-Santos, *Journal of Chemical Education* **2011**, 88, 731.
[27] Y. Zhao, C. Riemersma, F. Pietra, R. Koole, C. De Mello Donegá, A. Meijerink, *ACS Nano* **2012**, 6, 9058.
[28] S. Uchiyama, C. Gota, T. Tsuji, N. Inada, *Chemical Communications* **2017**, 53, 10976.
[29] P. Löw, B. Kim, N. Takama, C. Bergaud, *Small* **2008**, 4, 908.
[30] J. C. G. Bünzli, *Handbook on the Physics and Chemistry of Rare Earths* **2016**, 50, 141.
[31] K. Binnemans, in *Handbook on the Physics and Chemistry of Rare Earths*, Vol. 35 (Eds: K. A. Gschneidner Jr., J.-C. G. Bünzli, V. K. Pecharsky), Elsevier Science, B. V., Amsterdam **2005**, Ch. 225, p. 107.
[32] D. Jaque, F. Vetrone, *Nanoscale* **2012**, 4, 4301.
[33] C. D. S. Brites, A. Millán, L. D. Carlos, in *Including Actinides*, Vol. 49 (Eds: B. Jean-Claude, P. V. K.]), Elsevier, 2016, 339.
[34] X. Liu, C. H. Yan, J. A. Capobianco, *Chemical Society Reviews* **2015**, 44, 1299.
[35] C. D. S. Brites, A. Millán, L. D. Carlos, in *Handbook on the Physics and Chemistry of Rare Earths*, Vol. 49 (Eds: J.-C. G. Bünzli, V. K. Pecharsky), Elsevier Science, B. V., Amsterdam **2016**, Ch. 281, p. 339.
[36] J. C. Martins, C. D. S. Brites, A. N. C. Neto, R. A. S. Ferreira, L. D. Carlos, in *Luminescent Thermometry: Applications and Uses*, DOI: 10.1007/978-3-031-28516-5_3 (Eds: J. J. Carvajal Martí, M. C. Pujol Baiges), Springer International Publishing, Cham **2023**, p. 105.
[37] a) Q. Li, X. He, Y. Wang, H. Liu, D. Xu, F. Guo, *Journal of Biomedical Optics* **2013**, 18, 1; b) G. A. Roth, S. Tahiliani, N. M. Neu-Baker, S. A. Brenner, in *WIREs Nanomedicine and Nanobiotechnology*, Vol. 7, John Wiley & Sons, Ltd, 2015, 565.
[38] J. M. Amigo, in *Data Handling in Science and Technology*, Vol. 32, 2020, 3.
[39] A. F. H. Goetz, in *Imaging spectroscopy*, Vol. 228, 1992, 1.
[40] A. Iqbal, D.-W. Sun, P. Allen, *Food Control* **2014**, 46, 242.
[41] a) T. Chen, P. Yuen, M. Richardson, G. Liu, Z. She, in *IEEE Transactions on Affective Computing*, Vol. 5, 2014, 391; b) V. C. Coffey, *Optics and Photonics News* **2015**, 26, 26.
[42] a) M. Mortimer, A. Gogos, N. Bartolomé, A. Kahru, T. D. Bucheli, V. I. Slaveykova, *Environmental Science and Technology* **2014**, 48, 8760; b) D. Yohan, C. Cruje, X. Lu, D. Chithrani, *Nano-Micro Letters* **2015**, 7, 127; c) J. H. Shannahan, H. Sowrirajan, I. Persaud, R. Podila, J. M. Brown, in *Journal of Nanomaterials*, Vol. 2015, 2015; d) P. Zamora-Perez, D. Tsoutsi, R. Xu, P. Rivera-Gil, in *Materials*, Vol. 11, 2018; e) F. Akhatova, A. Danilushkina, G. Kuku, M. Saricam, M. Culha, R. Fakhrullin, *Bulletin of the Chemical Society of Japan* **2018**, 91, 1640.
[43] a) V. Mikulová, K. Kološtová, T. Zima, in *Folia Biologica (Czech Republic)*, Vol. 57, 2011, 151; b) K. Darwiche, P. Zarogoulidis, L. Krauss, F. Oezkan, R. F. H. Walter, R. Werner, D. Theegarten, L. Sakkas, A. Sakkas, W. Hohenforst-Scmidt, K. Zarogoulidis, L. Freitag, *International journal of nanomedicine* **2013**, 8, 4533; c) G. Lu, B. Fei, *Journal of Biomedical Optics* **2014**, 19, 010901; d) G. A. Sotiriou, F. Starsich, A. Dasargyri, M. C. Wurnig, F. Krumeich, A. Boss, J.-C. Leroux, S. E. Pratsinis, *Advanced Functional Materials* **2014**, 24, 2818; e) S. Zhu, K. Su, Y. Liu, H. Yin, Z. Li, F. Huang, Z. Chen, W. Chen, G. Zhang, Y. Chen, *Biomedical Optics Express* **2015**, 6, 1135.
[44] M. L. Debasu, C. D. S. Brites, S. Balabhadra, H. Oliveira, J. Rocha, L. D. Carlos, *ChemNanoMat* **2016**, 2, 520.
[45] F. J. Caixeta, A. R. N. Bastos, A. M. P. Botas, L. S. Rosa, V. S. Souza, A. N. Carneiro Neto, A. Ferrier, P. Goldner, L. D. Carlos, R. R. Gonçalves, R. A. S. Ferreira, *The Journal of Physical Chemistry C* **2020**, DOI: 10.1021/acs.jpcc.0c03874.
[46] E. M. Rodrigues, N. Rutajoga, D. Rioux, J. Yvon-Leroux, E. Hemmer, *Journal of Visualized Experiments* **2020**, 2020, 1.

[47] R. Marin, I. Halimi, D. Errulat, Y. Mazouzi, G. Lucchini, A. Speghini, M. Murugesu, E. Hemmer, *ACS Photonics* **2019**, 6, 436.
[48] D. Errulat, B. Gabidullin, M. Murugesu, E. Hemmer, *Chemistry - A European Journal* **2018**, 24, 10146.
[49] A. Nadort, V. K. A. Sreenivasan, Z. Song, E. A. Grebenik, A. V. Nechaev, V. A. Semchishen, V. Y. Panchenko, A. V. Zvyagin, *PLoS ONE* **2013**, 8.
[50] T. T. Bai, N. Gu, *Small* **2016**, 12, 4590.
[51] R. Piñol, C. D. S. Brites, N. J. Silva, L. D. Carlos, A. Millán, in *Nanomaterials for Magnetic and Optical Hyperthermia Applications* (Eds: R. Fratila, J. M. de la Fuente), Elsevier, Amsterdam **2019**, p. 139.
[52] M. L. Debasu, D. Ananias, I. Pastoriza-Santos, L. M. Liz-Marzán, J. Rocha, L. D. Carlos, *Advanced Materials* **2013**, 25, 4868.
[53] S. Zanella, E. Trave, E. Moretti, A. Talon, M. Back, L. D. Carlos, R. A. S. Ferreira, C. D. S. Brites, *Frontiers in Photonics* **2022**, 3.
[54] K. M. N. d. Souza, *Doutor em Ciência de Materiais* Universidade Federal de Pernambuco, Recife, 24-05-2019, **2019**.
[55] E. Hemmer, A. Benayas, F. Legare, F. Vetrone, *Nanoscale Horizons* **2016**, 1, 168.
[56] X. Zhu, Q. Su, W. Feng, F. Li, *Chemical Society Reviews* **2017**, 46, 1025.
[57] S. L. Gai, P. P. Yang, D. Wang, C. X. Li, N. Niu, F. He, X. B. Li, *Crystengcomm* **2011**, 13, 5480.
[58] M. L. Debasu, H. Oliveira, J. Rocha, L. D. Carlos, *Journal of Rare Earths* **2020**, 38, 483.
[59] J. Kai, D. F. Parra, H. F. Brito, *J Mater Chem* **2008**, 18, 4549.
[60] F. J. Caixeta, A. R. N. Bastos, A. M. P. Botas, L. S. Rosa, V. S. Souza, A. N. Carneiro Neto, A. Ferrier, P. Goldner, L. D. Carlos, R. R. Gonçalves, R. A. S. Ferreira, *The Journal of Physical Chemistry C* **2020**, 124, 19892.
[61] P. R. Twentyman, M. Luscombe, *Brit J Cancer* **1987**, 56, 279.
[62] I. J. Standard, (Ed: S. I. O. f. S. Geneve), 2009.
[63] R. Reisfeld, C. K. Jørgensen, in *Lasers and Excited States of Rare Earths*, DOI: 10.1007/978-3-642-66696-4_2, Springer Berlin Heidelberg, Berlin, Heidelberg **1977**, p. 64.
[64] L. A. Riseberg, M. J. Weber, in *Progress in Optics*, Vol. 14 (Ed: E. Wolf), Elsevier **1977**, p. 89.
[65] W. T. Carnall, H. Crosswhite, H. M. Crosswhite, Argonne Nat. Lab. 78-XX-95 Rep., 1977.
[66] K. Binnemans, *Coordination Chemistry Reviews* **2015**, 295, 1.
[67] G. Liu, *Chemical Society reviews* **2015**, 44, 1635.
[68] C. Görller-Walrand, K. Binnemans, in *Handbook on the Physics and Chemistry of Rare Earths*, Vol. 25, Elsevier **1998**, p. 101.
[69] W. J. Tropf, M. E. Thomas, T. J. Harris, in *Handbook of Optics, Vol. II: Devices, Measurements, and Properties* (Ed: M. Bass), McGraw-Hill Inc, New York **1995**, Ch. 33, p. 3.
[70] G. Ghosh, in *Handbook of Optical Constants of Solids*, DOI: https://doi.org/10.1016/B978-012544415-6.50150-3 (Ed: E. D. Palik), Academic Press, Burlington **1997**, p. 115.
[71] L. Haar, *Science* **1972**, 176, 1293.
[72] a) P. A. Tanner, *Chemical Society Reviews* **2013**, 42, 5090; b) M. H. V. Werts, R. T. F. Jukes, J. W. Verhoeven, *Physical Chemistry Chemical Physics* **2002**, 4, 1542.
[73] A. Escudero, E. Moretti, M. Ocaña, *CrystEngComm* **2014**, 16, 3274.
[74] J. J. Joos, D. Poelman, P. F. Smet, *Physical Chemistry Chemical Physics* **2015**, 17, 19058.
[75] F. E. Maturi, C. D. S. Brites, E. C. Ximendes, C. Mills, B. Olsen, D. Jaque, S. J. L. Ribeiro, L. D. Carlos, *Laser & Photonics Reviews* **2021**, 15, 2100301.
[76] a) M. Suzuki, T. Plakhotnik, *Biophysical Reviews* **2020**, 12, 593; b) J. J. Zhou, B. del Rosal, D. Jaque, S. Uchiyama, D. Y. Jin, *Nature Methods* **2020**, 17, 967.
[77] a) J. Lifante, Y. Shen, I. Zabala Gutierrez, I. Rubia-Rodríguez, D. Ortega, N. Fernandez, S. Melle, M. Granado, J. Rubio-Retama, D. Jaque, E. Ximendes, *Advanced Science* **2021**, 8, 2003838; b) A. Bednarkiewicz, J. Drabik, K. Trejgis, D. Jaque, E. Ximendes, L. Marciniak, *Applied Physics Reviews* **2021**, 8, 011317.
[78] a) S. Kittler, C. Greulich, J. S. Gebauer, J. Diendorf, L. Treuel, L. Ruiz, J. M. Gonzalez-Calbet, M. Vallet-Regi, R. Zellner, M. Köller, M. Epple, *Journal of Materials Chemistry* **2010**, 20, 512; b) S. Shanwar, L. Liang, A. V. Nechaev, D. K. Bausheva, I. V. Balalaeva, V. A. Vodeneev, I. Roy, A. V. Zvyagin, E. L. Guryev, *Materials* **2021**, 14, 1657.
[79] R. N. Silva, A. M. P. Botas, D. Brandão, V. Bastos, H. Oliveira, M. L. Debasu, R. A. S. Ferreira, C. D. S. Brites, L. D. Carlos, *Physica B: Condensed Matter* **2022**, 626, 413470.
[80] C. D. Brites, X. Xie, M. L. Debasu, X. Qin, R. Chen, W. Huang, J. Rocha, X. Liu, L. D. Carlos, *Nature Nanotechnology* **2016**, 11, 851.
[81] a) K. Kuruvinashetti, A. S. Kashani, S. Badilescu, D. Beaudet, A. Piekny, M. Packirisamy, *Plasmonics* **2018**, 13, 1639; b) P. VALLOTTON, B. ANGEL, M. MCCALL, M. OSMOND, J. KIRBY, *Journal of*

Microscopy **2015**, 257, 166; c) S. Patskovsky, E. Bergeron, M. Meunier, *Journal of Biophotonics* **2015**, 8, 162.
[82] N. Panov, D. Lu, E. Ortiz-Rivero, E. Martinazzo Rodrigues, P. Haro-González, D. Jaque, E. Hemmer, *Advanced Optical Materials* **2021**, 9, 2100101.
[83] W. Gao, J. Dong, Z. Wang, Z. Zhang, H. Zheng, *Materials Research Bulletin* **2017**, 91, 77.
[84] F. Gonell, A. M. P. Botas, C. D. S. Brites, P. Amorós, L. D. Carlos, B. Julián-López, R. A. S. Ferreira, *Nanoscale Advances* **2019**, 1, 2537.
[85] P. Sarder, A. Nehorai, *IEEE Signal Processing Magazine* **2006**, 23, 32.
[86] R. Piñol, C. D. S. Brites, R. Bustamante, A. Martínez, N. J. O. Silva, J. L. Murillo, R. Cases, J. Carrey, C. Estepa, C. Sosa, F. Palacio, L. D. Carlos, A. Millán, *ACS Nano* **2015**, 9, 3134.
[87] A. Ćirić, S. Stojadinović, M. D. Dramićanin, *Journal of Luminescence* **2019**, 216, 116749.
[88] G. Belušič, M. Ilić, A. Meglič, P. Pirih, *Scientific Reports* **2016**, 6, 32012.
[89] B. G. Wybourne, W. F. Meggers, *Physics Today* **1965**, 18, 70.
[90] W. B. Fowler, D. L. Dexter, *Physical Review* **1962**, 128, 2154.
[91] C. Görller-Walrand, K. Binnemans, in *Handbook on the Physics and Chemistry of Rare Earths*, Vol. 25 (Eds: K. A. G. Jr., L. Eyring), North-Holland Publishers Amsterdam **1998**, Ch. 167, p. 101.
[92] J. M. Zhang, Y. Liu, *European Journal of Physics* **2016**, 37, 065406.
[93] G. C. Schatz, M. A. Ratner, *Quantum Mechanics in Chemistry*, Dover Publications Inc, New York **2002**.
[94] G. F. d. Sá, O. L. Malta, C. d. M. Donegá, A. M. Simas, R. L. Longo, P. A. Santa-Cruz, E. F. d. S. Jr, *Coordination Chemistry Reviews* **2000**, 196, 165.